SINGLE-STATION EVENT LOCATION USING P- AND S-WAVES

by

Lauren Phillips

APPROVED BY SUPERVISORY COMMITTEE:

____

John F. Ferguson, Chair

____

John W. Geissman

____

Hejun Zhu

To my family

SINGLE-STATION EVENT LOCATION USING P- AND S-WAVES

by

LAUREN PHILLIPS, BS

THESIS

Presented to the Faculty of

The University of Texas at Dallas

in Partial Fulfillment

of the Requirements

for the Degree of

MASTER OF SCIENCE IN

GEOPHYSICS

THE UNIVERSITY OF TEXAS AT DALLAS

May 2020

ACKNOWLEDGMENTS

I would first like to show my appreciation to my thesis advisor, Dr. John Ferguson, for his guidance, dedication, and mentorship throughout my graduate education. I also want to thank my committee members, Dr. John Ferguson, Dr. John Geissman, and Dr. Hejun Zhu, for their review of this thesis. I thank my family who provided support, patience, and encouragement throughout the duration of my education.

April 2020

SINGLE-STATION EVENT LOCATION USING P- AND S-WAVES

Lauren Phillips, MS
The University of Texas at Dallas, 2020

Supervising Professor: John F. Ferguson

Seismic data are currently available for the Earth and its Moon. Such data are the most valuable type of information for the determination of internal structure. On November 26, 2018, the InSight (Interior Exploration using Seismic Investigations, Geodesy and Heat Transport) mission deployed a geophysical lander on Mars using a single seismic station to gather information about the planet's internal structure and seismicity. An instrument composed of multicomponent broadband and short period seismometers was deployed to record seismic noise, marsquakes, and meteor impacts. With just a single station, traditional source location methods are impossible, and different techniques need to be used.

Some form of polarization analysis must be used for single-station event location methods. Single-station location is based on the determination of station to event azimuth and epicentral distance. For the initial linearly polarized P-wave, a single eigenvector of the signal covariance matrix can determine the azimuth. Epicentral distance can be computed using either the incidence angle to compute slowness or the S-P time differences. If incidence angle is used, then the P-wave eigenvectors are used to compute an incidence angle. S-P times or other phase

differences can also be used to determine epicentral distance. These methods are more reliable than computation of the incidence angle. With the azimuth and epicentral distance, the location of seismic events can be determined relative to the station.

This thesis develops a processing methodology and investigates the ability of a single, three-component seismic station to determine event locations. The proposed process uses a variant of Samson and Olson's (1981) polarization method in the time domain with a complex covariance matrix derived from East-North-Vertical (E, N, Z) component seismograms. Azimuth is derived from the (E, N) components. The system is then rotated into the Radial-Transverse-Vertical (R, T, Z) coordinate system. The apparent incidence angle is then determined from the (R, Z) components. Application of Snell's Law yields the horizontal slowness, from which horizontal distance and traveltimes are determined by ray tracing in a global velocity model. Distance can also be determined from traveltime differences between different phase arrivals. The S and P arrivals are most commonly used. With these parameters, the latitude, longitude, and origin time of the event are determined, which is the epicenter. If depth can be determined, the hypocenter is obtained. Depth can be estimated from extracting the pP surface reflection and using the traveltime difference with respect to P. Seismicity maps based on single-station event locations are compared to nominal, or more accurate, United States Geological Survey (USGS) Global Seismographic Network (GSN) locations to see if plate tectonic structures can be identified from single-station results.

TABLE OF CONTENTS

LIST OF TABLES

LIST OF FIGURES

LIST OF SYMBOLS

(θ_e, ψ_e, d_e)	event latitude, longitude, and depth (deg, rad, m, km)
(θ_s, ψ_s, h_s)	station latitude, longitude, and elevation (deg, rad, m, km)
t	time (s, day)
T_0	origin time (date and time)
T_{UTC}	universal time (date and time)
T	traveltime for various phases, $T = T_{UTC} - T_0$
P, S, pP, etc.	phase designations
Δ	angular distance at Earth's surface (θ_e, ψ_e) – (θ_s, ψ_s) (deg, rad)
A	azimuth- at the station (deg, rad)
I	inclination- at the station (deg, rad)
r	radial coordinate inside the Earth (m, km)
r_E	mean Earth radius (m, km)
r_p, r_e	polar and equatorial radii of ellipsoid - WGS84 ellipsoid (m, km)
$V_P(r)$, $V_S(r)$	radial velocity functions - from Earth model (m/s, km/s)
p	horizontal slowness (s/m, s/km, s/rad) related to I via Snell's Law (and free surface BC)
τ	delay time (s)
Δt	sample interval (s)
$s(t)$	real seismogram (signal and noise) ($^{\mu m}/_{s}$)
$s(t)$	complex analytic seismogram - $\mathrm{Re}(s(t)) + i\mathrm{Im}(s(t))$
(E, N, Z)	local Cartesian coordinates (m, km, $^{\mu m}/_{s}$, etc.)
(R, T, Z)	local Cartesian coordinates rotated into A direction (m, km, $^{\mu m}/_{s}$, etc.)
S	three-component seismograms - $(S_E, S_N, S_Z), (S_R, S_T, S_Z)$
φ	phase angle (rad)
ω	angular frequency (rad/s)
f	frequency (Hz) - $\omega = 2\pi f$
f_L	local frequency is f averaged over a short time window
E	instantaneous envelope of $s(t)$
E^2	instantaneous energy of $s(t)$
L	trace length or complexity
t_c	exponential decay time constant (s)
β	smoothing parameter $0<\beta<1$
C	covariance matrix
u	eigenvector of **C**
λ	eigenvalue of **C**
a	AR model coefficients
ε	white noise
σ^2	noise variance
P_s	linear polarization measure

P_p	planar polarization measure
P	pure state polarization measure
P_{ind}	P-wave indicator
S_{ind}	S-wave indicator
$u(t)$	generic function of time (envelope, covariance, etc.)
$\bar{u}(t)$	exponentially weighted average of variable $u(t)$
$\hat{u}(t)$	estimate of variable $u(t)$
$\delta\Lambda$	angular location error, $(\theta_e, \psi_e) - (\widehat{\theta_e}, \widehat{\psi_e})$ nominal - estimate
δA	azimuth error, $A - \hat{A}$ nominal - estimate
$\delta\Delta$	distance error, $\Delta - \hat{\Delta}$ nominal - estimate
$*$	convolution
<=>	Fourier transform pair

CHAPTER 1

INTRODUCTION

Conventional methods for the location of seismic events use an array, or network, of seismometers because single stations are believed to result in crude estimates. An abundance of stations is required to obtain suitable azimuthal coverage. Single stations with three orthogonal components were often used for “quick and dirty” locations when more adequate data were unavailable. Due to advancements in technology, such as modern digital data acquisition and automated detection, single stations have reclaimed attention, particularly for nuclear explosion monitoring (Kim and Wu, 1997).

Single-station event location analysis must use some form of polarization analysis. Both azimuth and epicentral distance, either determined by incidence angle or S-P times, need to be determined to locate events. Azimuth and incidence angle can be determined using this technique by solving the eigenvalue problem for the covariance matrix (Kim and Gao, 1997). For the initial, linearly polarized P-wave, a single eigenvector can determine both the azimuth and incidence angle (Samson and Olson, 1980; Samson and Olson, 1981). For the planar polarized S-wave, generally all eigenvalues must be computed to determine an azimuth. S-wave motion is confined to a dipping plane, where the SV-wave moves in the vertical and horizontal directions and the SH-wave moves only in the horizontal direction. There can be linear motion if purely an SH-wave is present; however, generally, there is a combination of the SV- and SH-waves (and typically they are out of phase with one another), resulting in elliptical motion. If there is evidence of an SV-wave, then an incidence angle might be computed. Epicentral distance can also be computed by S-P times or other phase time differences. In this case, there must be an S-wave (or other phase) arrival. With this information, it is possible to detect and locate events using single-station data.

The pP-phase is used to determine the depth of the event. The pP-phase leaves the source going up, reflects off the surface of the Earth, and then turns in the mantle, unlike direct waves which originate at the source and then turn in the mantle. The pP-phase follows behind the direct P-phase (Scrase, 1931). The time delay between the P- and pP-phases is proportional to the depth of the event. With increasing depth, the travel time difference increases (Khan et al, 2016).

In November of 2018, the InSight mission deployed a seismic station on Mars that incorporates multicomponent seismometers (Clinton et al., 2017; Panning et al., 2017). Using a single station, standard methods for source location cannot be implemented, and different methods are required to extract event location (Panning et al., 2012). Events might include earthquakes, meteorite impacts, and landslides (Mimoun et al., 2017). Seismic events on Mars can be located by finding the P- and S-wave arrival times and polarizations (Khan, 2016; Panning et al., 2012). Traveltime and horizontal slowness can be computed for radially symmetric Martian velocity models (Panning et al., 2015). These methods yield epicentral distance and origin time. S-P times can produce reliable distances and origin times. Along with azimuth, these determine the epicenter. This single seismic station is the first step towards a Martian seismic network (Ruedas et al., 2009).

As will be done on Mars, a single seismic station selected from the GSN will be used in this research to demonstrate the method of single station event location. The objective is to investigate various data processing options utilizing only a single three-component seismic station. Polarization analysis will provide information to locate events. The effectiveness of the processor will be investigated by comparison to estimated United States Geological Survey (USGS) locations from the GSN for several events. Distances are constrained between 10° and 90° to confine raypaths to the mantle. As will be shown, station geology and the effects of heterogeneity local to the stations have a big effect on single-station event location results. The velocity structure of the Earth generally increases with depth but is not spherically symmetrical; however, this is a good first approximation. Radial symmetry is assumed in order to locate the event, however, there is going to be heterogeneity that causes the calculated location to be different from the nominal, or more accurate, USGS GSN location. The purpose of this research is to see how misleading the results can be when compared to the nominal locations.

This work also investigated how estimated single-station locations compare to nominal locations in the context of plate tectonic boundaries. In other words, can tectonic plate boundaries be located from single-station locations? How do the estimated single-station locations align with the boundaries? Gutenberg and Richter's (1954) seismicity map of the Earth was used for this analysis. Gutenberg and Richter's work represented 50 years of seismicity in a pre-plate tectonic era and before the installation of the Worldwide Standardized Seismograph Network (WWSSN), which provided better global station coverage. On a different planet, there would be limited knowledge, similar to the knowledge of the Earth in the 1950's using dozens of stations. Could one station perform as well as Gutenberg and Richter did in 1954? For this experiment, modern data was used because digital seismograms from that time are not available.

1.1 Background

The InSight mission will investigate Mars structure and seismicity using a single seismic station (Raucourt et al., 2012; Clinton et al., 2017). The mission is intended to examine the interior of Mars, giving scientists new insight into solar system evolution (Murdoch et al., 2016; Mimoun et al., 2017; Lognonné et al., 2017). Due to the absence of extensive plate tectonics, Mars has retained historical evidence related to its interior that is lost on geologically active planets like Earth (Khan et al., 2016; Panning et al., 2017; Lognonné et al., 2017). A three-component single-station will be planted on the surface, taking precise measurements for both the Mars Structure Service and Marsquake Service (Khan et al., 2016; Panning et al., 2017). SEIS (Seismic Experiment for Interior Structures) is a composite instrument, composed of two independent systems: a very broad band and short period multicomponent seismometer (Clinton et al., 2017; Mimoun et al., 2017; Raucourt et al., 2012; Murdoch et al., 2016; Bowles, 2015). Three very broad band seismic sensors form a core that is enclosed by a titanium vacuum sphere (Dandonneau et al., 2013). Three short period sensors consist of silicon suspensions with laterally moving masses (Bowles, 2015). These sensors can detect a wide range of signals, including body waves, surface waves, and the Phobos tide (Dandonneau et al., 2013).

Seismic events on Mars can be located by obtaining the epicentral distance and azimuth (Khan et al., 2016; Panning et al., 2012). First, the seismogram is analyzed, and the P- and S-wave arrival times are picked (Khan et al., 2016; Panning et al., 2012). Arrival times are also computed theoretically from radially symmetric Martian velocity models (Khan et al., 2016). Initial models are obtained by satisfying the known mass and moment of inertia, and by using silicate mineral phase diagrams and thermodynamic data (Clinton et al., 2017). Actual seismic data will then be used in a kind of “bootstrap” process to improve the model. Relying on this 1D model, these differential arrival times can be compared (Clinton et al., 2017; Panning et al., 2012). Surface waves will also be used in the location process.

In contrast to Mars, Earth has a global digital network that provides free, real-time, open access data. The Global Seismographic Network (GSN) is comprised of more than 150 stations distributed globally and that attempts to provide uniform, unbiased coverage of the Earth. The advanced system was established in 1986 by Incorporated Research Institutions for Seismology (IRIS) and the USGS, as well as through coordination with the international community, to upgrade from the analog Worldwide Standardized Seismograph Network (WWSSN). The goal was to install and operate a global, multi-use scientific facility and societal resource for Earth observations, environmental monitoring, scientific research, and education (Gee and Leith, 2011; Bent 2013; Butler, 2004; Ammon et al., 2010). The GSN stations strive for the optimal recording capability balanced with international geographic coverage (Park et al., 2005; Bent, 2013). A wide range of frequencies is recorded by the network of broadband, three-component seismometers (Gee and Leith, 2011; Ammon et al., 2010).

The network archives seismic data from all stations that can be used to study earthquakes. A passing wavefront expands and reaches more distant seismic stations, keeping record of the times at which the wavefront passes each station. With the arrival times, the source location can be obtained (U.S. Geological Survey, 2018). The problem of earthquake location was cast as a least squares solution of a linearized inverse problem for the epicenter (or hypocenter) and origin time by Geiger (U.S. Geological Survey, 2018; Geiger, 1912). The method must have a velocity model to calculate traveltimes (U.S. Geological Survey, 2018).

Seismic arrays are generally seen as a better alternative to single seismic stations. The combination of signals from many individual seismometers makes them sensitive tools to detect events. Arrays improve the signal-to-noise ratio (SNR) when compared to single stations. The development of seismic arrays began in the late 1950s to the early 1960s. The first arrays were small, with about 10-36 seismometers (Rost and Thomas, 2002). Seismic arrays began to attract attention when there became growing interests in methods to monitor nuclear explosions. From 1945-1996, countries including the United States, Soviet Union, France, the United Kingdom, and China conducted a large number of nuclear tests. During this period, there were many efforts to restrain nuclear testing. In 1963, the Limited Test Ban Treaty (LTBT) placed a global ban on all nuclear weapon tests, except for underground environments

(Prăvălie, 2014). In 1971, an agreement between Norway and the US came into effect and the Norwegian Seismic Array (NORSAR) became operational in southeastern Norway (Lawyer et al., 2001; Lukasik, 2011; Schweitzer and Roth, 2015). The principal objective of the agreement was to provide a way to ensure compliance with the future Comprehensive Test Ban Treaty (CTBT) (Schweitzer and Roth, 2015). Later arrays were much larger that the first arrays (Rost and Thomas, 2002). NORSAR consisted of 132 short-period and 22 long-period three-component seismometers (Lukasik, 2011). In 1984, the US and Norway wanted to investigate monitoring regional events with arrays (U.S. Congress, 1988). Specialists at Sandia National Laboratories used the NORESS (an experimental subarray operated by NORSAR) facility to install a seismic array system that would detect and locate regional events (Lawyer et al., 2001). In 1993, the CTBT was enforced and placed a global ban on all nuclear weapon tests, including underground environments (Lawyer et al., 2001).

Arrays provide event locations by determining the azimuth and slowness from array measurements, and then ray tracing through the Earth. However, there is a calibration issue due to 3D velocity structure local to the array. To effectively use these arrays, calibration is best accomplished with a large number of events and azimuths. The advantage to the array method is that the slowness can be measured directly.

Even with the development of networks and arrays, single-station event location has remained an important topic. Due to advances in technology, single stations have reclaimed attention over time. Frohlich and Pulliam (1999) reviewed efforts to locate events using single stations. They discussed the significant role that single stations have on monitoring compliance with the CTBT. To monitor compliance, the locations and/or focal depths of the events are determined; focal depth is determined by waveform correlation where the observed and synthetic waveforms are matched. Even with the current seismic network, many regions of the world do not have three or more stations close enough to locate events. This leaves single-station event location as the only option to locate events, which is why more research and technological advances are needed for this method (Frohlich and Pulliam, 1999).

1.2 Station Data and Geology

Station geology significantly impacts single-station event location accuracy. The velocity structure of the Earth generally increases with depth but is not strictly spherically symmetrical. However, this is a good first approximation; a radial-only velocity structure allows for less complicated traveltime calculations (Bullen and Bolt, 1985). The multi-station event location method also assumes radial structure but allows for local corrections. Near the station, local geology may cause the radial-only approximation to fail. Structural features usually have some preferred orientation and can extend down into the lower crust, and possibly the mantle. Therefore, radial symmetry is assumed in order to locate the event, however, heterogeneities will cause the calculated location to be different from the nominal location. This research evaluates how misleading the single-station locations are when compared to the nominal locations.

Stations located in different geotectonic settings were selected from the Texas and Oklahoma region. TX32 is located with the TXAR Array, in Lajitas, TX. WHTX was part of the EarthScope Transportable Array Network located at Lake Whitney, TX, and is now a permanent station. WMOK is part of the US National Seismic Network, located in the Wichita Mountains, OK (Figure 1). The goal is to obtain homogeneous event coverage of a hemisphere in both azimuth and distance. Figure 2 shows the Texas/Oklahoma Cambrian structural features along with the major geologic provinces.

Earth data can be accessed from https://earthquake.usgs.gov/earthquakes/search/. Earth data can also be accessed from https://www.iris.edu; Mars data is and will be available from this website as well.

Figure 1. Location map of the three selected seismic stations in the TXOK region.

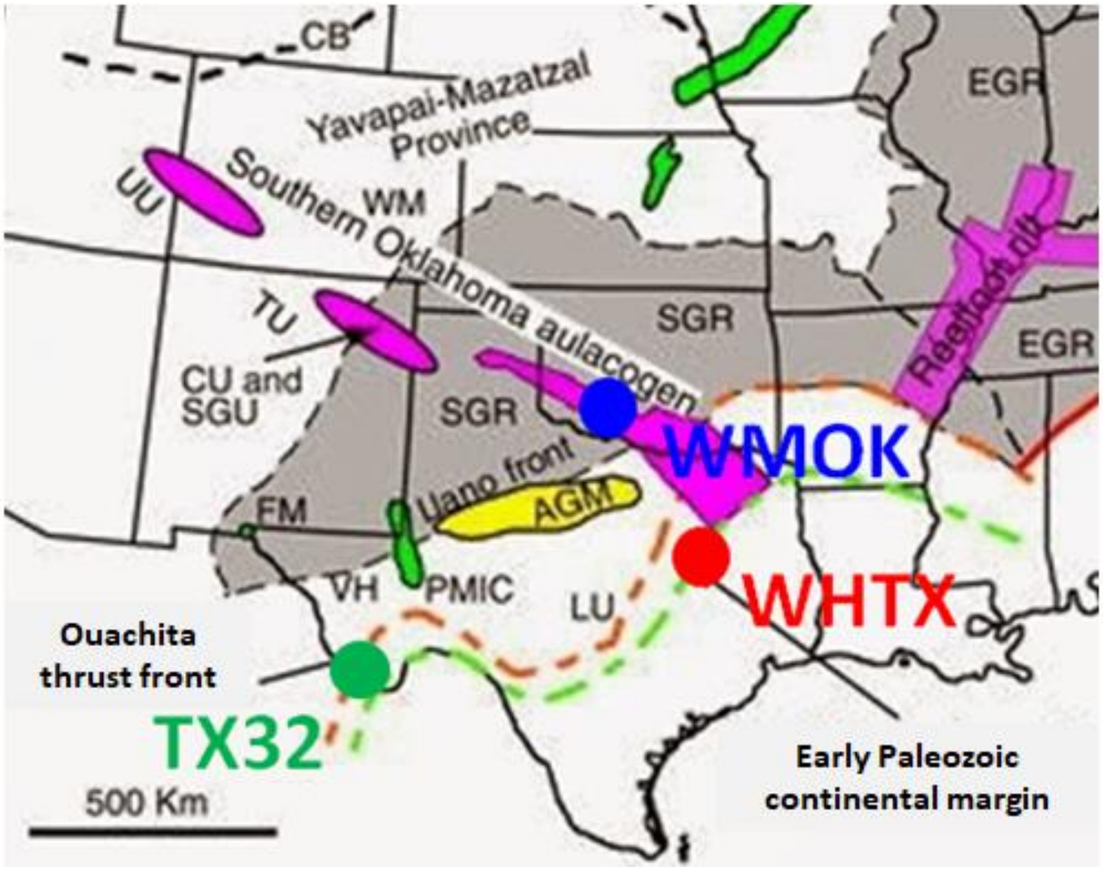

Figure 2. Texas/Oklahoma tectonic features. EGR- eastern granite-rhyolite province; SGR- southern granite-rhyolite province; CB- Cheyenne belt; PMIC- Pecos mafic intrusive complex; AGM- Abilene gravity minimum; FM- Franklin Mountains; TU- Tusas uplift; WM- Wet Mountains; UU- Uncompahgre uplift; CU- Cimarron uplift; SGU- uplift; VH- Van Horn area; LU- Llano uplift (modified from Van Schmus et al., 1996)

Tables 1-3. IRIS metadata available for each station used in this study.

Table 1. TX32 metadata

Latitude	29.334°
Longitude	-103.6677°
Elevation	995.5 m
Instrument	KS54000
Channels	**E** BHE **N** BHN **Z** BHZ

Table 2. WHTX metadata

Latitude	31.9913°
Longitude	-97.4561°
Elevation	190 m
Instrument	Streckeisen STS-2 G3
Channels	**E** BHE **N** BHN **Z** BHZ

Table 3. WMOK metadata

Latitude	34.7379°
Longitude	-98.7807°
Elevation	486 m
Instrument	STS2-I
Channels	**E** BH2 **N** BH1 **Z** BHZ

The nominal frequency and phase response curves are shown in Figures 3-5. TX32 experiences low noise, which results in higher gain at this station. The higher gain could explain the higher frequency at this site.

Six years of data were obtained for a hemisphere that was centered on Texas. A total of 9,934 events worldwide with magnitudes ≥5 were downloaded from the Advanced National Seismic System (ANSS) Comprehensive Catalog and are shown in Figure 6. Catalog locations were assumed to be correct and nominal. The green, blue, and red triangles represent the three TXOK stations.

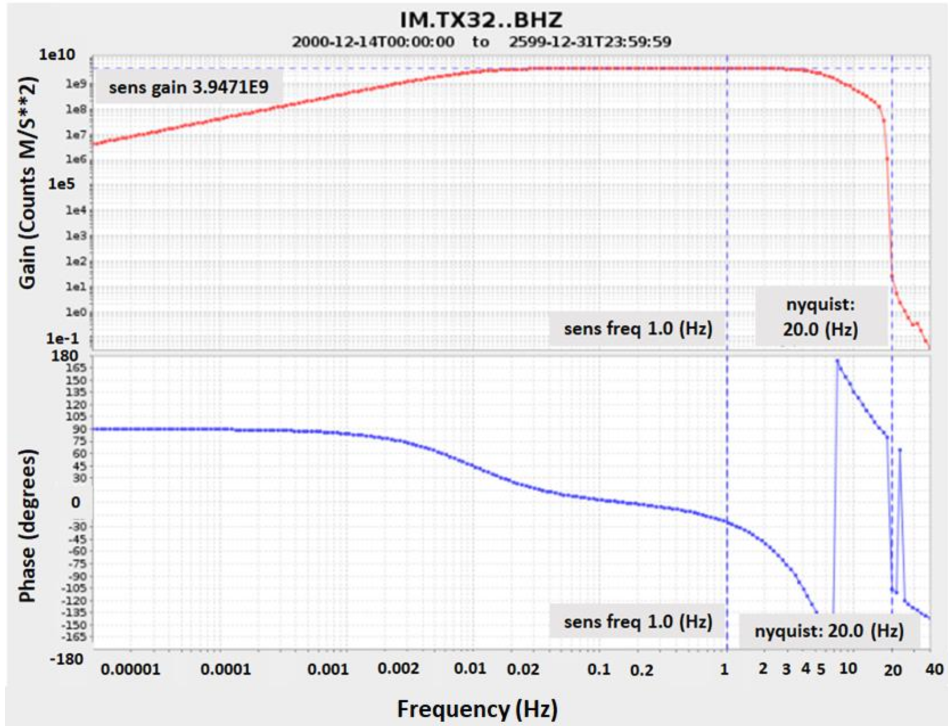

Figure 3. The BHZ channel for TX32.

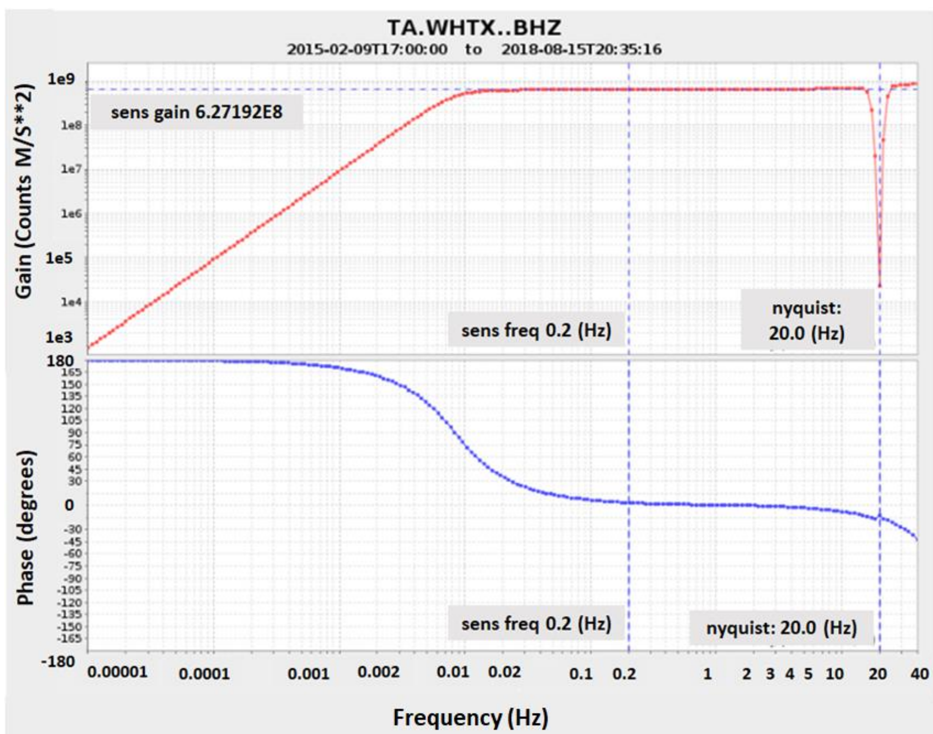

Figure 4. The BHZ channel for WHTX.

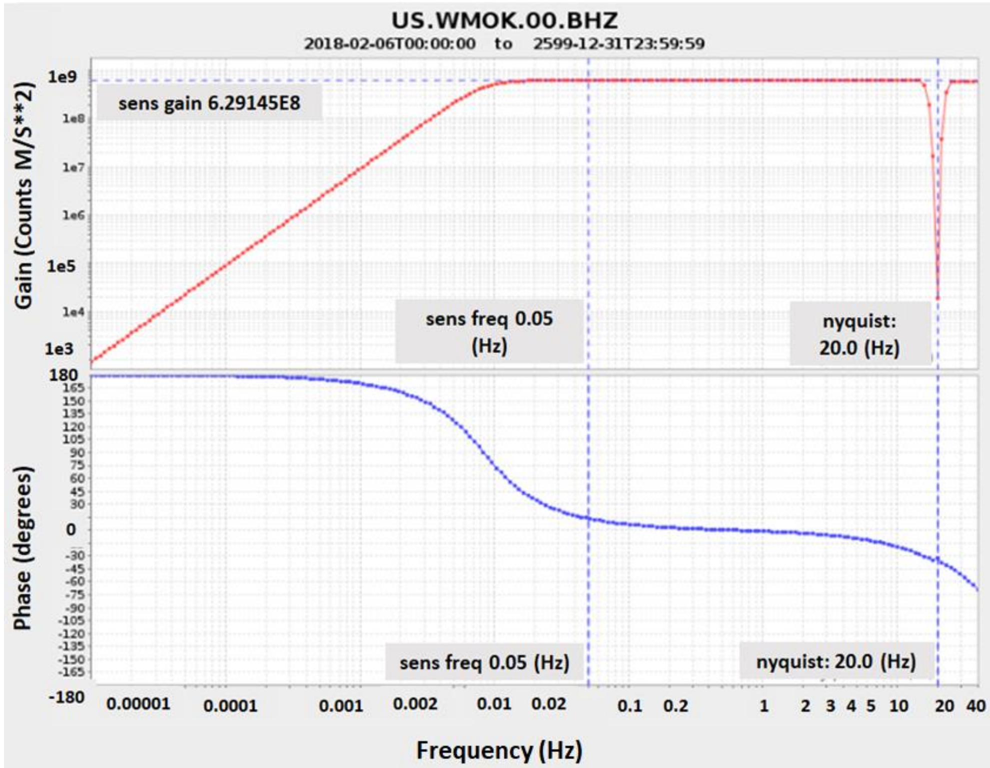

Figure 5. The BHZ channel for WMOK.

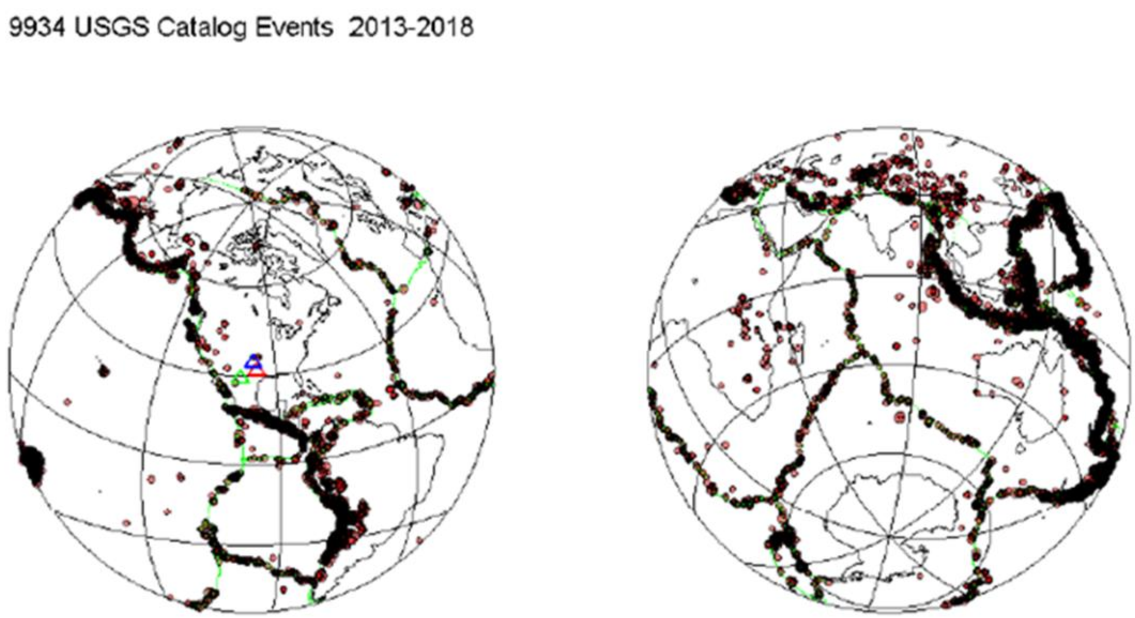

Figure 6. Worldwide events obtained from the USGS catalog.

In this process, multiple events were eliminated. These are events that occurred within the same time frame, but at different locations. If two (or sometimes three) events occurred within 30 minutes of one another, the earliest event was retained, and the later events were discarded. There were 1,638 multiple events worldwide; eliminating these reduced the number of total events without time overlap to 8,296 worldwide. Next, a hemisphere centered on the centroid of TX32, WHTX, and WMOK was selected, further reducing the number of events to 3,262. A magnitude constraint was implemented to include only earthquakes with magnitudes ≥6 worldwide, which reduced the number of events to 709. A distance constraint was then implemented to only include earthquakes with distances between 10° and 90°, which reduced the number of events to 274 (Figure 7).

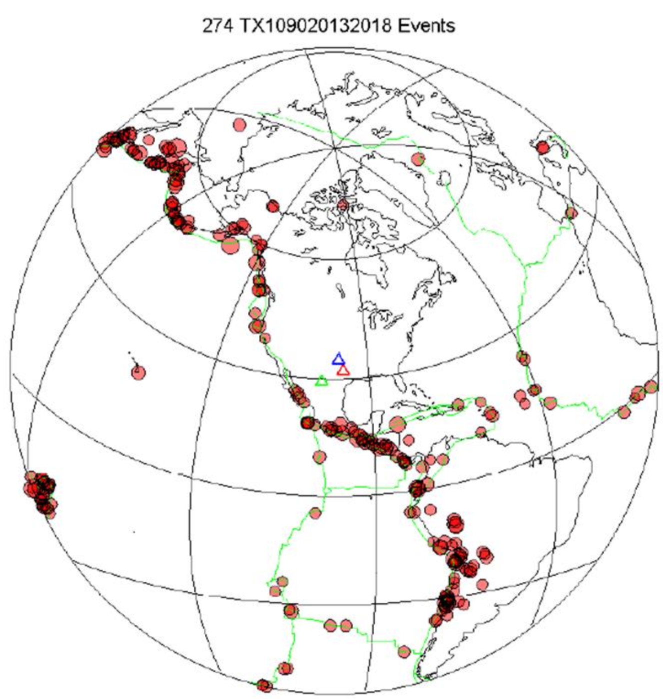

Figure 7. Locations of the remaining 274 events after the constraints described in the text were applied.

With these events, there is not good azimuthal coverage (Figure 8). In this case, most events are aligned to the southeast and northwest, with very few northeast located events. Southwest located events are almost exclusively at near 90° distance. Even without constraints, good azimuthal coverage is nearly impossible in this region of the world.

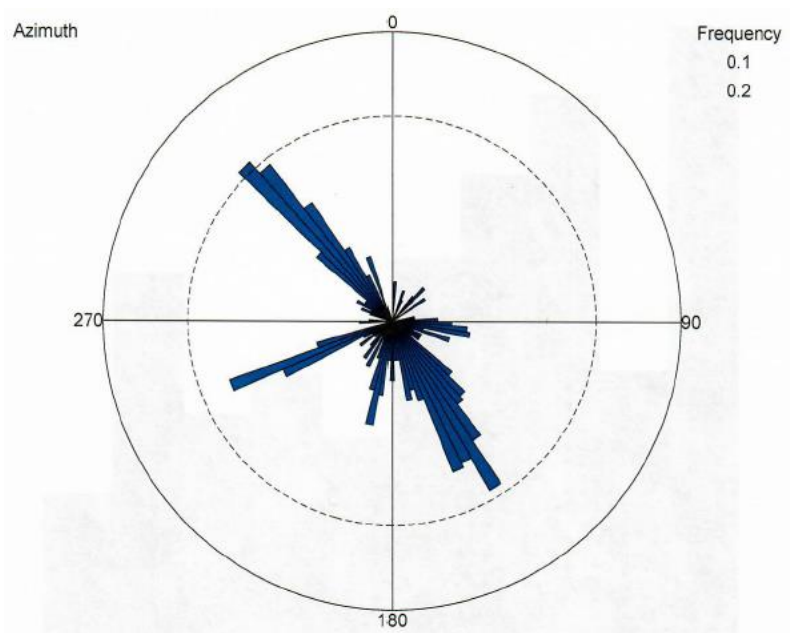

Figure 8. Rose diagram showing azimuthal coverage for the remaining 274 events.

Seismograms were downloaded for TX32, WHTX, and WMOK and a statistical summary is provided in Table 4. Altogether, there are 596 total events among three stations. Some of the events were eliminated due to unsuitable records, such as dead channels or transient noise issues. Some of the remaining events had very poor SNRs and also were eliminated. Table 4 separates the total number of events into 1) earthquakes with a magnitude ≥7 and 2) earthquakes with a magnitude between 6 and 7. 'Deep' corresponds to events >100 km, while 'Shallow' corresponds to events <100 km. 'Incomplete' events with insufficient data were discarded. ‘No P’, ‘No S’, and ‘No pP’ signify, respectively, events with no P-phase detection, no S-phase detection, and no pP-phase detection. ‘Bad’ corresponds to other problematic events that were discarded (generally due to transient noise). ‘Bad arrival’ corresponds to events with poor arrival picks when compared to nominal arrival times based on catalog origin times and an assumed Earth model (IASP91). ‘Fair or bad polarizations’ are events with polarization estimates that were not well defined in azimuth. The stations shared 103 reliable, common events; so, a subset of the data was taken to only include the common events, which was used in the analysis.

Table 4. Data obtained by each station.

Station	Total # of events	Deep	Shallow	Incom-plete	No P	No S	No pP	Bad	P-wave bad arrival	S-wave bad arrival	Fair or bad polari-zations
Statistics for all events with magnitudes ≥7 (count).											
TX32	19	6	12	8	1	3	16	1	0	3	0
WHTX	18	3	15	9	0	0	13	1	1	5	2
WMOK	15	4	8	12	3	3	11	1	0	2	0
Total #	**52**	**13**	**35**	**29**	**4**	**6**	**40**	**3**	**1**	**10**	**2**
Statistics for all events with magnitudes ≥6 and <7 (count).											
TX32	194	33	160	51	1	21	163	0	6	20	14
WHTX	167	28	121	78	18	18	124	0	5	17	10
WMOK	183	27	130	62	26	32	136	0	9	15	10
Total #	**544**	**88**	**411**	**191**	**45**	**71**	**423**	**0**	**20**	**52**	**34**
Grand Total	**596**	**101**	**446**	**220**	**49**	**77**	**463**	**3**	**21**	**62**	**36**

The basis of this research is not that the geology on Mars is comparable to the geology of Texas or Oklahoma, but, as will be done on Mars, a single seismic station will be used to locate events. The objective is to analyze how well a single station could perform this task, by acquiring homogeneous coverage of a hemisphere in both azimuth and distance. This effort is difficult because on Earth earthquakes occur in quasi-linear zones, rather than randomly distributed.

1.2.1 Station TX32

The TX32 seismic station is located about 14 km northeast of Lajitas, Texas, at the east side of the TXAR array. This village is situated on the Rio Grande in southwest Texas, along the northwest edge of Big Bend National Park (Li et al., 1984; Li, 1981; Sandidge-Bodoh, 1989). The distance from major cities makes this region seismically quiet and permits high SNRs at the site (Li, 1981).

This station is located in the Basin and Range/Rio Grande Rift extensional tectonic zone (Figure 9) which has a relatively north-south structure that extends into the mantle. A series of horsts and grabens produce mountain ranges and deep Cenozoic basins. This station sits on one of the horst blocks and is underlain by Mesozoic limestones, with minor amounts of shale and marl (Li, 1981; Li et al. 1984). Northwest of the Lajitas site, the Colorado Plateau separates the Basin and Range province from the Rio Grande Rift. To the south, the Basin and Range province and Rio Grande Rift are indistinguishable. The Rio Grande Rift formed through two phases of extension. The first major episode initiated in the late Oligocene and the second episode occurred in the Miocene, when there was major, rapid extension across the western US (Cather et al., 1994).

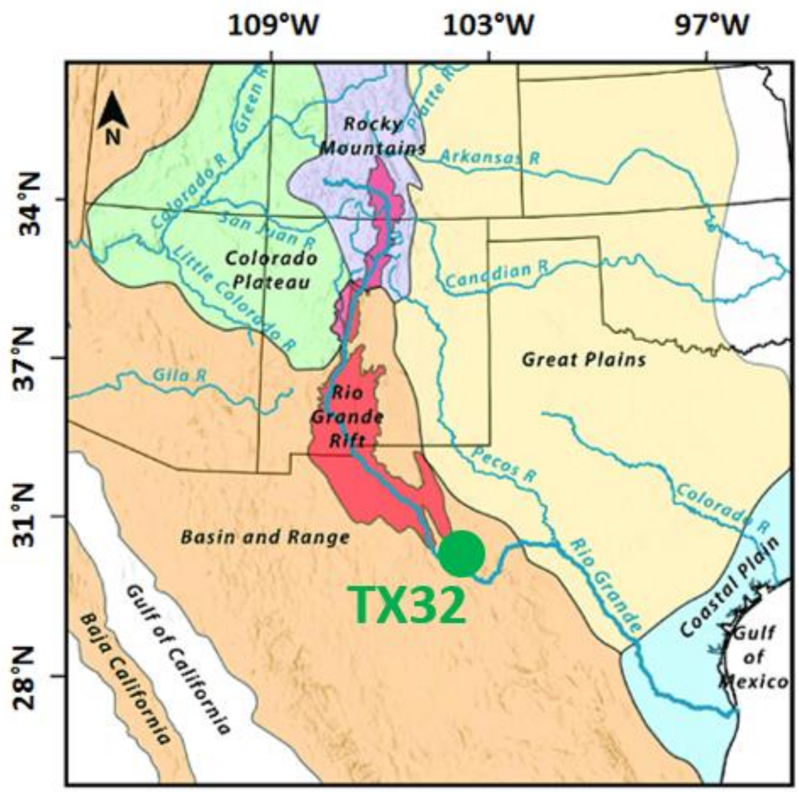

Figure 9. The Lajitas site Cenozoic tectonics (Repasch et al., 2017).

The Comanche Series includes Mid-Cretaceous thickly-bedded limestones of the Santa Elena Formation, the Lower Cretaceous shales, marls, and limestones of the Sue Peaks Formation, and the Lower Cretaceous cherty limestones of the Del Carmen Formation (Smith, 1970; Sandidge-Bodoh, 1989). A transect through Terlingua, TX, just east of the station (5.21 km distant), and the corresponding geologic cross section are shown in Figures 10 and 11.

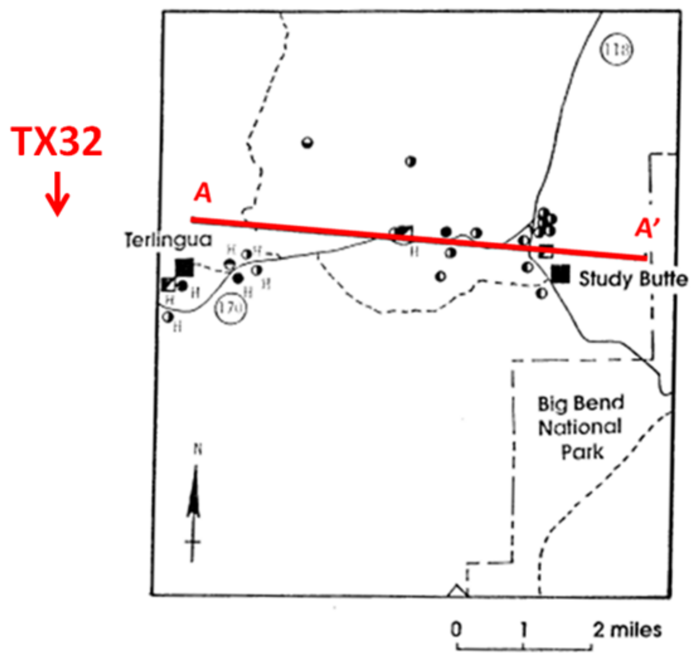

Figure 10. Transect through the Terlingua region (modified from Fallin, 1990).

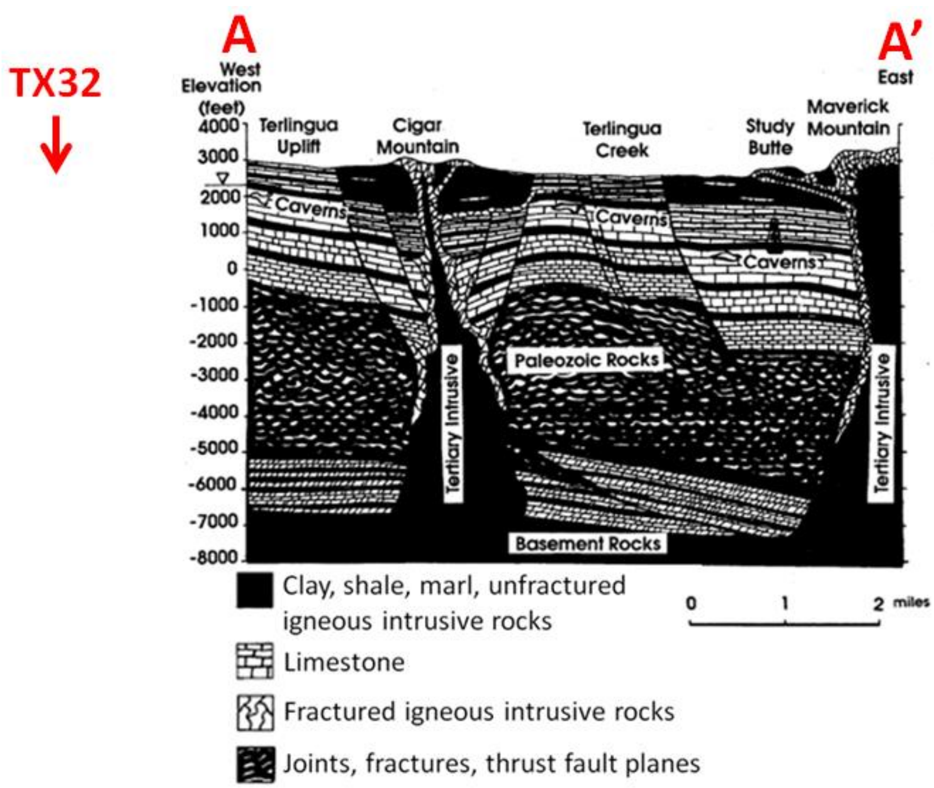

Figure 11. Terlingua region cross section (modified from Fallin, 1990).

Seismic tomography has been used to analyze lithospheric thickness variations and mantle structure and dynamics for the North American continent. Figures 12 and 13 show dramatic change from the western to eastern US, which reflects a transition in crustal and lithospheric thickness, which is located close to TX32.

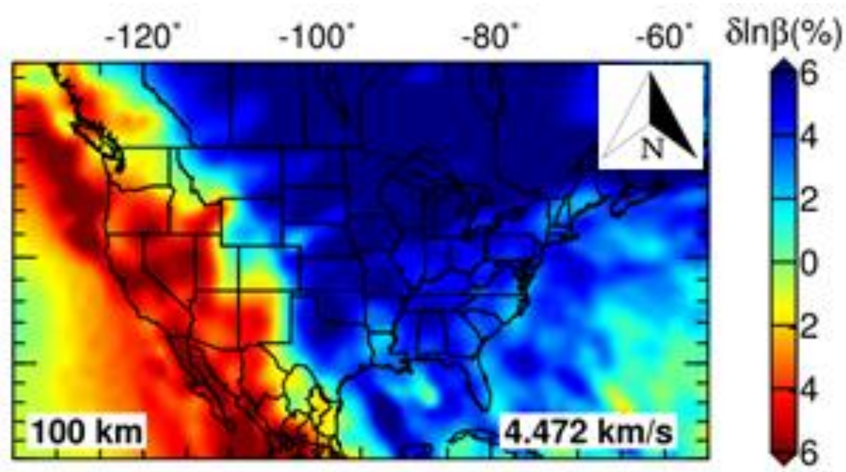

Figure 12. Seismic tomography results obtained from Zhu et al. (2017).

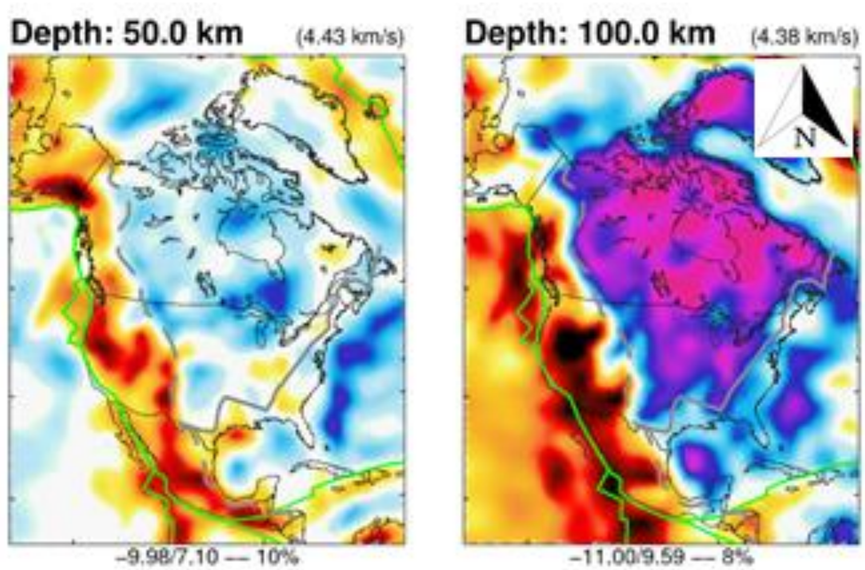

Figure 13. The seismic tomography results obtained from Schaeffer and Lebedev (2014). 50 km is the approximate thickness of the crust and 100 km is the approximate thickness of the lithosphere.

Tibuleac and Herrin (1997) provided a comprehensive review of azimuth calibration studies for the TXAR array. TXAR sits near a boundary that divides two areas with different geophysical properties, the Mid-Continent and Basin and Range Provinces. Therefore, they attempted to correct azimuth and phase velocity to reduce bias when locating events using the TXAR array (Tibuleac and Herrin, 1997).

The seismic velocity structure at this site includes limestones with relatively high seismic velocities (Figure 14).

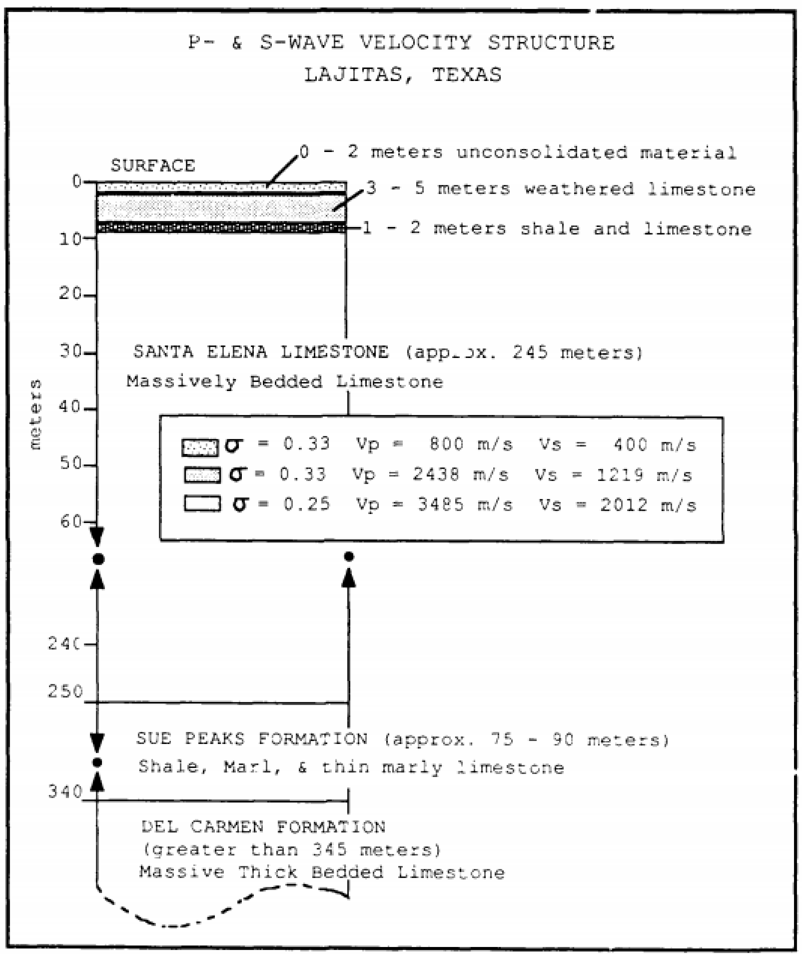

Figure 14. Seismic velocity structure for the Lajitas site (Sandidge-Bodoh, 1989).

Initially, a different station from the TXAR Array Network was used. TX31 is located very close to TX32, situated only 30 meters away. TX31 yielded large azimuth errors and a large systematic orientation error; therefore, attention was shifted to TX32. Figure 15 shows TX31 and TX32.

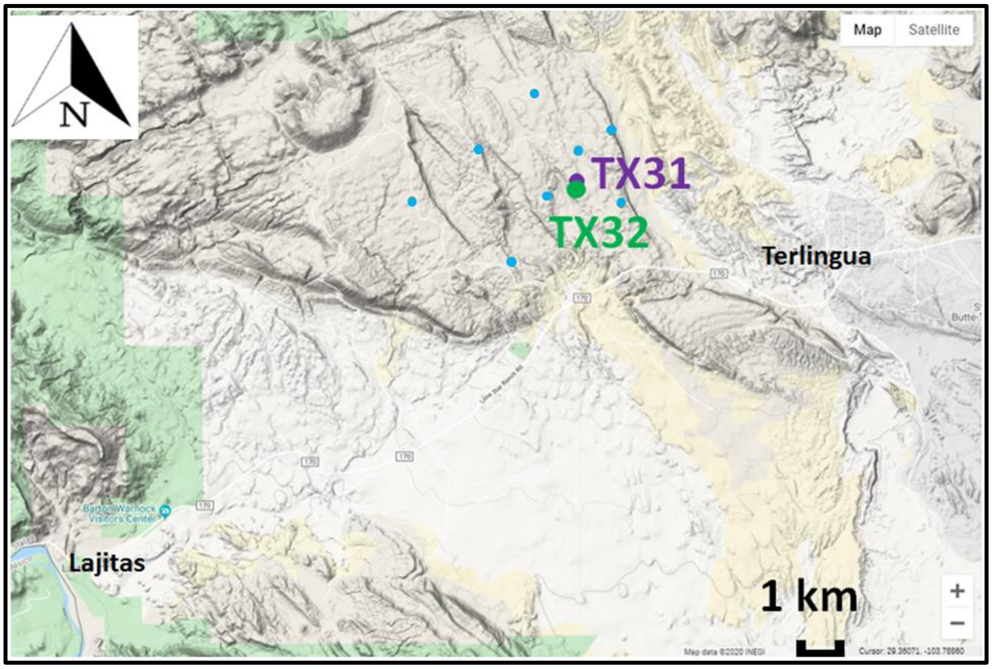

Figure 15. Location map for TX31 and TX32 near Lajitas, Texas. The light blue dots are other TXAR array stations.

1.2.2 Station WHTX

The WHTX seismic station is located near Lake Whitney in central Texas. Lake Whitney is a reservoir that branches off the main stem of the Brazos River. The Whitney Dam was built for flood control and power production. The construction of the dam resulted in Lake Whitney (Byars, 2009; Ruesink, 1977; Spencer, 1966).

This part of central Texas lies in the Great Plains Province, which is also called the Grand Prairie region. Miles of dry prairies stretch across the eastern region. To the west, the Grand Prairie is comprised of flat or gently sloping southeastward topography (Hull, 1951; Wermund, 1996). Rolling and undulating topography is typical for this area (Hull, 1951; Hill, 1901). Where bedrock limestone is cut by streams, rougher topography is observed. The westward plateau-like landscape has undergone erosion that has caused this surface to become well exposed (Hull, 1951; Wermund, 1996).

In the Late Cretaceous, this region was covered by shallow, inland seas**.** Throughout the Paleozoic and Mesozoic, the Interior Plains was a relatively flat, stable area of tectonic stability. In the Jurassic, sea level increased, and flooded most of the Great Plains. Continued sedimentation occurred over millions of years (Bureau of Land Management, 2009). The Balcones Fault trace is east of the Great Plains. The East Texas Basin is to the east, and the Fort Worth Basin to the west. This station sits on a basement high.

The site location is underlain by Lower Cretaceous strata. These include the Georgetown Formation, the Edwards Formation limestones, the Comanche Formation limestones that are interbedded with shale, and the Brazos Terrace alluvium which is predominantly sand. The Georgetown Formation consists of 7 total members, but only two are present in the dam area: 1) the Duck Creek Limestone Member and 2) the Kiamichi Shale Member (Byars, 2009; Brown, 1971). The Edwards Formation presents as massive beds of resistant limestone interbedded with softer beds (Kocher, 1916). The hardness and massiveness of the Edwards Limestone has resulted in the preservation of features like the Edwards Plateau (Byars, 2009; Kocher, 1916). The Edwards Limestone is responsible for the topography observed in the region. Low hills or mesas are topped with Edwards Limestone while the Comanche Peak Limestone makes up the slopes (Byars, 2009). A transect through the Whitney Reservoir and the corresponding geologic cross section are shown in Figures 16 and 17.

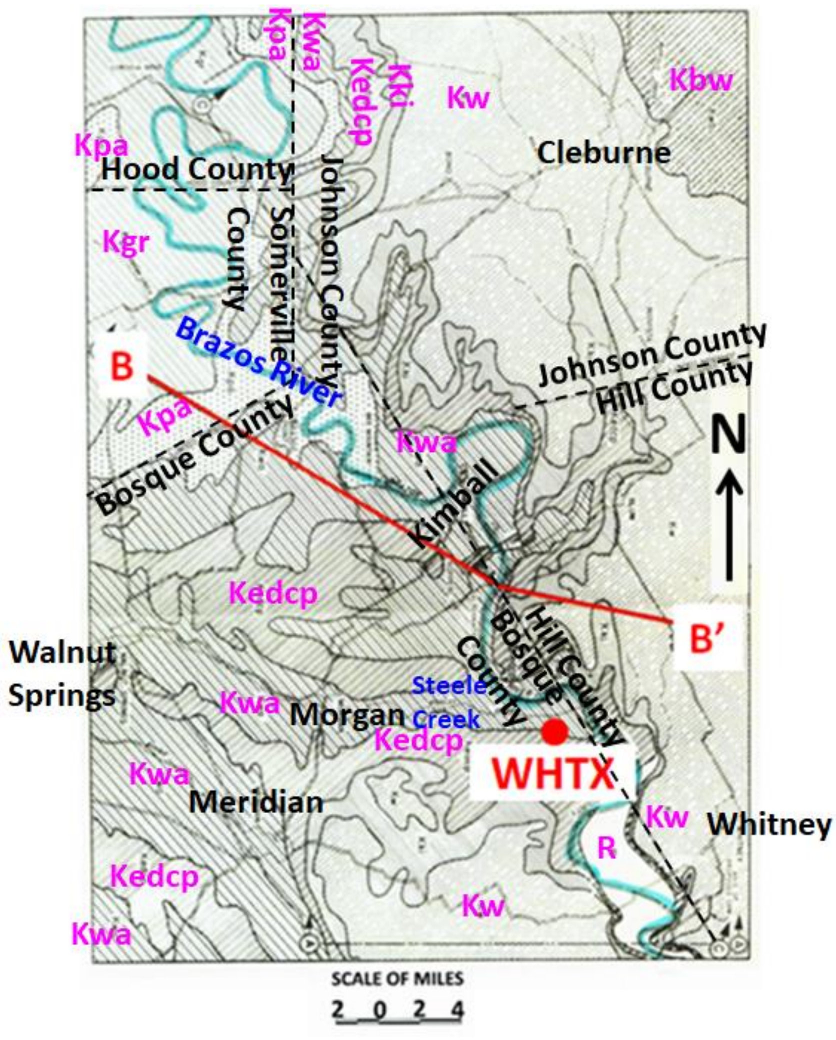

Figure 16. Transect through the Whitney Reservoir (modified from Hull, 1951). The Brazos River is light blue. Counties and cities are black. Formations are magenta. R- Recent Alluvium & Terrace Deposits; Kwb- Woodbine; Kw- Washita; Kki- Kiamichi; Ked- Edwards; Kedcp- Edwards & Comanche Peak; Kcp- Comanche Peak; Kwa- Walnut; Kpa- Paluxy; Kgr- Glen Rose.

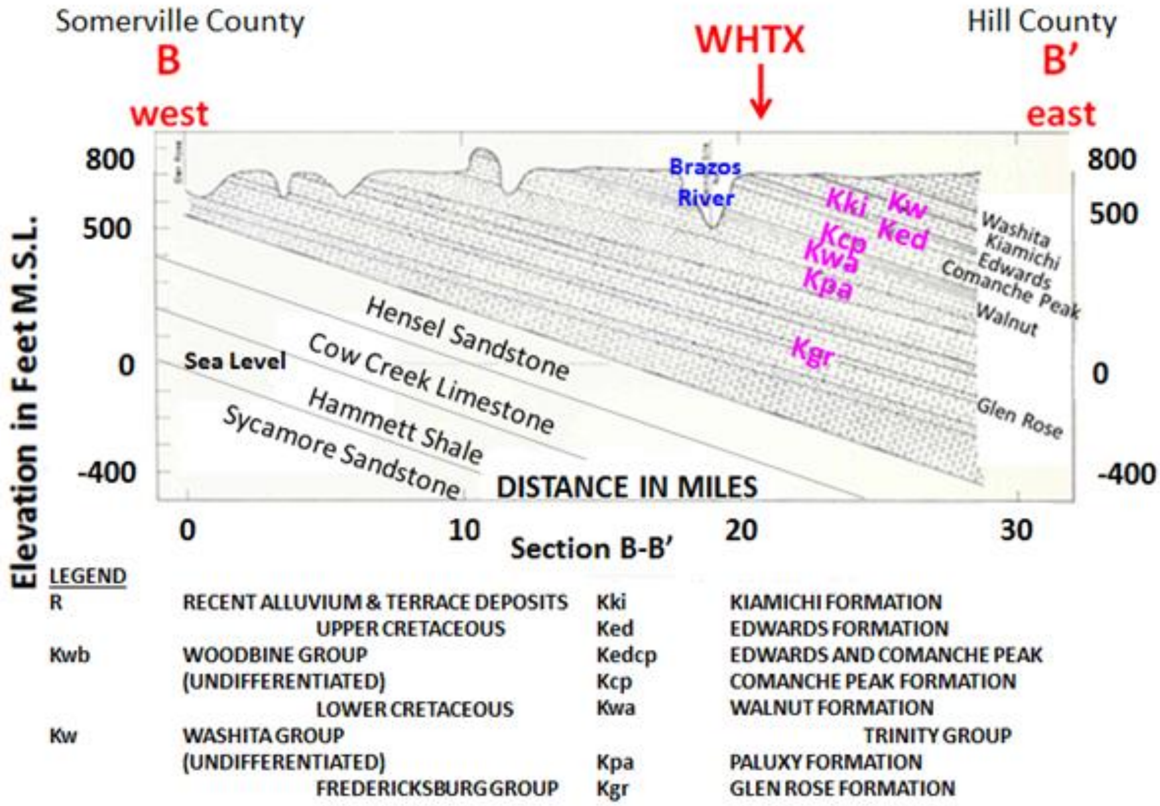

Figure 17. Whitney Reservoir cross section (modified from Hull, 1951).

Like TX32, the seismic velocity structure at this site includes limestones with relatively high seismic velocities (Figure 18).

Initially, a different station in central Texas was used. FW05 is located at the University of Texas at Dallas, situated 129.3 km northeast of WHTX. Due to its urban location, there is a high level of noise at the FW05 site; therefore, attention was moved to WHTX. Figure 19 shows FW05 and WHTX.

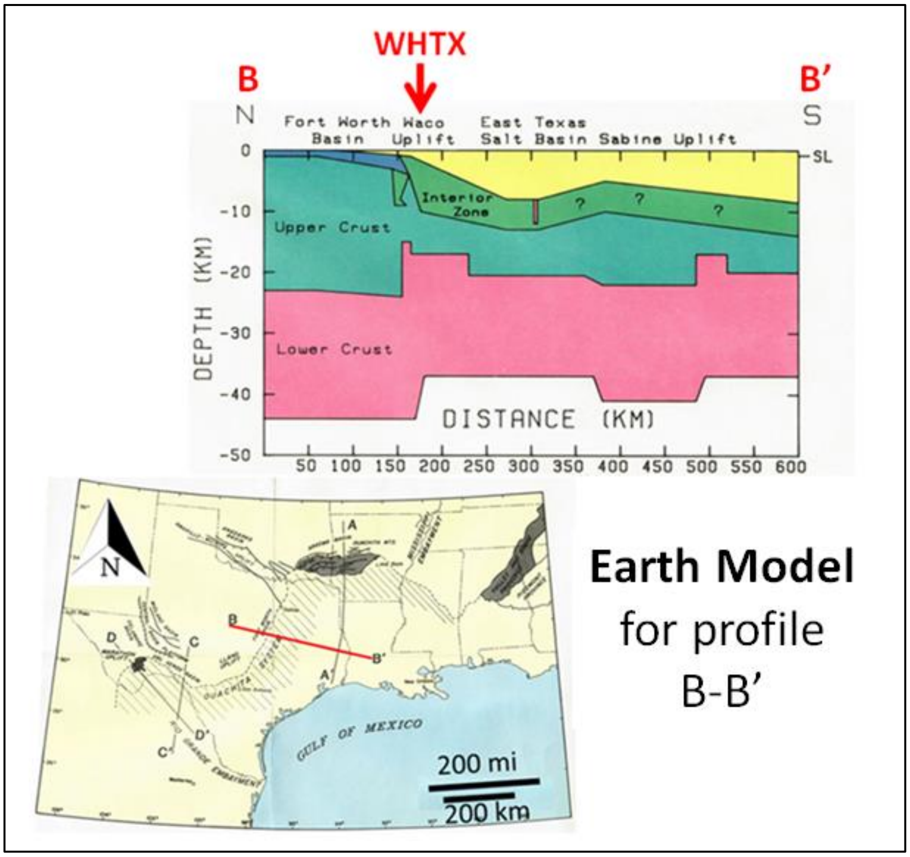

Figure 18. Seismic velocity structure for Lake Whitney (Keller, 1988).

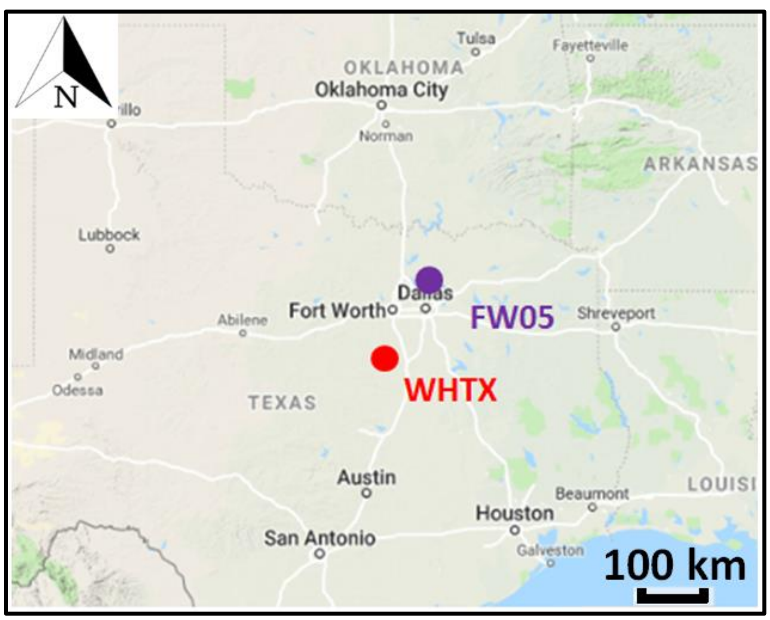

Figure 19. Location map for FW05 and WHTX in north central Texas.

1.2.3 Station WMOK

The WMOK seismic station is located in southwestern Oklahoma in the Wichita Mountains, one of the principal mountain belts of Oklahoma. This northwest-southeast trending structure is the result of Pennsylvanian uplift and the associated folding and faulting of rocks (Price at al. 1995; Johnson, 2008). During the Cambrian, lithospheric extension and rifting of the Laurentian supercontinent occurred. This resulted in the formation of the Southern Oklahoma Aulacogen and the initiation of igneous activity (Price at al., 1995; Mankin, 1997). In the late Paleozoic, compressional forces deformed this aulacogen, resulting in the formation of the Wichita Uplift and Anadarko Basin (Soreghal et al., 2012; Mankin, 1997).

The Anadarko Basin is a foreland basin that began to develop during the Ouachita Orogeny in the Late Mississippian. The WMOK site is characterized by a northwest-southeast tectonic strike, major thrust faults, and the Southern Oklahoma Aulacogen. The site sits on the upper plate of a major thrust fault.

Cambrian magmatism resulted in igneous rocks, predominantly granite, rhyolite, gabbro, and anorthosite, which can be observed in the northwest-trending segment of the mountain belt (Johnson, 1974; Johnson 2008). Early Paleozoic subsidence resulted in sedimentary rocks, predominantly limestone and dolomite (Kushner et al., 2017). These once covered the igneous rocks but have been eroded from many regions of the mountain range (Johnson, 1974). A transect through the Wichita Mountains and the corresponding geologic cross section are shown in Figures 20 and 21.

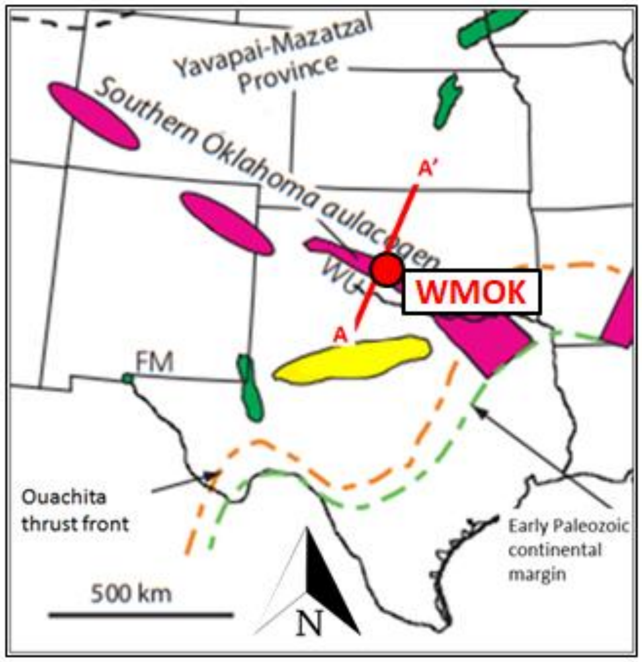

Figure 20. Transect through the Wichita Mountains (modified Soreghan et al., 2012).

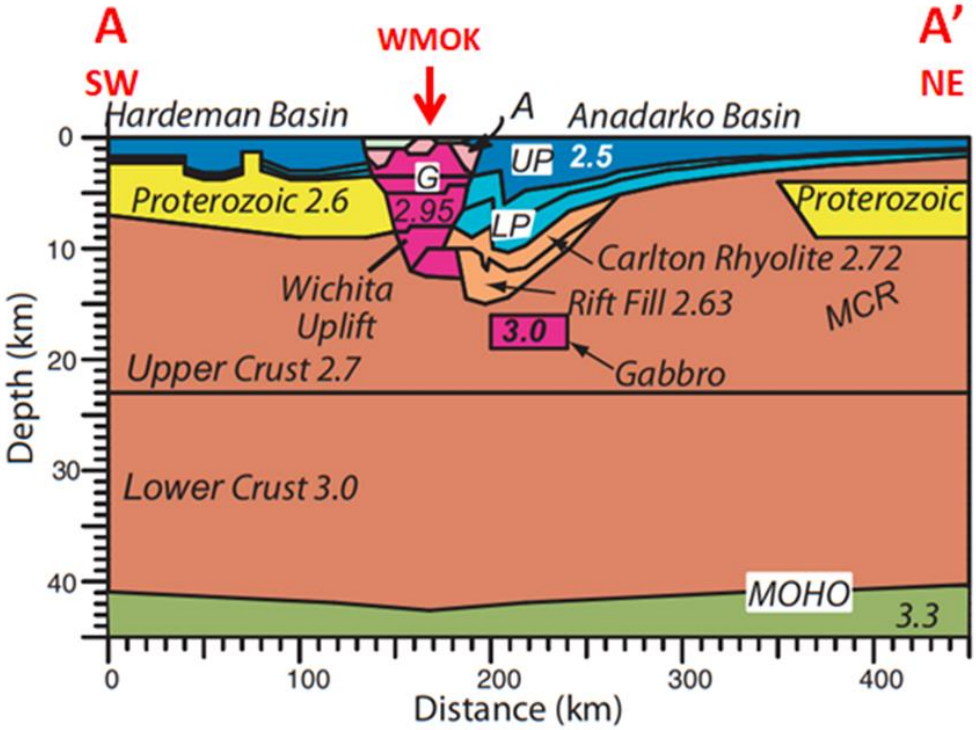

Figure 21. Wichita Mountains cross section. Densities are g/cm^3 (modified from Soreghan et al., 2012).

The seismic velocity structure at this site includes igneous rocks that have very high seismic velocities (Figure 22). The station sits on a basement high underlain by entirely igneous rocks, and no sedimentary structures.

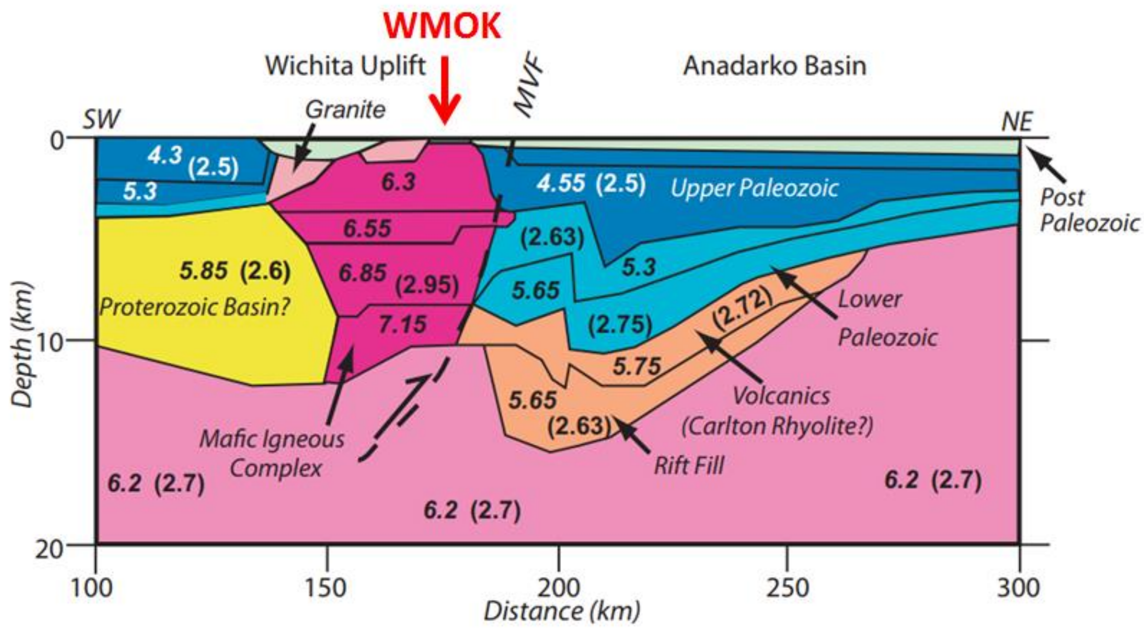

Figure 22. Seismic velocity structure for the Wichita Mountains. Seismic velocities are in km/s and the numbers in parentheses are densities in g/cm^3 (Soreghan et al., 2012).

1.2.4 Regional Geophysical Perspective

The USArray has homogeneous coverage of seismic stations over the United States to investigate the lithosphere and deep Earth structure (USArray, 2014). Three-component broadband seismograms can be converted into receiver function data, where shear-wave splitting (SWS) measurements are made to analyze the mantle structure beneath the US (Bashir et al., 2011; Gao et al., 2008). Figure 23 portrays the major tectonic provinces of North America (black lines). With the compilation and analysis of USArray data, mantle anomalies have been analyzed. Figure 23 shows how velocities in the upper mantle depart from the IASP91 model.

TX32 is the green dot, WHTX is the red dot, and WMOK is the blue dot.

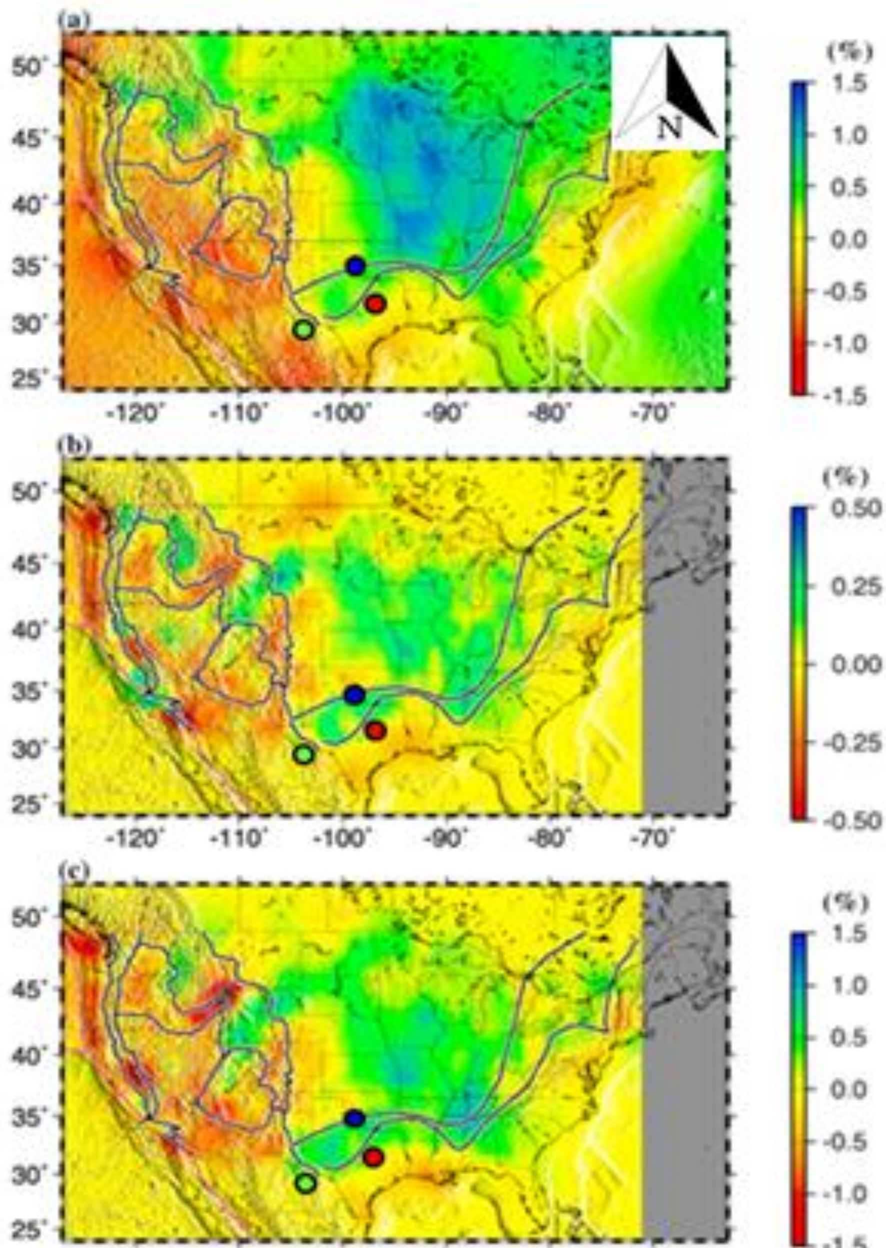

Figure 23. Mean velocity anomalies in the upper mantle. (a) is Vp obtained from Burdick et al. (2014), (b) is Vp obtained from Porritt et al. (2013), and (c) is Vs obtained from Porritt et al. (2013) (modified from Gao and Liu, 2014).

The proximity to the upper mantle anomalies affects V_p and V_s measures. All stations are located near the edges of the green anomaly, indicating that they are all affected by velocity anomalies to some degree. All three stations have some degree of heterogeneity in the crust and mantle.

CHAPTER 2

TRAVELTIMES OF SEISMIC PHASES WITHIN THE EARTH

Roughly, the Earth is in spherical shells from the inner core, outer core, mantle, and crust. Distinct traveltime branches are observed for both P and S body waves. Figure 24 portrays the Earth with the nomenclature for raypaths.

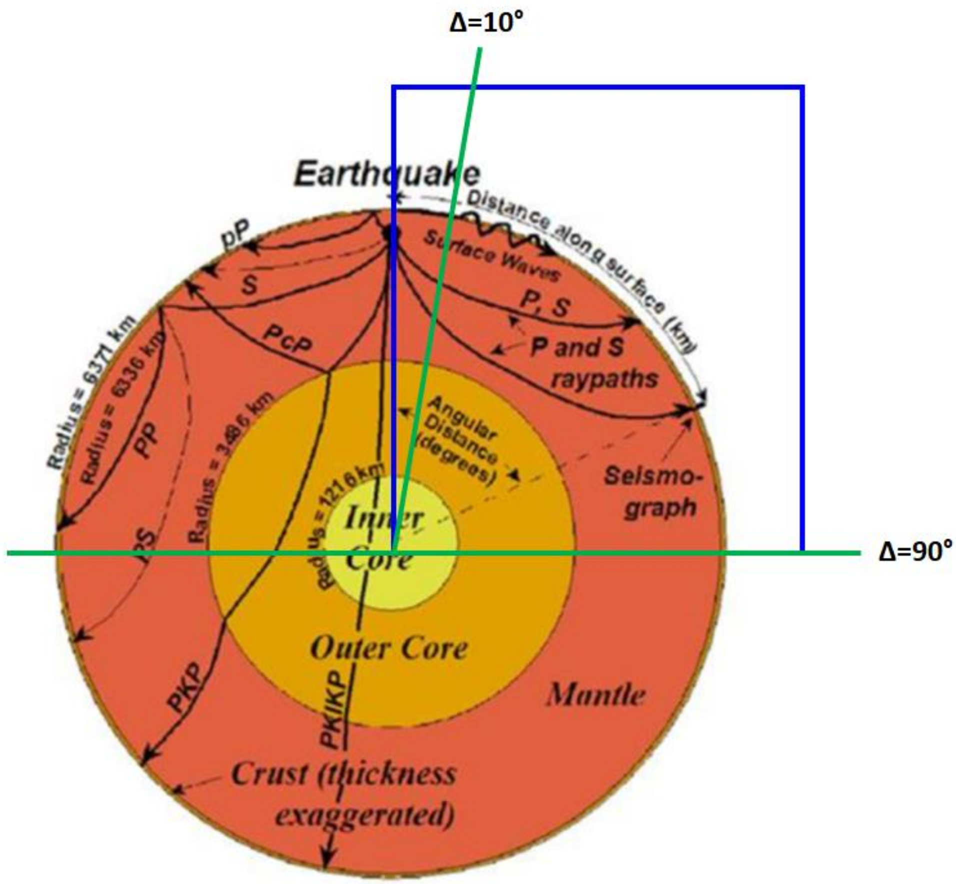

Figure 24. Seismic phases within the Earth (modified from Braile, 2007).

The traveltime branches portrayed in Figure 25 are associated with the named raypaths. This research focuses on P- and S-phases. There is potential use for reflected branches (i.e. PcP); however, this research does not include them.

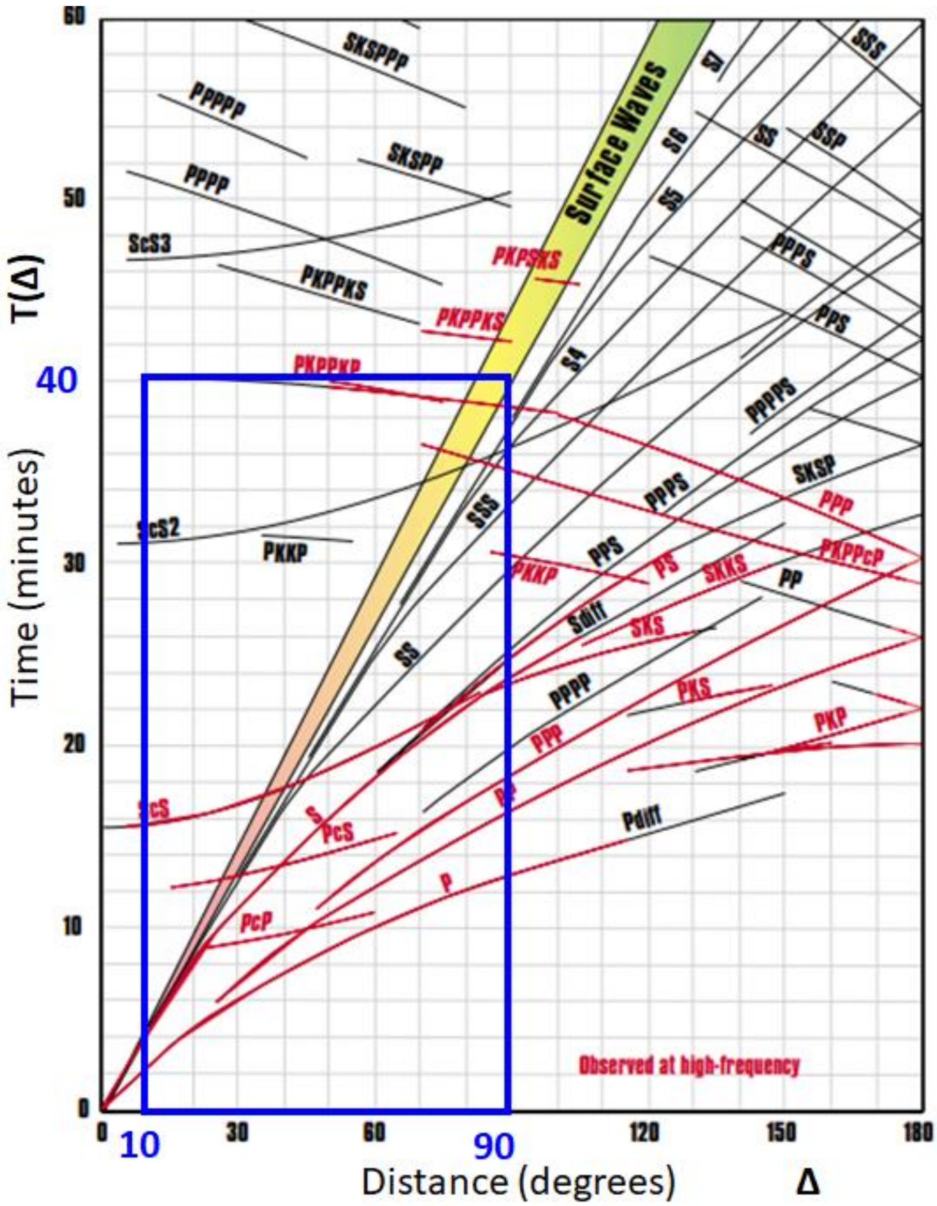

Figure 25. Traveltimes for various seismic phases within the Earth (Astiz et al., 1996). The data window extends to 40 minutes.

Potential arrivals are inside the blue box in Figures 24 and 25; these are rays that turn in the mantle or are reflected, particularly P, S, and pP. The blue box is related to the data window. The data window is 3600 seconds (1 hour long), with 1200 seconds (20 minutes) before the origin time to obtain a pre-event noise sample, and 40 minutes beyond origin time.

In this experiment, we exclude events <10° and >90° in angular distance. Events <10° have raypaths in the crust and upper mantle are not captured well by a global model. These events would need a local model. Below 90°, mantle arrivals before 20 minutes are relatively simple. Beyond 90°, raypaths extend into the core and there are numerous traveltime branches from both directions. For this research, complexity was avoided.

One-dimensional Earth models are spherically symmetric averages over lateral structure in the Earth. They gloss over differences in oceanic versus continental areas, subduction zones, etc. There is generally good agreement (to within seconds) for global traveltimes. Global 1-D reference models include PREM, IASP91, and AK135 (Dziewonski and Anderson, 1981; Kennett and Engdahl, 1991; Kennett, Engdahl, and Buland, 1995; Montagner and Kennett, 1995). 1D models are not entirely correct but useful.

PREM was produced by Dziewonski and Anderson (1981) and uses oceanic and continental alternate models. PREM also includes anisotropy in the upper mantle. IASP91 was produced by Kennett and Engdahl (1991) and is a global average with no ocean or continental variations and no anisotropy. AK135 was produced by Kennett, Engdahl, and Buland (1995) and is an improved version of IASP91 that combines continental, average Earth, and ocean. AK135-F is a variant of AK135 produced by Kennett, Engdahl, and Buland (1995) and Montagner and Kennett (1995). For the AK135-F traveltimes, refer to Research School of Earth Sciences (2009).

The velocity model is used two ways. Based on the catalogue location and origin time, the nominal traveltimes (i.e. IASP92 traveltimes) are computed. Also, the same model is used to compute traveltimes to obtain events locations

Bullen and Bolt (1985) present well known integral relationships among $V(r)$, Δ, T, τ, and p. $V(r)$ is a radial velocity function that can be computed for P and S (i.e. $V_p(r)$ and $V_s(r)$). Δ is the angular distance (deg). T is the traveltime (s). p is the slowness which is the slope of the traveltime curve (s/deg). τ is the delay time (s). For this program, Bullen and Bolt's (1985) approach is implemented where integrals can be directly numerically evaluated for Δ, T, τ, and p for any particular ray path, from the velocity model.

Buland and Chapman (1983) provide an alternate method of computing traveltimes. Equation (1) is a linear relationship of traveltime as a function of slowness:

$$T(p) = \tau(p) + p\Delta(p) \tag{1}$$

where slowness is (Equation (2)):

$$p = \frac{dT}{d\Delta} \quad (2).$$

Expressing the traveltime curve as a function of slowness defines τ. This method is also described by Kennett and Engdahl (1991) and in Kennett's (2001, 2002) books. Most modern researchers use the Buland and Chapman (1983) approach. Our direct numerical integration method has been compared and produced results in good agreement with the $\tau(p)$ approach.

This program implemented the IASP91 model, parameterized by P- and S-velocity models, portrayed in Figure 26 (Kennett and Engdahl, 1991). IASP91 was supposed to be a good average model of Earth for which traveltimes could easily be evaluated. It is commonly used today in global seismology. Possible alternate models would have been PREM and AK135.

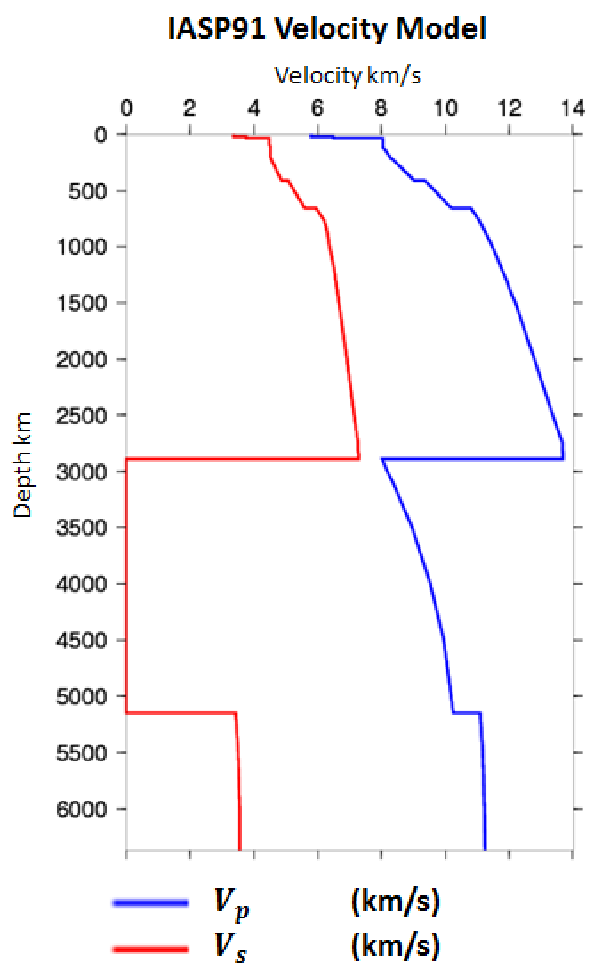

Figure 26. Kennett and Engdahl's IASP91 Earth model (modified from IRIS, 2011).

CHAPTER 3

METHODOLOGY

There is a chronological order of procedures involved in the single-station event location process: signal detection, arrival determination, and polarization analysis. This review is organized in this manner. Much inspiration for this program stems from the work of Kennett and co-workers in the 1990's (Tong, 1995; Tong and Kennett, 1995; Tong and Kennett, 1996; Leonard and Kennett, 1999; Leonard, 2000; Bai and Kennett, 2000; Bai and Kennett, 2001).

A hierarchy of windows is used in the program. The processor sequentially focuses on smaller time windows to determine arrival time and polarization. Events are downloaded from https://earthquake.usgs.gov/earthquakes/search/. For selected events, digital seismograms are obtained starting 20 minutes before and 40 minutes after the origin time. Local frequency, f_L, is determined by smoothing an instantaneous frequency estimate with a 1 second boxcar window. Short and long signal (STA and LTA) exponential windows are time adaptive based on the local frequency (Tong, 1995; Tong and Kennett, 1995; Tong and Kennett, 1996; Magotra et al., 1991; Withers, 1998). The sizes of these are adjusted; however, the ratio of the long to short term length segment is 12 to 1. Various detector channels "trigger" and remain in an "on" state defining so called detector windows. These detector windows may or may not actually correspond to a seismic signal; they are simply responding to a change in the data. The detector windows define a single detection window by their overlap. The arrival time could be on either side of the trigger time. Within the trigger window, many triggers will overlap one another. This window gives us an interval of time to search before and after the trigger for a specific arrival time.

The arrival time search makes use of a 12 second window containing the trigger time which should confine the arrival. Once an arrival time is defined, another noise window is obtained prior to the P-arrival and the phase window after the arrival time. These windows are used to analyze the power spectra and polarization. The phase and noise windows are the same size. The power spectra are obtained from signal and noise windows. The spectra are compared to define the SNR in the frequency domain. For the phase window, it is important to make sure the block of data is not too small or too big. Prediction error filters are propagated from the noise model forward and the signal model backward in order to determine an arrival time (Kennett and Leonard, 1999). Figure 27 shows an example of a seismogram with the noise, signal, and polarization windows.

The phase window is then refined to obtain a polarization window. The polarization window is optimized for polarization stability and yields the azimuth and inclination off the arriving wave. However, successful determination of an arrival time can be used to define the presence of a signal. If an arrival detection is not obtained, the window is discarded. If an arrival detection is obtained, then polarization analysis begins. Next, that arrival is characterized by its polarization state spectra and other measures. Initially, there is a search for the P-wave. Once a P-wave is obtained, search for an S-wave later in the seismogram.

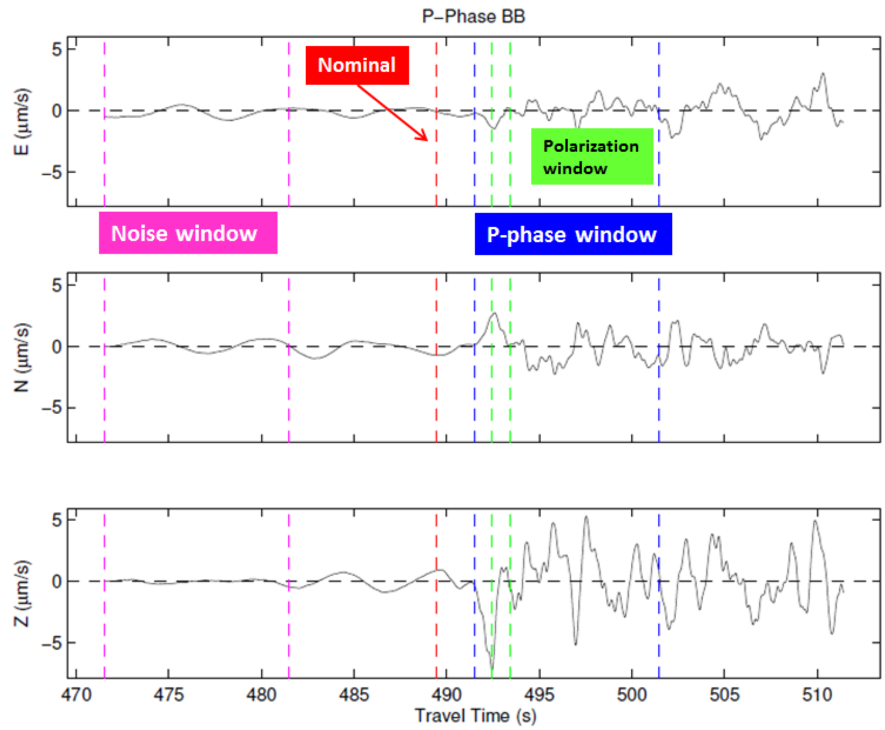

Figure 27. A seismogram with the noise and P-phase signal windows, as well as the polarization window. The red line is the nominal arrival time for the P-phase. For this processor, the P-phase window starts at the arrival pick.

3.1 Signal Detection

P- and S-phases in three-component seismograms are detected from a single station. The detections must be associated with particular raypaths and traveltime branches. Detection is accomplished by use of the short-term-average (STA) to long-term-average (LTA) ratio method applied to various signal property channels. Today, the STA/LTA ratio method is commonly used in global seismology (Trnkoczy, 2012). The STA measure has a shorter time window that yields information about when the seismic signal changes, indicating the presence of a seismic event. The LTA measure has a longer time window that yields information about ambient seismic noise (Allen, 1978; Earle and Shearer, 1994). When STA changes with respect to the LTA, that is when the local signal-to-noise can be estimated (Earle and Shearer, 1994). A predetermined threshold is set. When the ratio exceeds the threshold, an event is declared (Tong and Kennett 1995; Earle and Shearer, 1994). For this program, STA/LTA ratios are computed for both the energy and complexity to produce different signal detectors. The threshold is established by consideration of an F-test for a 95% confidence.

To detect that a signal has occurred, two different attributes of the signal are used: 1) the amount of energy locally in the signal and 2) the local complexity. The definition of 'local' is defined by the local frequency. The detectors adapt to the changing frequency in the noise and the changing frequency in the signal by changing the short and long window lengths (Tong, 1995; Tong and Kennett, 1995; Tong and Kennett, 1996). The window length is proportional to local period $T_L = 1/f_L$. Local frequency, f_L, can be determined from smoothed instantaneous frequency computed from the analytic seismogram. For this program, the instantaneous frequency operation is done in the frequency domain. This is discussed below.

The analytic seismogram is a complex time series consisting of the recorded seismogram and its Hilbert transform as represented in Equation (3):

$$s(t) = \mathrm{Re}(s(t)) + i\mathrm{Im}(s(t)) \qquad (3).$$

The seismogram $s(t)$ consists of a real part, $\mathrm{Re}(s(t))$, and an imaginary part, $\mathrm{Im}(s(t))$ (Claerbout, 1976; Bracewell, 1965; Yilmaz, 1987). The real part of $s(t)$ is the data; if the real part is needed, it can be extracted from the analytic seismogram. The Hilbert transform of $\mathrm{Re}(s(t))$is given by convolution (Equation (4)):

$$\mathrm{Im}(s(t)) = \frac{1}{\pi t} * \mathrm{Re}(s(t)) \tag{4}$$

which is simply an all pass filter with a 90° phase shift. $t$is time (s) and $*$ is the convolution operator. Because the Fourier transform of the Hilbert operator is known (Equation (5)):

$$\frac{1}{\pi t} <=> i\, sgn(\omega(t)) \tag{5}$$

$\mathrm{Im}(s(t))$ can be computed via the convolution theorem through a simple frequency domain manipulation (Claerbout, 1976). $<=>$ indicates a Fourier transform pair and $\omega(t)$ is the angular frequency (rad/s). For a discrete signal, Equation (3) can also be expressed in polar coordinates as seen in Equations (6) and (7):

$$s(t) = E(t) \exp[i\varphi(t)] \tag{6}$$

$$E(t) = [\mathrm{Re}(s(t))^2 + \mathrm{Im}(s(t))^2]^{1/2} \tag{7}$$

where $E(t)$ is the instantaneous amplitude or envelope and $E(t)^2$ is the instantaneous energy. The instantaneous phase angle $\varphi(t)$ (rad) is computed using Equation (8):

$$\varphi(t) = \arctan(\frac{\mathrm{Im}(s(t))}{\mathrm{Re}(s(t))}) \tag{8}$$

(Bracewell, 1965; Claerbout, 1976; Yilmaz, 1987). The phase angle is then used to obtain $\omega(t)$ using Equation (9):

$$\omega(t) = \frac{d\varphi}{dt} = 2\pi f(t) \tag{9}$$

(Claerbout, 1976). Discrete approximations to d/dt are unstable and amplify noise. Local frequency, $f_L(t)$, is found by averaging of instantaneous frequency, $f(t)$, over a short time window (1 second). The Scheuer and Oldenburg (1988) approximation is used for computing $\omega(t)$.

Earle and Shearer (1994) calculated the STA/LTA ratio using the envelope function. The envelope encloses an outline of the seismogram but has only positive values (Earle and Shearer, 1994).

There are several types of averaging windows that can be used. For this program, an exponential window was selected instead of a sliding boxcar window after a thorough evaluation by Withers et al. (1998). Equation (10) represents how the exponential window $\bar{u}(t)$ is computed. Equation (11) computes t_c, the time required for the exponentially decaying impulse response to decay by a factor of 1/e where Δt is the sample interval (s).

$$\bar{u}(t_i) = \beta\hat{u}(t_{i-1}) + (1-\beta)u(t_i) \tag{10}$$

$$t_c = {}^{-\Delta t}/_{\ln(\beta)} \tag{11}$$

β is related to the time constant t_c, which is related to the width of the window. The exponential window reduces transient energy effects (Withers et al. 1998). The exponential smoothing window is causal.

Tong (1995), Tong and Kennett (1995, 1996), and Magotra et al. (1991) also used an exponential window. The time constant t_c is related to the width of the window. t_c is also proportional to T_L = $1/f_L$. The time constant can be continually adapted as the frequency changes (Tong, 1995; Tong and Kennett, 1995; Tong and Kennett, 1996).

Automatic phase detection is accomplished by using the STA/LTA energy or complexity ratio. The lengths of both the STA and LTA window are frequency adaptive. Tong (1995) and Tong and Kennett (1995, 1996) determine ways to compute the total, horizontal, and vertical energy measures from the Z, N, and E seismograms and also different frequency bands, for instance low pass and high pass bands (Tong 1995; Tong and Kennett, 1995; Tong and Kennett, 1996; Earle and Shearer, 1994). This yields a family of detectors: for each channel and some channel combinations.

Ratios are also taken of the complexity. The length, $L(t_i)$, of seismogram s is measured between consecutive time samples and is a function of time t, as seen in Equation (12):

$$L(t_i) = abs(s(t_i) - s\ (t_{i-1})) \tag{12}$$

$$i, j = 1, 2, 3 \text{ or } i, j = E, N, Z$$

(Tong and Kennett, 1995). Length of the noise changes rapidly, while for the signal, it will start to change more slowly. The envelope of the length is measured to compute the complexity.

The complexity detectors are based on the fact that the signal has lower complexity when compared to the noise (Tong and Kennett, 1995; Tong and Kennett, 1996). The complexity detectors give information about the changes in frequency content. These detectors are useful for the enhancing the onset and providing better arrival times for small high-frequency signals (Tong and Kennett, 1995).

It is best to assess the output of a number of different detectors that are sensitive to different signal and noise characteristics. Multiple detectors can detect a wide range of signal characteristics.

The STA/LTA detector implemented in the program does not precisely confine an arrival time; it is only known that the signal occurred in a short window of time. The arrival time needs to be determined to a few samples, whereas the STA window is multiple samples. The detection alone does not provide an arrival time; there needs to be a modeling process to establish where the signal starts.

3.2 Arrival Determination

The arrival times for the detected phases are determined from autoregressive (AR) models of the time series. These methods can model both the signal and the noise, and hence, can be employed for signal-to-noise determination. Several authors including Takanami and Kitawaga, (1988, 1991, 1993), Leonard and Kennett (1999), Leonard (2000), and Bai and Kennett (2000, 2001) have discussed how the noise and signal of a seismogram can be modeled as an autoregressive process; which can then be used to estimate arrival times.

AR model fitting has been used to determine P and S arrival times. AR models are linear regression models where a future sample is predicted from preceding samples. The error at a specific point in time depends linearly on the previous errors (Leonard and Kennett, 1999).

Equation (13) represents a digital time series where s_t is an AR model of order p if it satisfies the equation:

$$s_t + a_1 s_{t-1} + a_2 s_{t-2} + \cdots + a_p s_{t-p} = \varepsilon_t \tag{13}$$

where $1, a_1, a_2, \dots, a_p$ are autoregressive model coefficients (a_0=1), and ε_t is uncorrelated Gaussian random noise (white noise) with a zero-mean and a finite variance σ^2 (Priestly, 1981; Robinson and Treitel, 1980; Leonard and Kennett, 1999). t is the time index. The coefficients are estimated by least squares using $N > p$ signal samples (there should be fewer coefficients than data points). Noise and signal samples of length N are modeled. Single- and multi-component AR modeling can be implemented for arrival determination of three-component seismic data. Equation (13) generalizes to a multichannel process where the process predicts channels from themselves and channels from each other. The AR model coefficients form a matrix. For this program, the Neumaier and Tapio (2001) multichannel approach is implemented for arrival picking. Wiggins and Robinson (1965) present an alternate method of the multichannel approach.

The AR model is a time series model but also characterizes amplitude, frequency, and phase information. The AR model can predict future time series values and can be used to form a prediction error filter which serves to deconvolve the modeled signal (Robinson and Treitel, 1980). The adaptive filtering attempts to predict the time series process and analyze for frequency and phase changes (Leonard and Kennett, 1999, Leonard, 2000).

An AR model can be built with p terms. If p is increased, the error is reduced, but if there is noise, a perfect prediction (i.e. $p = N$) is not desired. The question is: how many terms should be used? Somehow, the information content has to be measured. The goal is to only use as many terms as needed to capture predictable information, and to stop before the noise is over fitted.

The AIC (Akaike Information Criterion) statistic is a method used in time series analysis to obtain information about signal-to-noise ratio (SNR). The AIC measures how well the model fits the data but penalizes increasing the number of parameters. The "best" model produces the minimum AIC (Akaike, 1974). The AIC statistic is used in an iterative process of model fitting.

The AIC uses a modified maximum likelihood approach to derive the "best" order number using Equation (14):

$$AIC[p] = Nln({\hat{\sigma}_p}^2) + 2p \tag{14}$$

where p is the estimated AR model order, N is the number of data samples, and ${\hat{\sigma}_p}^2$ is the estimated white noise variance σ^2 at order p. The term $2p$ is the penalty for adding more parameters (Marple, 1987).

Rissanen (1983) introduced the MDL (Minimum Description Length). The MDL is a very similar idea to the AIC but penalizes in a different way as shown in Equation (15):

$$MDL[p] = Nln({\hat{\sigma}_p}^2) + pln(N) \tag{15}$$

where $pln(N)$ is the penalty. Kennett and coworkers use the AIC, however for this program, the MDL was implemented which is an improvement over the AIC. The MDL is implemented to inform when the filter is failing. There is a very distinct minimum that can be observed in the MDL statistic that marks the appropriate choice of p (Marple, 1987; Rissanen, 1983).

The MDL penalizes for too many terms. As the error goes down, the penalty goes up. These are added together to produce a minimum where they cross, as shown in Figure 28. Where the minimum occurs corresponds to the number of terms that should be used. A minimum indicates the presence of a good model.

The MDL is used twice to assess the model. First, the model is fitted by a least-squares process that minimizes the MDL to determine order p. The model predicts the data; the prediction is subtracted from the data to get the prediction error. The MDL is used again in the arrival determination. Failure of the prediction process for data not used in the model fitting can also be assessed by MDL (or AIC).

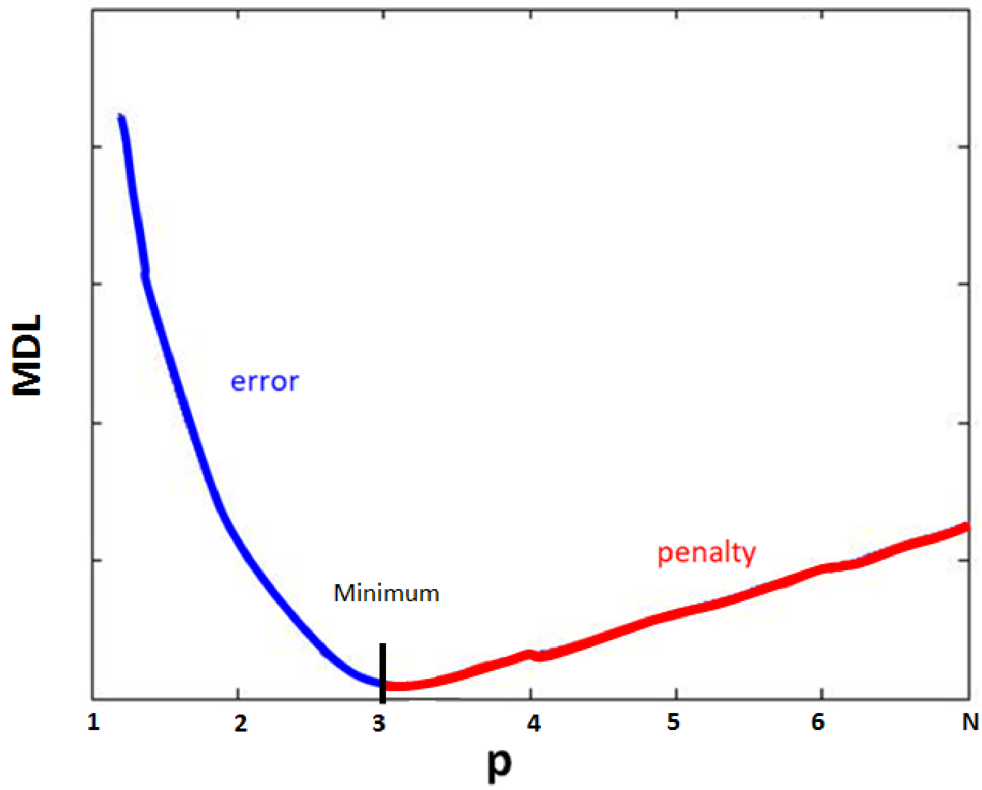

Figure 28. The MDL plotted against the model order p.

Takanami and Kitawaga (1988, 1991, 1993) compute two functions: 1) prediction in the forward direction using an AR model that represents the noise and 2) prediction in the backward direction using an AR model that represents the signal. These two statistics are combined to get a minimum MDL where the predictions fail at the same place (Leonard and Kennett, 1999; Leonard, 2000). The forward noise model fails at the signal and the backward signal model fails at the noise. Their method detects change from both directions. When the models cease to be good predictions, an arrival is declared (Takanami and Kitawaga, 1988; Takanami and Kitawaga, 1991; Takanami and Kitawaga, 1993). Figure 29 shows the noise and signal windows, as well as the trigger time and detector window.

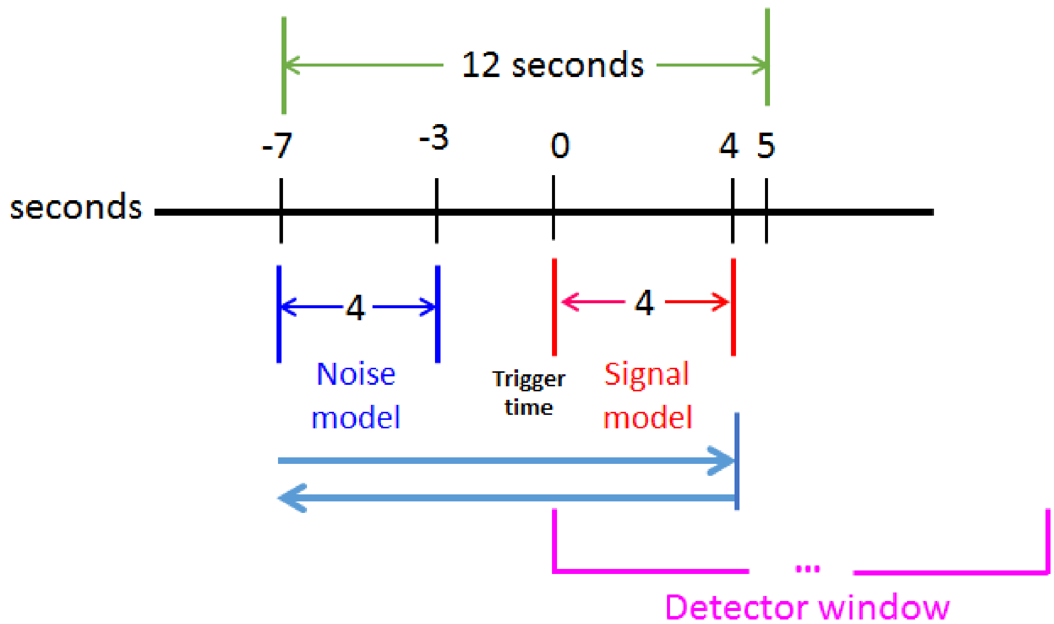

Figure 29. Windows associated with arrival time determination. The detection window extends to some unknown time (Kennett and Leonard, 1999; Leonard, 2000).

A good arrival time is crucial because the P- and S-arrival times are important for computing distance, and the P- and pP-arrival times for depth.

3.3 Polarization Analysis

Seismic waves are elastic waves that propagate through the solid material of the earth. These waves can be represented as time-variant particle-displacement vectors. Polarization describes the orientation of the particle motion. The P-wave moves back and forth in the direction of arrival. S-waves have particle motion that is orthogonal to the direction of propagation. Full vector motion of the ground is recorded by three-component instruments with orthogonal seismic detectors (E, N, Z). The orientation of the motion vector at the seismic station can be measured, which then yields the direction to the source of the waves.

Seismic motion can be represented with the eigenvectors of a 3x3 covariance matrix; this matrix is crucial for polarization analysis. Covariance is measured by averaging over a moving time window. As previously discussed in *Section 3.1: Signal Detection*, the same exponential window is used to smooth the covariance as the STA measure. As the frequency spectrum of the seismic data changes with time, the time window is adapted by changing its width. Computations for this analysis can also be performed using the Fourier transform of the covariance matrix - the power spectral matrix. Either way there must be a time-frequency resolution tradeoff and averaging results in both domains.

Time domain methods include the work of Magotra et al. (1987) and Madston (1990). Magotra et al. (1987) and Madston (1990) computed covariance matrix $\mathbf{C}$ to estimate the polarization direction for different phases (Magotra et al., 1987). Madston (1990) employed the time domain averaging method of Magotra et al. (1987) for the covariance matrix (Magotra et al., 1987). Time domain averaging needs to be frequency adaptive which, in turn, uses the local frequency described previously. A sliding exponential window was used to continuously update the covariance matrix. The covariance matrix can't be measured at a single point; it needs to be averaged over some kind of window. This is where frequency adaptive averaging is important. $\mathbf{S}$ is the multi-channel analytic signal with N rows and M columns, and hence, M channels (a matrix). The signal is assumed to be zero-mean. The covariance matrix is obtained by Equation (16):

$$\mathbf{C} = \overline{\mathbf{S}^{\mathrm{T}}\mathbf{S}} \tag{16}$$

which is now M rows and M columns. $\overline{\mathbf{S}^{\mathrm{T}}\mathbf{S}}$ is the exponential window averaged covariance matrix. This gives the covariance matrix in time, and therefore, gives eigenvalues and eigenvectors in time. For this program, the STA window was used to average. Preprocessing to remove a mean value or high pass filtering may be necessary.

$\mathbf{C}$ is the covariance matrix with components (Equation (17)):

$$\mathbf{C} = \begin{bmatrix} C_{ee} & C_{en} & C_{ez} \\ C_{ne} & C_{nn} & C_{nz} \\ C_{ze} & C_{zn} & C_{zz} \end{bmatrix} \tag{17}$$

The covariance, or equivalently the spectral matrix, can be expanded in the form (Equation (18)):

$$\mathbf{C} = \sum_{j=1}^{n} \lambda_j \mathbf{u_j} \mathbf{u_j}^{\dagger} \tag{18}$$

where λ_j and u_j are respectively eigenvalues and eigenvectors (Samson, 1980; Samson and Olson, 1981). The eigenvectors are complex and form an orthonormal basis (Olson, 1982). A wave in a pure state can represent all polarization information in the form of a single, non-zero eigenvector (Samson and Olson, 1980).

The P-wave has particle motion that is rectilinear. The P-wave is the first arrival, which can be very pure and is not complicated by other arrivals. Due to this, the P-wave provides the best estimate of source azimuth because it's not contaminated by P- and S- scattered energy. As time progresses, the source azimuth estimate becomes more unreliable. The S-wave appears after the P-wave in the seismogram. S-waves can have a combination of SV- and SH-wave motion. Typically, there is a combination of SV- and SH-waves that arrive at different times due to an anisotropic velocity structure. When out-of-phase with one another, there can be spiraling, elliptical motion. Polarization estimates are not as reliable for the S-wave because of this mixture of motions; however, they can still aid in the discrimination between P- and S-waves. P- and S-wave arrival times are necessary when locating events with a single station.

By looking at the eigenvectors and eigenvalues of the complex covariance matrix among the three channels, the polarization can be determined. There are three eigenvectors, where either one or two are related to signal motion and the remainder to noise variance.

The initial P-wave motion should be characterized by a single eigenvector, which is indicative of a pure state signal. This vector orientation in the horizontal (E, N) plane yields the source azimuth. The P-wave can be distinguished from other wave types by this pure state property.

Several different methods of polarization analysis for event location have been proposed. Some methods perform this analysis in the time domain, while others in the frequency domain.

Vidale (1986) used the full eigenvector approach to discriminate between arriving wave types (P-, SV-, and SH-waves have different polarization characteristics). The scalar measures below, Equations (19) and (20), are derived from covariance matrix and eigenvector decomposition:

$$\mathrm{P_S} = 1 - \frac{\lambda_2 + \lambda_3}{\lambda_1} \tag{19}$$

which measures the strength of the polarization in the signal. If $\mathrm{P_s}$ is near 1, this is indicative of a single eigenvector state. Eigenvalues (or eigenvariances) are $\lambda_1 \geq \lambda_2 \geq \lambda_3$.

Also:

$$\mathrm{P_P} = 1 - \frac{\lambda_2}{\lambda_3} \tag{20}$$

which measures planar polarization or a two-eigenvector state.

Jurkevics (1988) used covariance matrix decomposition to obtain the eigenvector $\mathbf{u_1}$which is has eigenvalue λ_1. These yield information about the P-wave azimuth and dip angle of the motion. The direction cosines of $\mathbf{u_1}$ (cosines of angles between $\mathbf{u_1}$ and (E, N, Z)) are shown in Equation (21):

$$\mathbf{u_{j1}} \qquad j = 1, 2, 3 \tag{21}$$

Azimuth and inclination are measured using Equations (22) and (23):

$$A = \tan^{-1}(\frac{\mathbf{u_{21}}}{\mathbf{u_{11}}}) \tag{22}$$

$$I = \cos^{-1}(\mathbf{u_{31}}) \tag{23}$$

Azimuth ambiguity must be resolved by consideration of both horizontal and vertical motion which could be either toward or away from the source (Magotra et al., 1987).

Samson, in a series of papers (1980, 1980, 1981, 1983, 1983), uses a frequency domain approach for polarization analysis of various types of signals. They assumed a pure state where a wave can be represented by a single eigenvector (Samson and Olson, 1980; Samson, 1983; Samson, 1983). Samson and Olson (1981) generated a data-adaptive polarization filter for multichannel seismic data, which enhances the waveforms of pure state data (Samson and Olson, 1981). Samson and Olson employ frequency domain averaging of Fourier transformed data in a moving boxcar window to estimate the power spectral matrix. The degree of pure state polarization, P, is a scalar measure that can be computed to design the time-varying filter as seen in Equation (23). Samson and Olson perform computations with the power spectral matrix, but it is also possible to use the covariance matrix in the time domain as demonstrated by Madston (1990). This formalism is directly applicable to the P-wave motion and the time domain approach is exclusively used in this research. Using $\mathbf{C}$, the degree of polarization P can be obtained using Equation (24):

$$\mathrm{P} = \frac{nchan(tr(\mathbf{C}))^2 - tr(\mathbf{C}^2)}{(nchan - 1)(tr\mathbf{C})^2} \tag{24}$$

where the number of channels $nchan$ = 1, 2, or 3. The $tr\mathbf{C}$ and $tr(\mathbf{C})^2$ are scalar invariants with respect to coordinate rotation (Samson and Olson, 1980; Samson and Olson, 1981). The orientation of the pure state eigenvector can be estimated without diagonalization of $\mathbf{C}$ (Samson and Olson, 1980). For a pure state, P = 1 (Samson and Olson, 1980).

3.4 Characterization

Is it a P- or S-wave? Is it a seismic signal or just transient noise? Characterization is based on measures in the phase and polarization windows. Factors to analyze include the SNR, peak frequency, and bandwidth which are obtained from the power spectra. S-waves often have lower SNR, frequency, and bandwidth compared to P-waves. Polarization provides various polarization measures, P, P_s, P_p, which makes discrimination between P- and S-waves possible (Samson and Olson, 1980; Samson and Olson, 1981; Vidale 1986). All of these signal characteristics can be used to attempt to answer the opening questions and determine the phase type. If a decision is made that an initial P-wave has been detected, then the azimuth is calculated. Next, a search is done for the pP-phase, which should follow within 100 seconds, and eventually, the first occurrence of an S-wave. Signal characterization should be capable of rejecting spurious detections (i.e. transient noise).

Estimation of the power spectrum was made using Thomson's (1982) multitaper spectral analysis method. The data samples $s(t)$ are multiplied by a set of orthogonal tapers to produce various single taper periodograms. To reduce the variance, these estimates are then averaged to determine the power spectral density. This technique was established as an alternative to averaging in the frequency domain (Prieto et al., 2007). The power spectra are used to characterize the signal and noise.

A P-wave indicator, P_{ind}, and an S-wave indicator, S_{ind}, are used in addition to polarization measures to distinguish between P-and S-waves. The P_{ind} uses the vertical energy, while the S_{ind} uses the horizontal energy (Tong and Kennett, 1995).

3.5 Azimuth

The computation of the azimuth is the most important part of the single-station event location process. The azimuth is calculated from the station to event location. Azimuth is the angle at the station clockwise from north to the great circle through the station and epicenter. Azimuth is determined from the pure state polarized initial P-arrival. S-wave azimuths are not useful due to their multi-eigenvector nature. With the determined azimuth and angular distance between station and epicenter, events can be located using spherical trigonometry.

We estimate the azimuth by polarization analysis of the P-wave arrival. Because P-waves are linearly polarized, a single eigenvector can determine the azimuth (Samson and Olson, 1980; Samson and Olson, 1981). For the S-wave, it is necessary to look beyond the first eigenvector and all of the eigenvectors are determined. The major axis vectors are averaged within the polarization window to obtain the azimuths shown below. Polarization is determined in a narrow time window selected for low variance of the azimuth. Azimuth is derived from the (E, N) components of the (E, N, Z) three-component seismogram. The signal association stage should find the pure state portion of the seismogram, associated with the P-phase, which the azimuth should then be computed from. This doesn’t work so well for the S-phase because there is a mixture of SH and SV motions.

3.6 Incidence Angle

The incidence angle is the angle tangent to the raypath and the vertical in the plane of the raypath (sagittal plane) as shown in Figure 30.

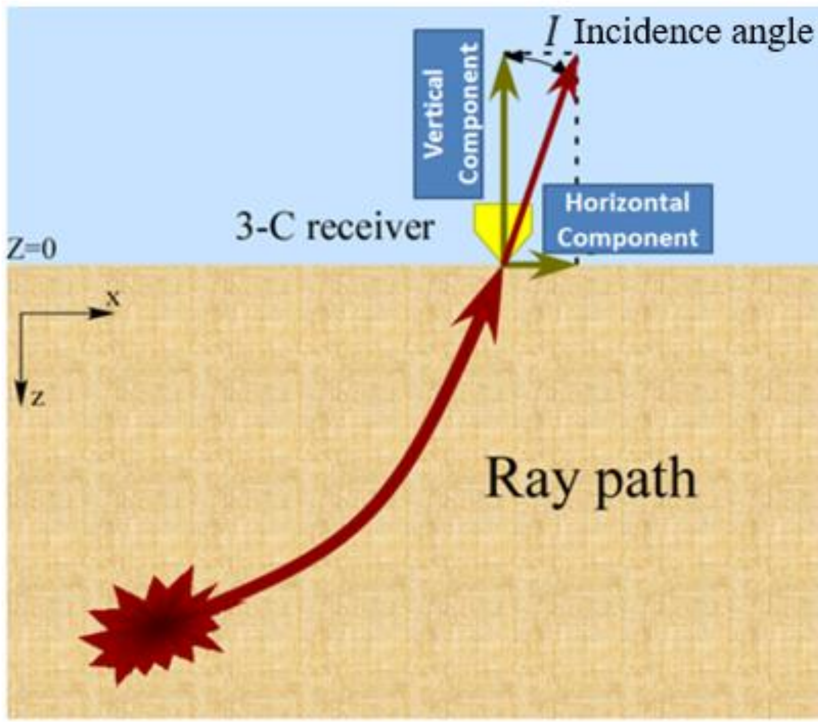

Figure 30. The incidence angle (modified from Kawabayaski et al., 2012).

After azimuth is determined, the seismograms can be rotated about Z from (E, N, Z) to (R, T, Z) by the angle $A - 90°$. The apparent incidence angle is then determined from the (R, Z) components. The true incidence angle is obtained from the apparent incidence angle using the free surface boundary condition (Kennett, 1991).

The apparent incidence angle is measured from the raw polarization analysis. The apparent incident angle would represent the true direction in an unbounded medium;

however, the free surface is problematic. The free surface interaction involves boundary conditions on the wave equation that cause mode conversion and coupling (Kennett, 1991). If the free surface coupling effects are removed, decomposition of wave types can occur and the P-, SV-, and SH-waves can be separated without distortion (Jepsen and Kennett, 1990). The apparent incidence angle has to be corrected to obtain a true incidence angle that's consistent with ray theory. The correct P and S velocities at the station, which are generally not known, are required for the surface correction.

3.7 Slowness

If the slowness is known, the distance to the epicenter (or hypocenter) can be determined by ray tracing in a 1D velocity model (Bullen and Bolt, 1985). Rays are refracted at the interfaces between subsurface layers of different velocity and in velocity gradients. Snell's Law can be expressed for a radially symmetric Earth where velocity increases with depth as seen in in Equation (25) (Aster, 2011). It can be written in terms of the local velocity and slowness as:

$$\frac{\sin(I)}{v} = p \tag{25}$$

where p is the ray parameter or horizontal slowness, which is constant along the ray path. The term I is the ray incidence angle corrected for free surface and v is the local velocity at the station (Shearer, 2009; Aster, 2011). In this study, incidence angle and slowness were found to be highly variable and unreliable estimates of Δ resulted.

3.8 Location from Azimuth and either Slowness or S-P Times

Epicentral distance can be determined either by slowness or S-P times. With a radial velocity model, horizontal slowness yields the epicentral distance and traveltime by ray tracing. Typically, within the Earth, velocity increases with depth. This gradient assures that rays will turn toward the surface. At the turning point the ray is traveling horizontally and the slowness is the reciprocal of the velocity ($1/v$). This is represented in Figure 31.

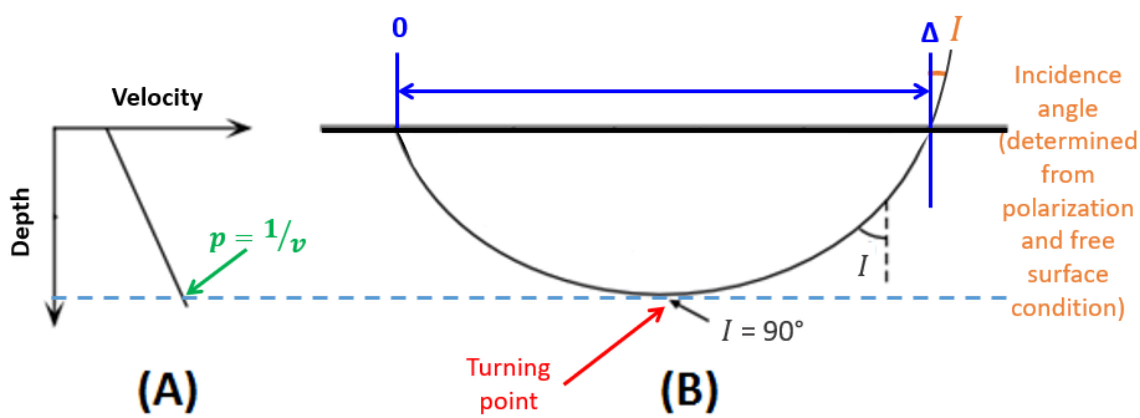

Figure 31. (A) is a model representing the Earth's general velocity increase with depth. (B) is a raypath turning toward the surface corresponding to model (A) (modified from Shearer, 2009).

Slowness, p, is determined from the incidence angle and Snell's Law (Figure 31), which requires the local, near surface velocity. Furthermore, the incidence angle must be corrected for P-SV conversion and the free surface (Jepsen and Kennett, 1990; Kennett, 1991; Tong and Kennett, 1995). If a slowness is determined, then a raypath can also be determined. With the horizontal slowness, the turning point can be obtained and Δ is computed for that raypath.

If there is an arrival time for the S-wave, determining the S-P time will yield the epicentral distance, shown in Figure 32. S-P times provide a more reliable way to measure the epicentral distance.

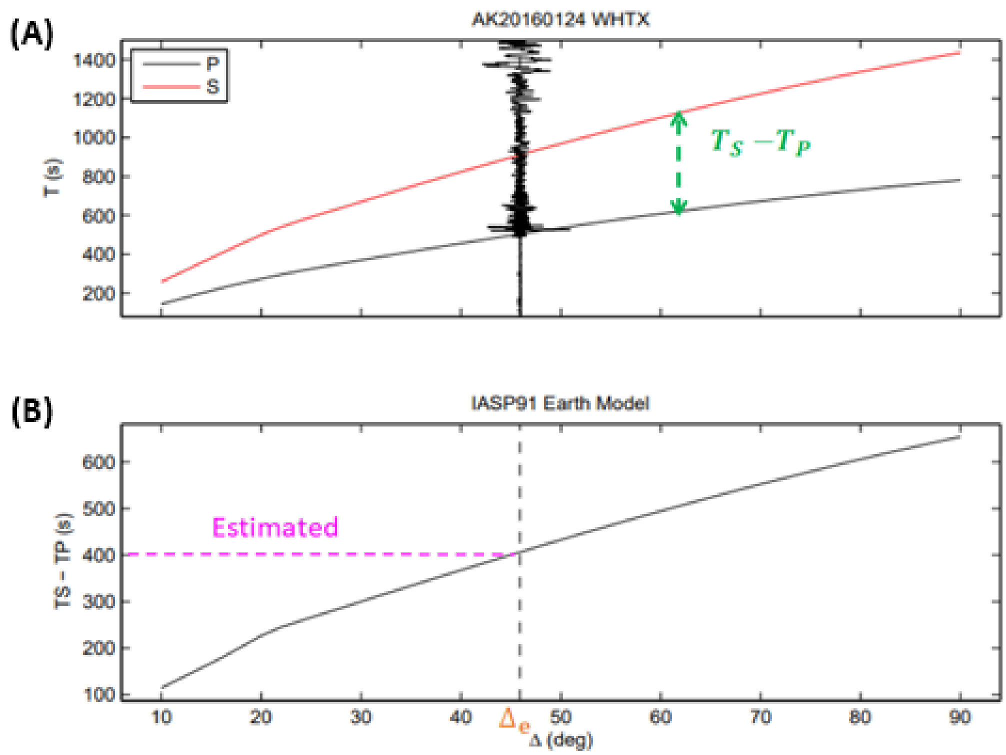

Figure 32.(A) Distance versus traveltime. The time interval between S and P gets bigger with distance. (B) Distance versus S-P time. An S-P time difference on the curve gives a distance.

Nominal locations are obtained from the ANSS catalogue, and the IASP91 model defines the nominal traveltimes. Also, data is downloaded from the https://earthquake.usgs.gov/earthquakes/search/, and the actual arrival traveltimes in those seismograms will be different. Arrival times, used to estimate distance, and polarization are determined through signal processing. Inversion from traveltimes can determine the distance.

Figure 33 shows that the latitude and longitude of the station, azimuth, epicentral distance, and traveltime yield the latitude and longitude of the event and origin time; this is the epicentral location.

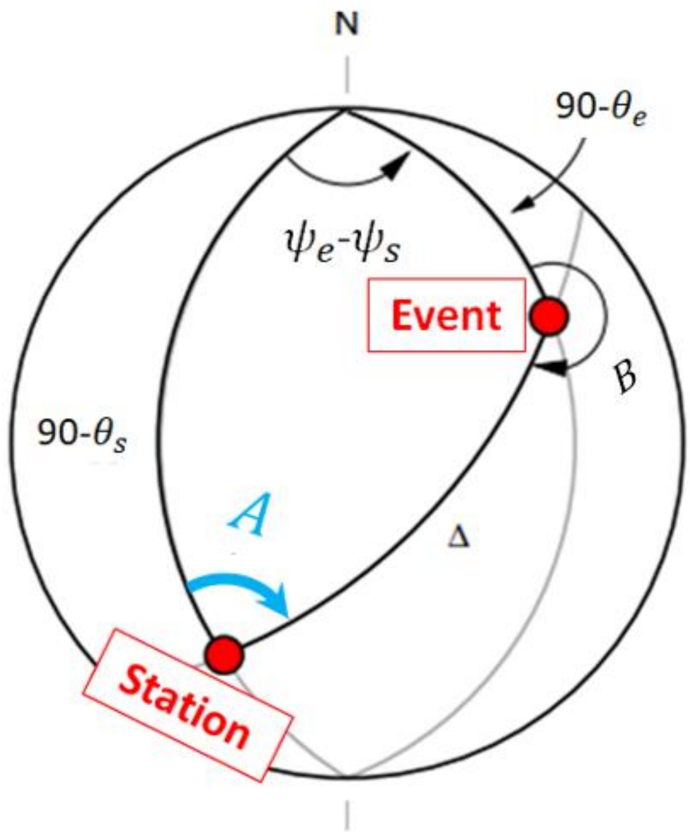

Figure 33. The station S and event E on a spherical Earth. The station has coordinates (θ_s, ψ_s, h_s). The event has coordinates (θ_e, ψ_e, d_e). A is the azimuth. B is the back azimuth. Δ is the angular distance.

For the hypocentral location of an earthquake, latitude and longitude of the event, origin time, and depth are necessary, which is determined from pP seismic phase arrivals. The epicenter is more accurate when the depth is known. Inclusion of depth and other phases besides P and S complicate the process somewhat, but the principle remains the same.

CHAPTER 4

REPRESENTATIVE EXAMPLE

The step-by-step methodology is described below along with images, Figures 34-45, of the process for a magnitude 7.1 earthquake near Old Iliamna, Alaska in January 2016. The earthquake has a distance from the nominal location in the catalogue to the station, WHTX, of 46° (or 5115 kilometers) and a depth of 129 kilometers. This earthquake occurred in a region where the Pacific plate subducts beneath North America, resulting in high seismicity. The data was obtained from WHTX, a station which was originally part of the EarthScope Transportable Array Network located at Lake Whitney, TX. Three broadband channels were selected to analyze: an east, north, and vertical channel. The frequency bandwith runs from 0.1 Hz to 25 Hz and the SNR from >1 to 10 Hz with 50 samples/second. The 7.1 magnitude event produces very high signal to noise ratio over most of the frequency range. This example makes use of the nominal USGS GSN location to demonstrate the method. Nominal arrival times are computed using the IASP91 model (Kennett and Engdahl, 1991).

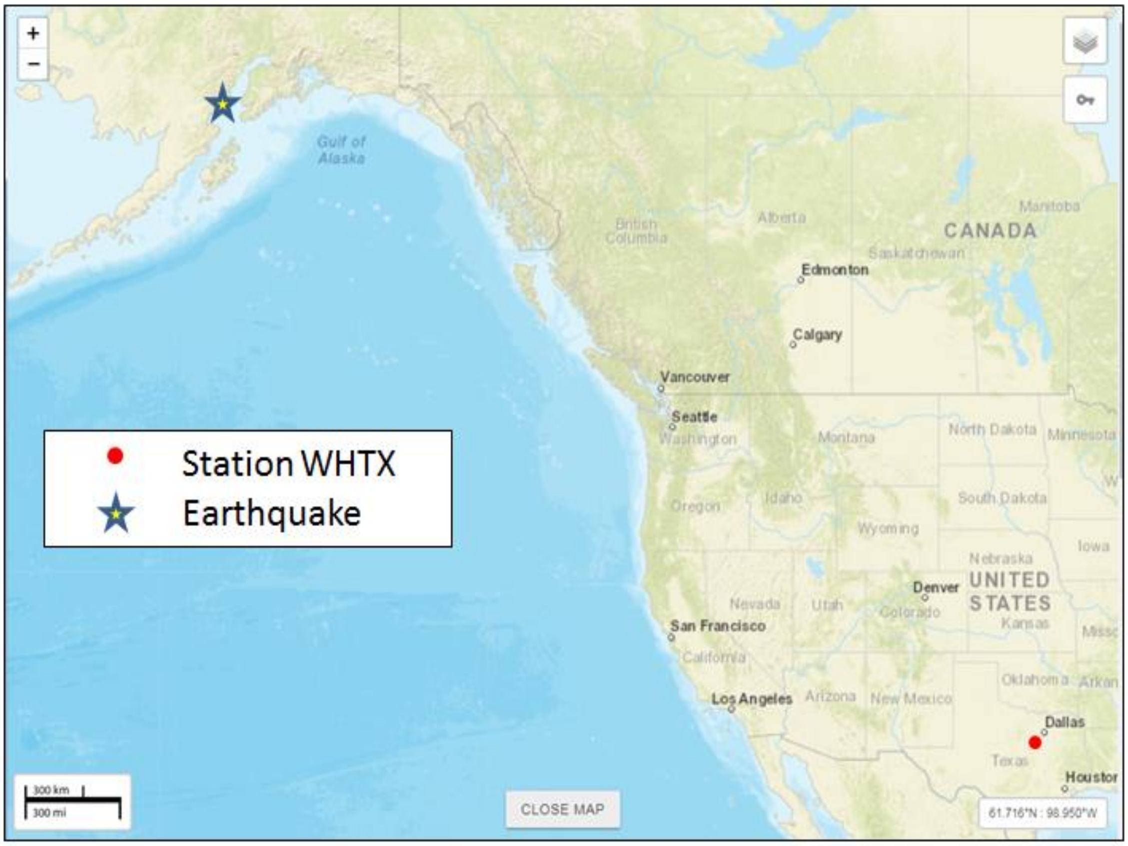

Figure 34. Earthquake and seismic station.

1. Obtain the seismograms and event/station data

1.1 Station Location- name, latitude, longitude, elevation, channels (E, N, Z)

1.2 Event- P-wave window, S-wave window, noise window

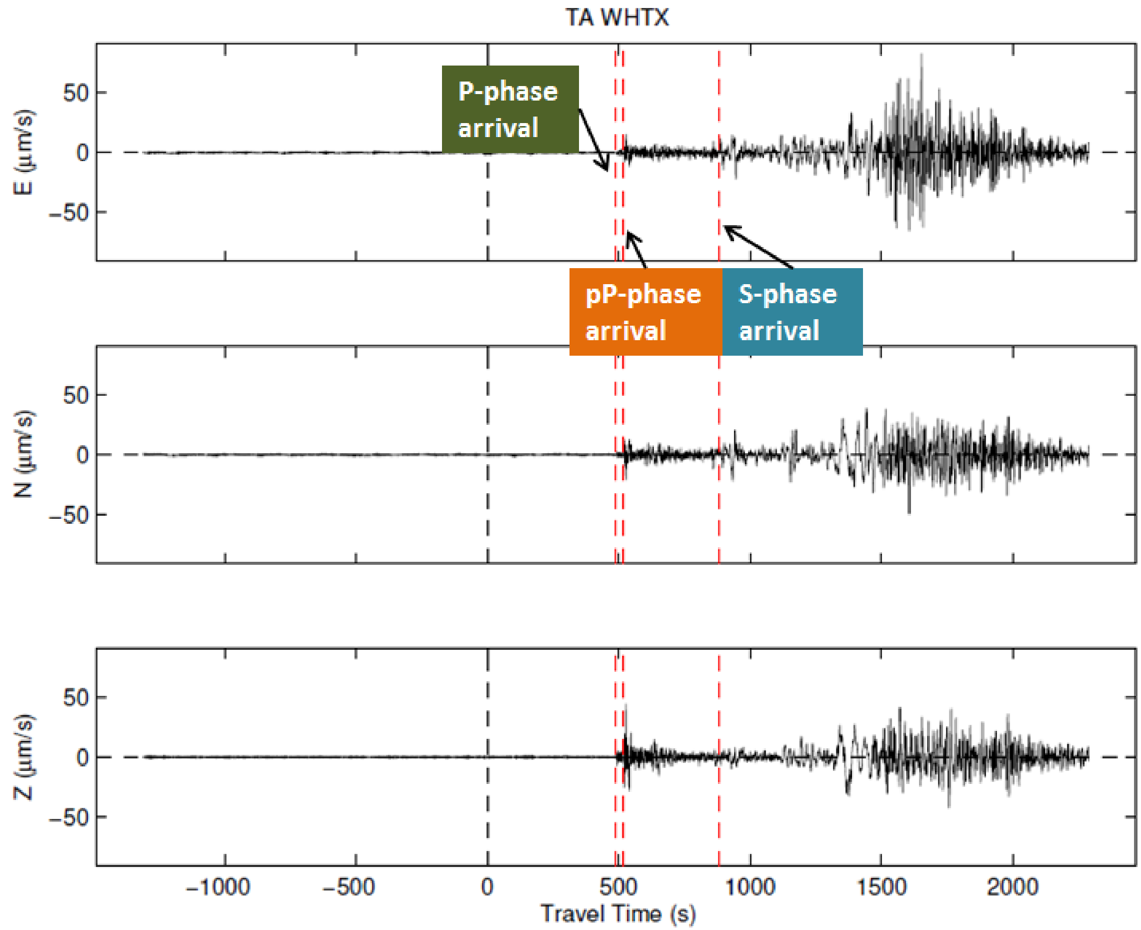

Figure 35. Seismograms for the three different channels: east, north, and vertical. The red lines are the nominal arrival times.

2. Frequency analysis

2.1 Local frequency

2.1.1 Signal detectors and band-pass filters follow from the local frequency

2.1.2 This allows adaptation to the signal frequency and generation of low frequency and high frequency detections bands

2.1.3 This enables some frequency discrimination in the detection process

2.2 Spectrum

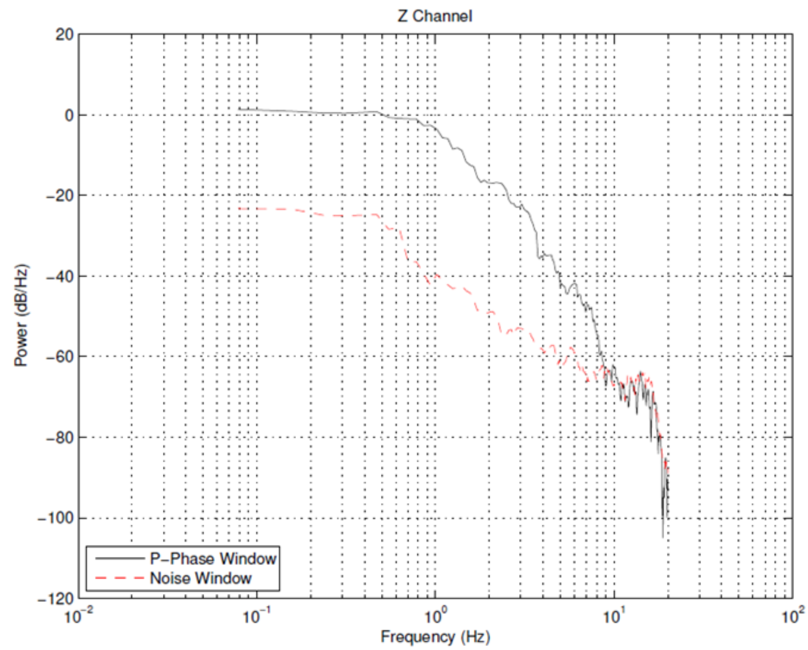

Figure 36. The power spectrum for the P-phase is shown, from which signal and noise characteristics are extracted. These can be used to optimize the bandpass filter and smoothing for the polarization processors. Here the maximum SNR is 41.7 dB at 0.86 Hz.

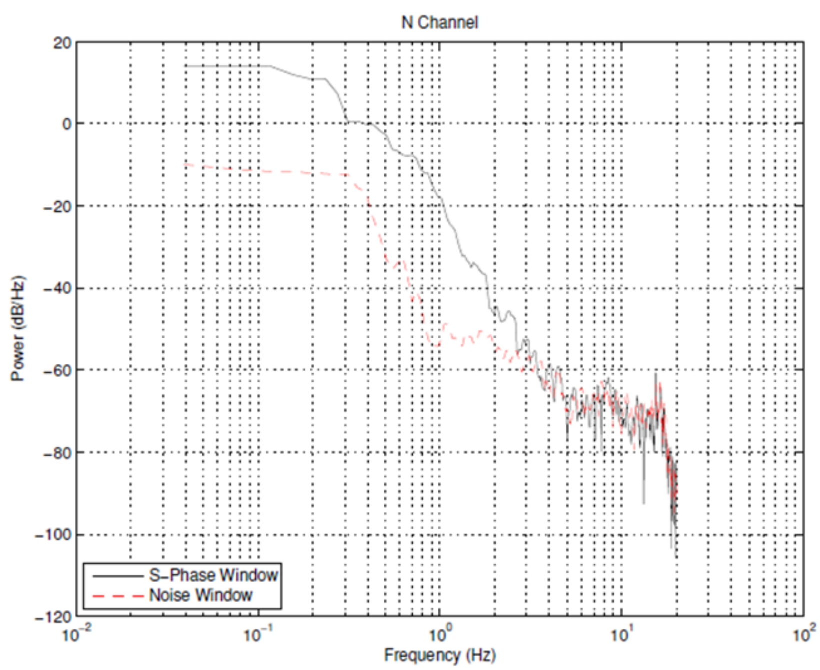

Figure 37. The power spectrum for the S-phase is shown, which has a lower SNR than the P-phase. Here the maximum SNR is 40.2 dB at 0.86 Hz.

3. Signal detectors

3.1 Frequency adaptive

3.1.1 Based on Tong and Kennett's work

3.2 STA/LTA trigger

3.2.1 A ratio of the short-term-average energy to the long-term-average energy

3.2.2 The STA yields information about seismic events, while the LTA yields information about the amplitude of the ambient seismic noise

3.2.3 When the ratio exceeds a predetermined threshold, an event is declared (Allen, 1978; Earle and Shearer, 1994; Trnkoczy, 2012)

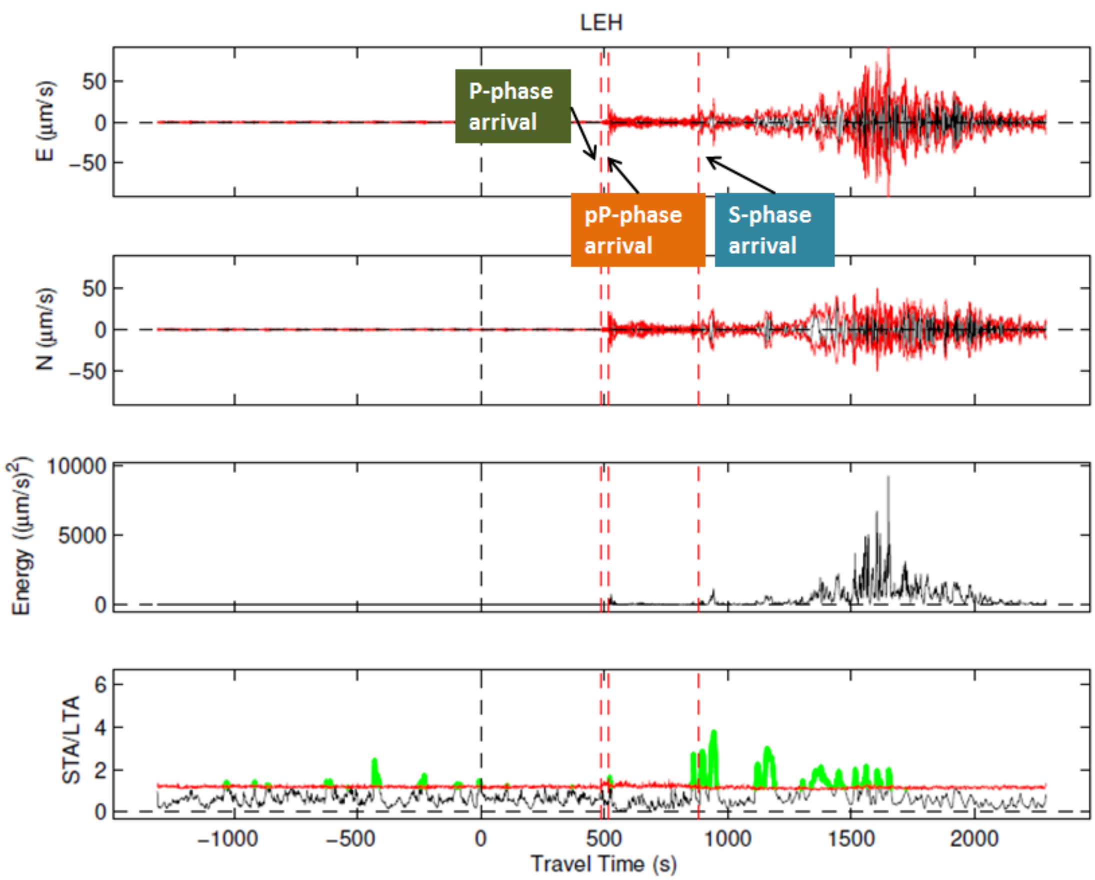

Figure 38. Triggers on the LEH (low-pass horizontal energy) detector. The green triggers reflect where the STA/LTA ratio threshold is exceeded. The red lines are the nominal arrival times. The signal envelope is red. The threshold is established by consideration of an F-test for a 5% confidence.

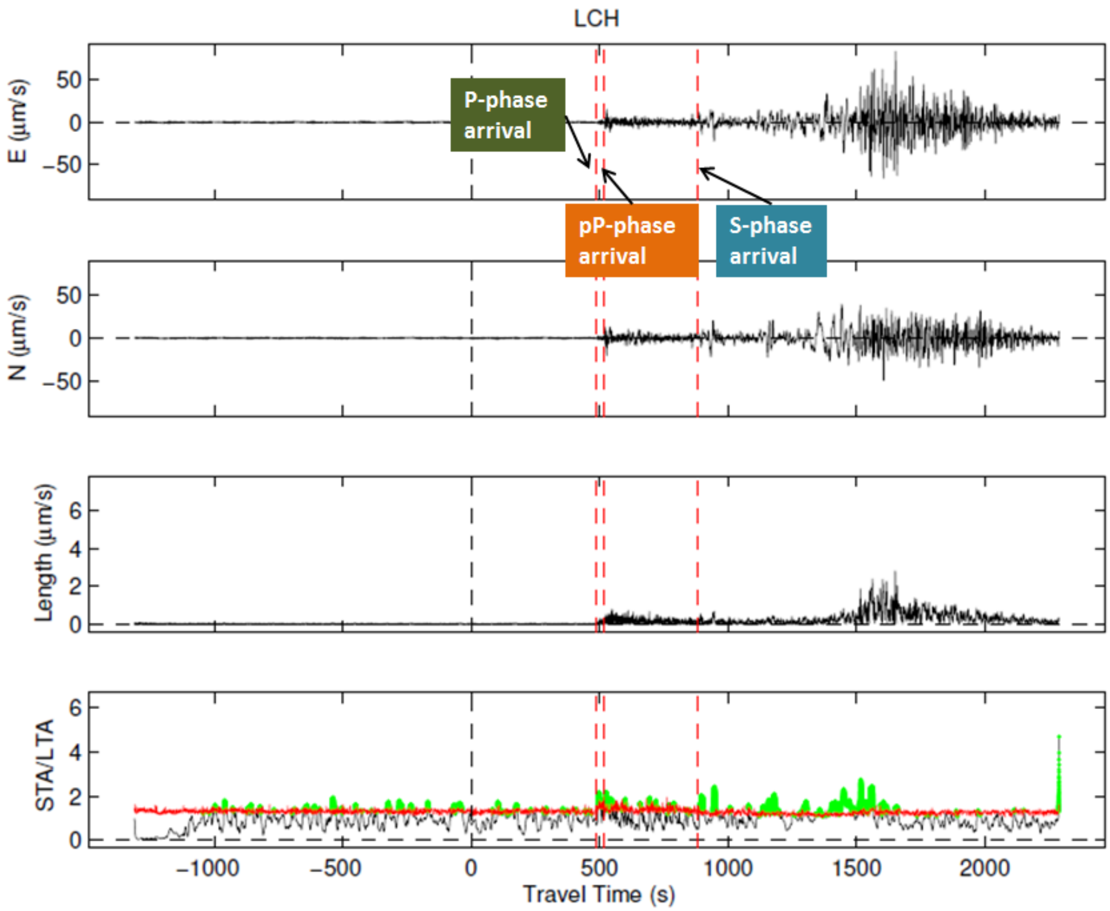

Figure 39. Triggers on the LCH (low-pass horizontal complexity) detector. The green triggers reflect where the STA/LTA ratio threshold is exceeded. The red lines are the nominal arrival times. The signal envelope is red. The threshold is established by consideration of an F-test for a 5% confidence.

The energy detector triggered on the pP- and S-phases, but not the P-phase. When looking at the seismogram in Figure 35, it is evident that pP-phase amplitude is much larger than the P-phase. There was much more energy present for the pP-phase, which overpowered the P-phase energy response, and hence, not did not trigger.

The complexity detector triggered on the P-, pP-, and S-phases. The P-phase trigger would be selected from the complexity, and not the energy. The complexity trigger and AR modeling are capturing the subtle P-phase signal.

4. Arrival picking for particular phases: P, S, pP, etc.

4.1 An autoregressive model is utilized to detect the arrival

4.1.1 This model is a prediction error filter that deconvolves the signal

4.1.2 It models the time series process and looks for changes

4.1.2 When the model ceases to be a good prediction, a detection is declared

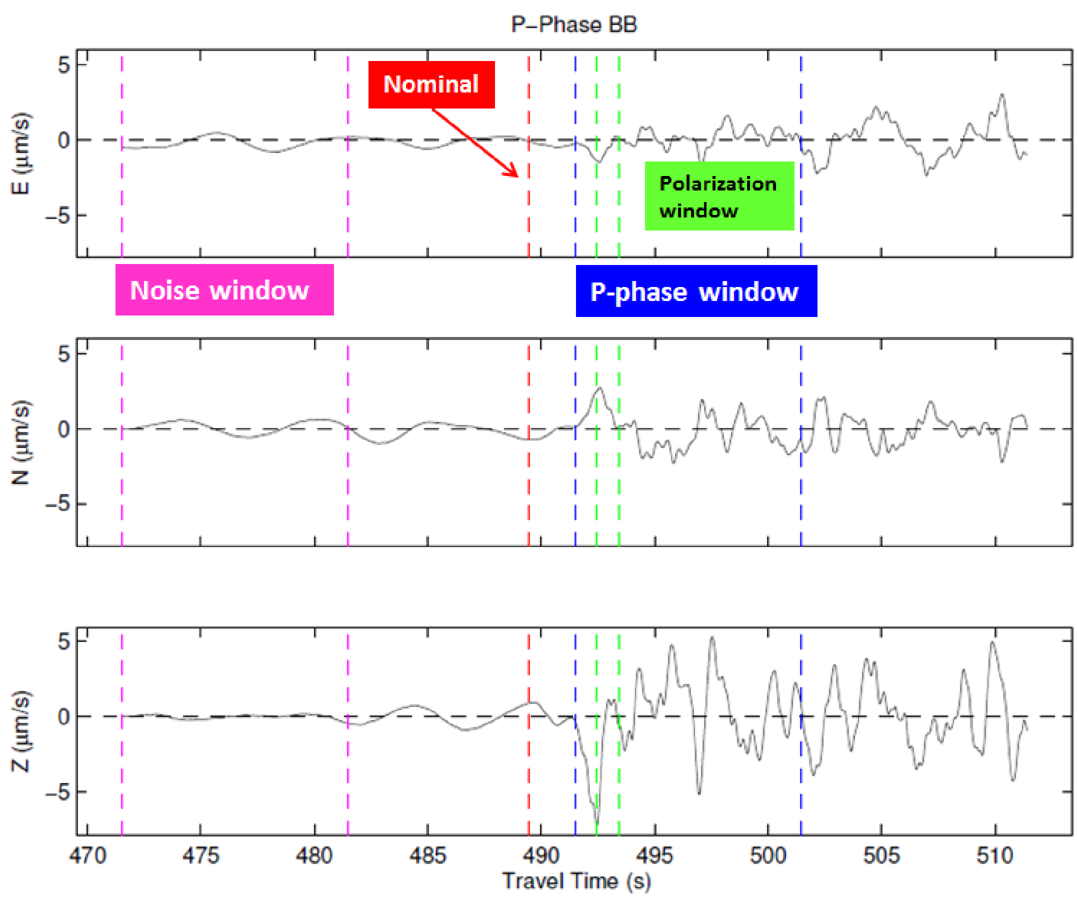

Figure 40. The seismogram is now zoomed in onto the P-phase. The red line is the nominal arrival time for the P-phase. For this processor, the P-phase window starts at the arrival pick.

Arrival of the P-wave is estimated from the minimum MDL statistic for forward and backward prediction error filters and AR models. The trigger is determined from multiple STA/LTA detectors. The polarization window is based on the pure state polarization statistic.

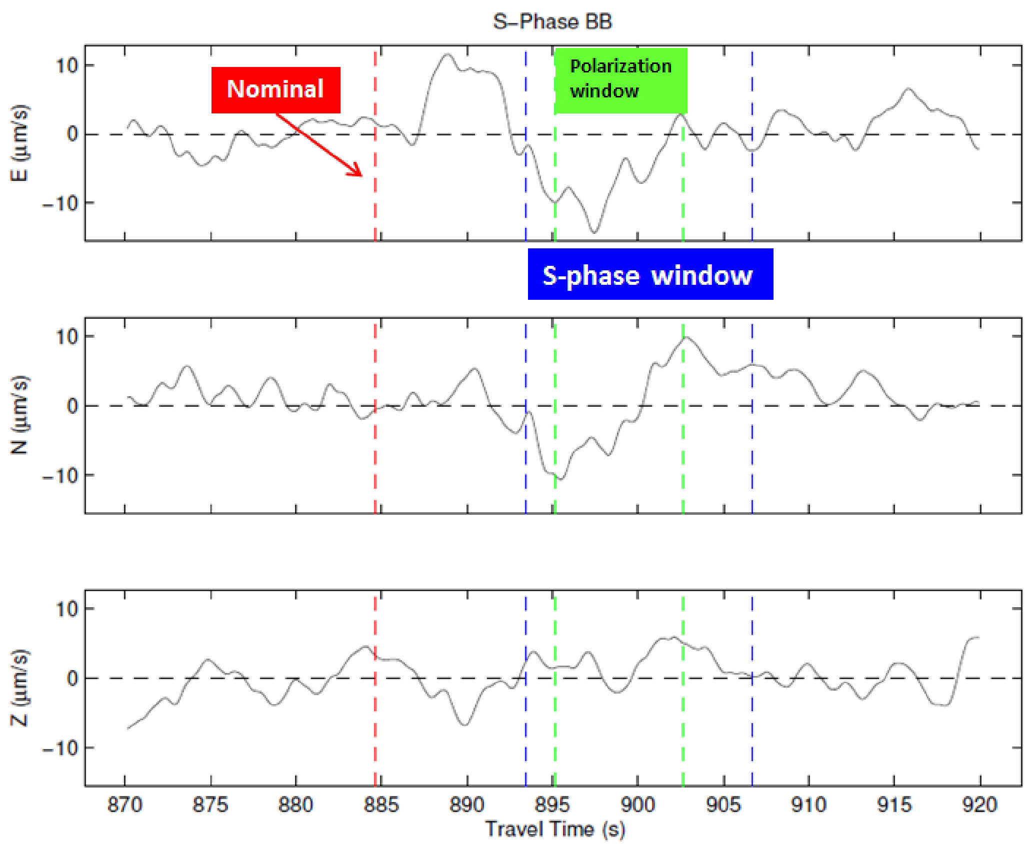

Figure 41. The seismogram is now zoomed in onto the S-phase. The red line is the nominal arrival time for the S-phase. For this processor, the S-phase window starts at the arrival time.

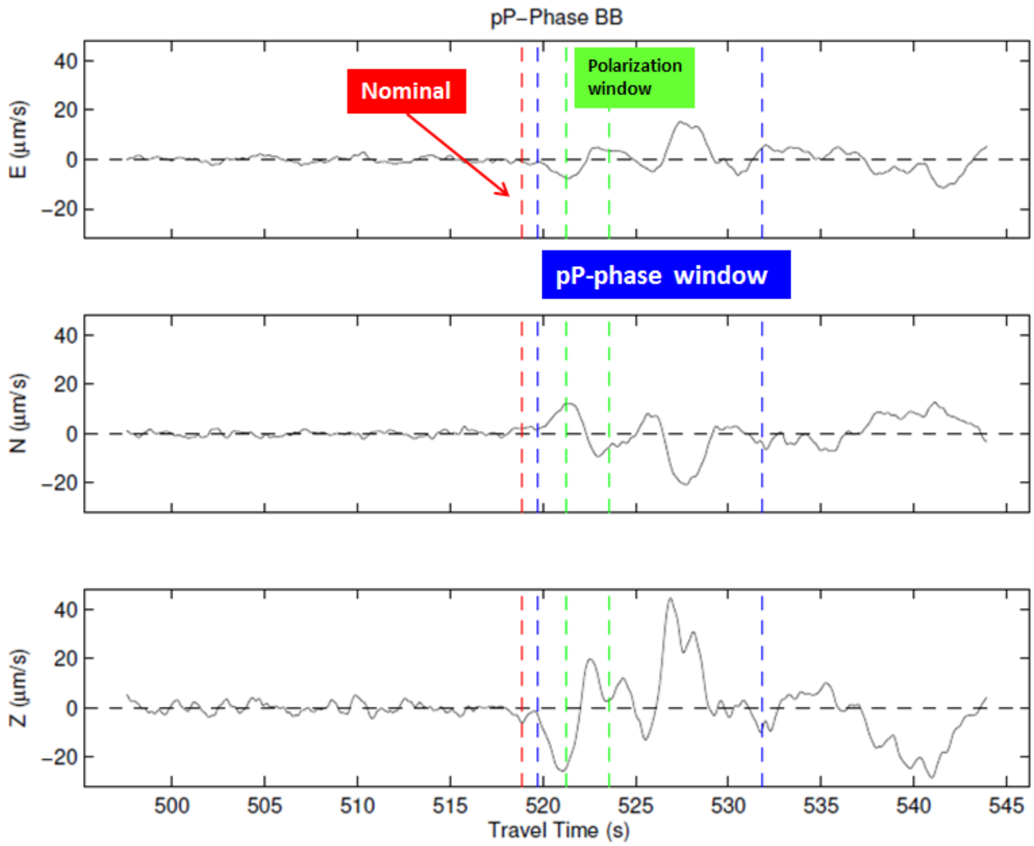

Figure 42. The seismogram is now zoomed in onto the pP-phase. The red line is the nominal arrival time for the pP-phase. For this processor, the pP-phase window starts at the pP-onset.

Figure 40 displays a noise window and a P-phase window. Figures 41 and 42 show only the S- or pP-phase window. Noise is always evaluated prior to the P-arrival. The noise window begins and ends prior the onset of the signal. The phase window begins and ends during the signal. The noise and phase window are designed to be the same length of time. The spectra are generated from the noise and phase windows.

5. Polarization analysis for particular phases

5.1 For the P-phase, the pure state method is employed: a single eigenvector is extracted for the P-wave

5.2 For the S-phase, the pure state method cannot be employed: all the eigenvectors must be computed

5.3 For the pP-phase, a single eigenvector is extracted (because it is similar to the P-wave)

6. Azimuth, inclination, and slowness

6.1 Azimuth

6.2 Rotate into (R, T, Z) using the azimuth

6.3 Incidence Angle

Figures 43 and 44 use rose diagrams to represent azimuthal and inclination data in a circular distribution. The rose diagram reflects a histogram in the polarization window.

6.4 Slowness from incidence angle (Snell's Law) and local velocity

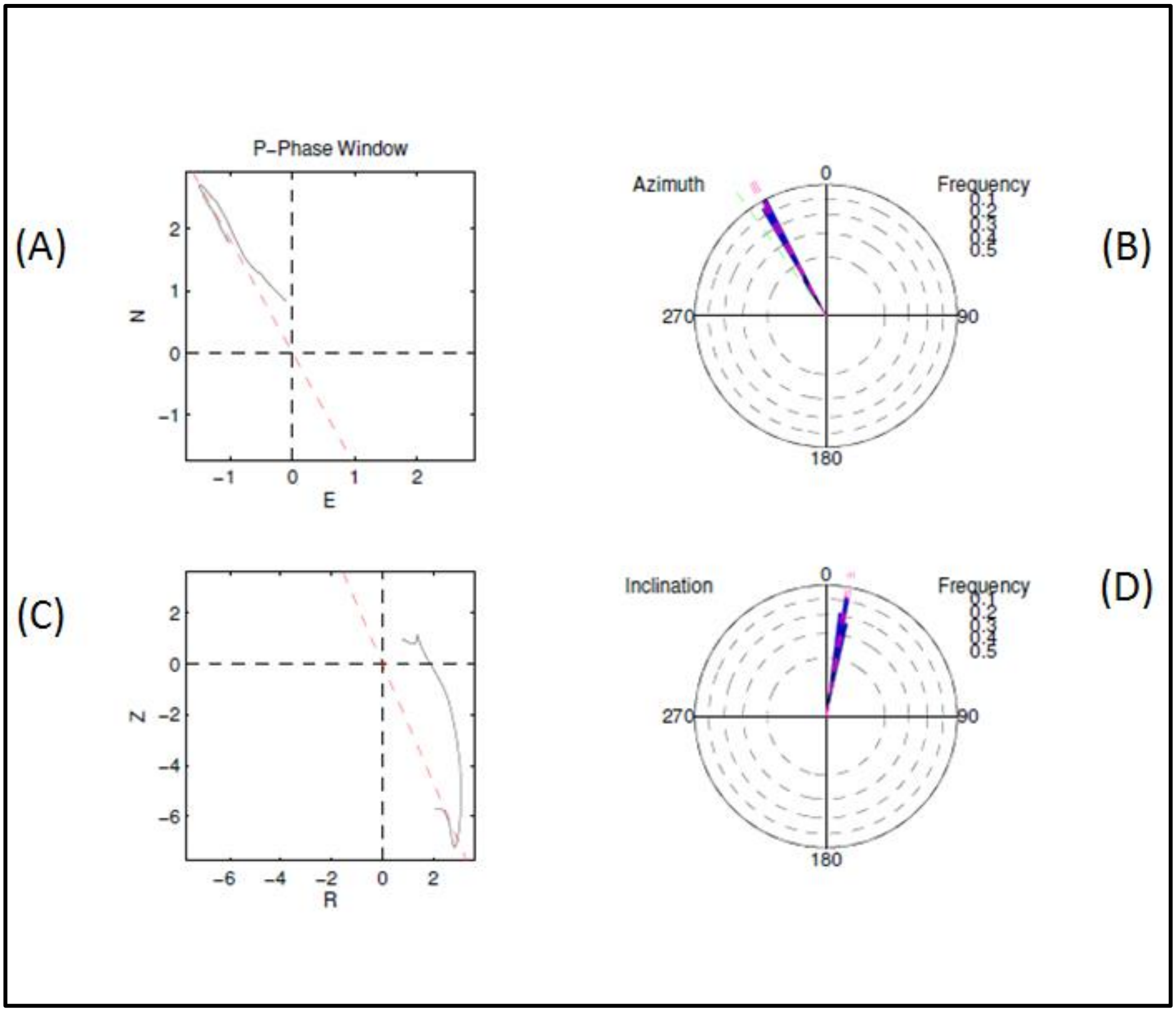

Figure 43. Azimuth and Incidence Angle for the P-phase. (A) A hodogram of the signal in the polarization window is shown. The azimuth is a time domain average of the major axis vector in the east and north directions. The computed azimuth is 331.1°, while the nominal azimuth is 324.12°. (B) A rose diagram of the azimuthal data. The tight distribution of the blue segments indicates there is relatively high certainty in this direction. The red line attempts to fit the azimuthal direction and the pink lines represent ± the standard deviation. The green line reflects the nominal azimuth of 324.12°. (C) The apparent incidence angle is a time domain average of the radial and vertical components of the major axis vector, which has been rotated into the radial direction. (D) A rose diagram of the inclination data. Notice that the blue segments are distributed over a wider region than the azimuthal direction in (B). This indicates there is more uncertainty in this direction. The red line attempts to fit the inclination direction and the pink lines represent ± the standard deviation.

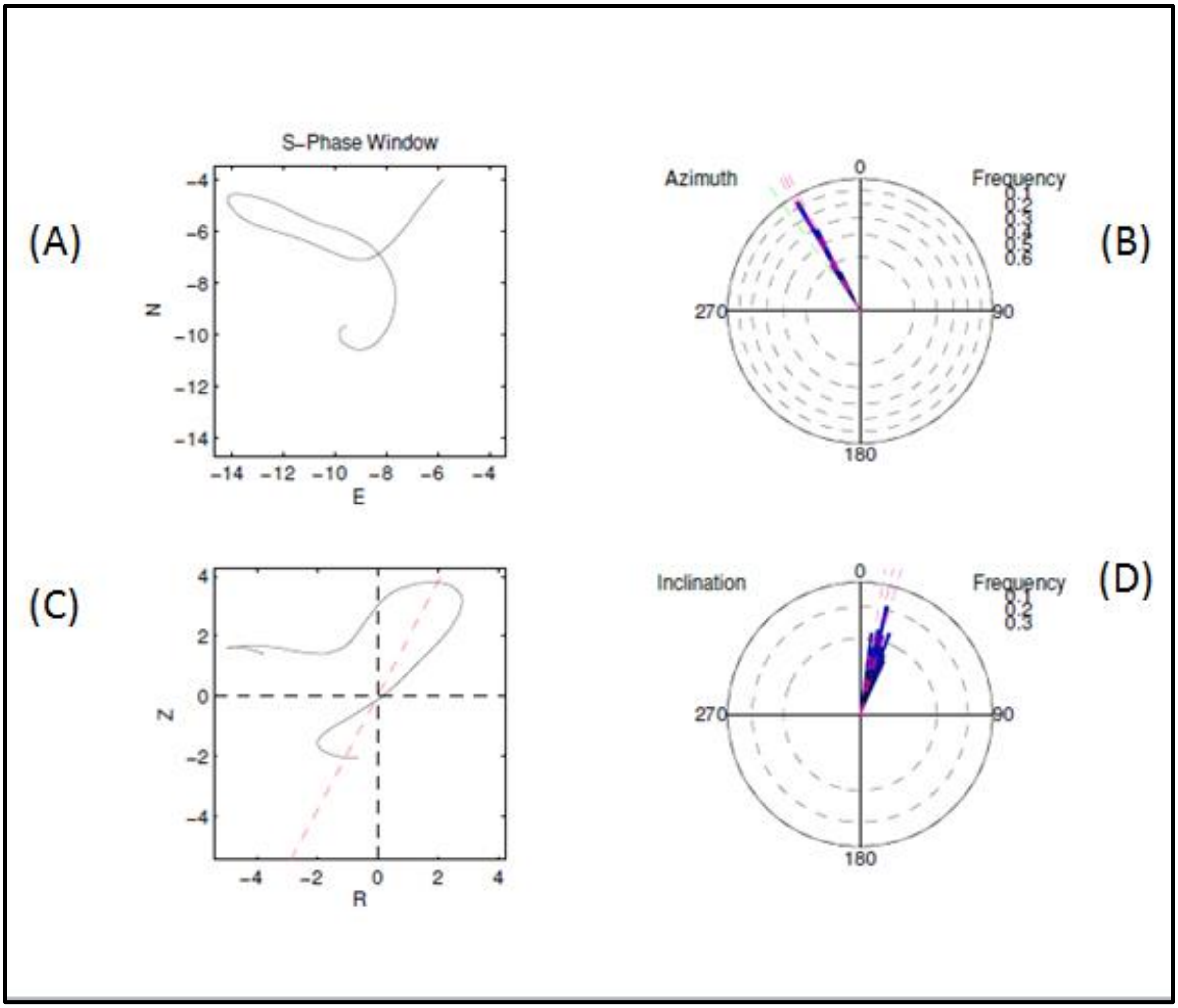

Figure 44. Azimuth and Incidence Angle for the S-phase. (A) A hodogram of the signal in the polarization window is shown. The azimuth is a time domain average of the major axis vector in the east and north directions. The computed azimuth is 330.1°, while the nominal azimuth is 324.12°. (B) A rose diagram of the azimuthal data. The tight distribution of the blue segments indicates there is relatively high certainty in this direction; however, the distribution is not as tight as the P-phase. The red line attempts to fit the azimuthal direction and the pink lines represent ± the standard deviation. The green line reflects the nominal azimuth of 324.12°. (C) The apparent incidence angle is a time domain average of the radial and vertical components of the major axis vector, which has been rotated into the radial direction. (D) A rose diagram of the inclination data. The much wider distribution of the blue segments when compared to the azimuthal direction in (B), and when compared to the P-phase, indicates there is more uncertainty in this direction. The red line attempts to fit the inclination direction and the pink lines represent ± the standard deviation.

7. Location from azimuth and either slowness or S-P times

7.1 Use the latitude of the station, longitude of the station, azimuth, epicentral distance, and traveltime to obtain the latitude of the event, longitude of the event, and origin time

Figure 45 shows the estimated location. This location error is mostly due azimuth error, not distance error.

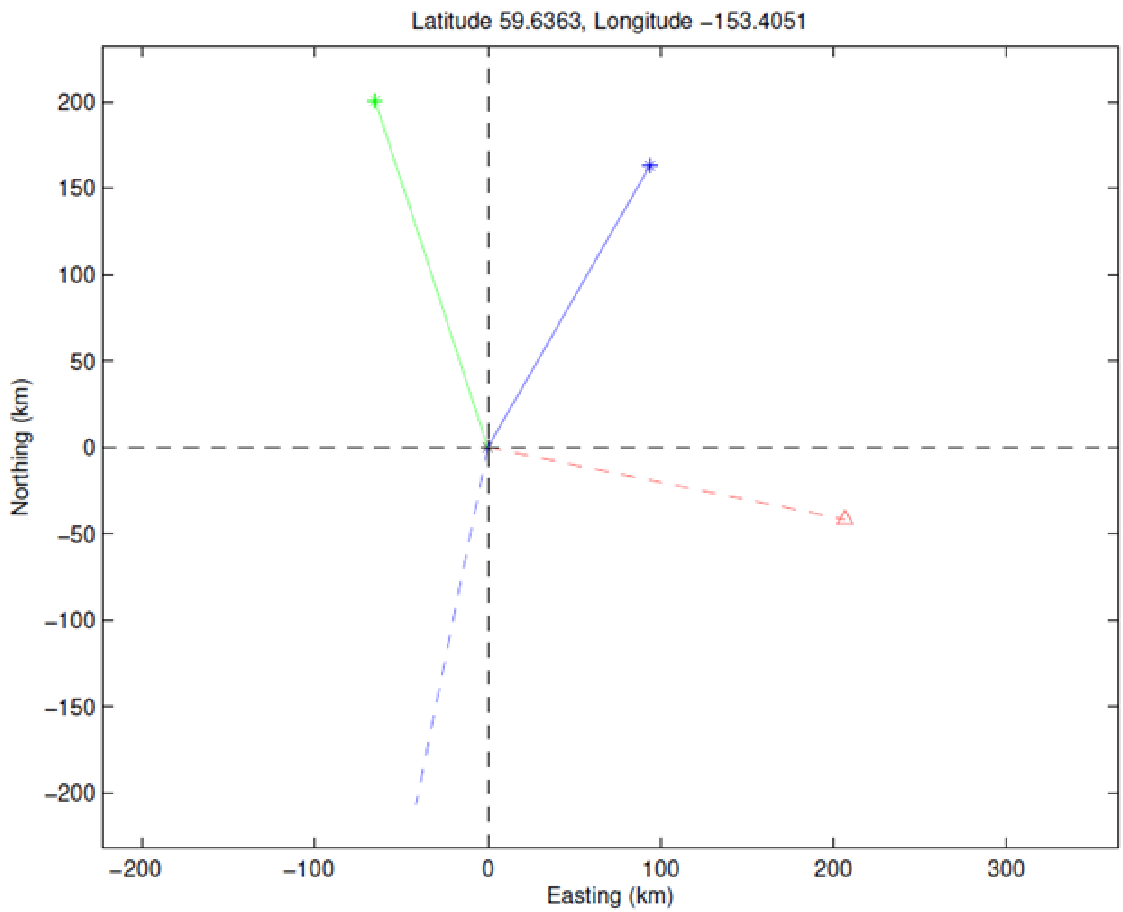

Figure 45. The blue line is the location computed by using the azimuth and S-P time. The green line is the location computed by using the azimuth, S-P and pP-P time. The blue dotted line reflects the transverse direction. The red dotted line reflects the radial direction, which points in the direction of the station. The origin reflects the nominal location.

CHAPTER 5

VERIFICATION OF RESULTS

To verify the effectiveness of this processor, the USGS GSN locations were taken as the nominal locations. For several selected stations, a large number of events with varied azimuths, distances, depths, etc. were run through this processor and compared to the USGS locations. In addition, the standard errors of latitude, longitude, and origin time are known; these are parameters that can also be used to verify results.

CHAPTER 6

ANALYSIS OF RESULTS

Locations from all three stations were analyzed to examine the impact of local geology on single-station event location accuracy. Seismicity maps were plotted for the three stations and compared to the nominal USGS ANSS seismicity map. The goal was to examine the similarity of the maps and see if structures related to plate tectonics could be resolved. It was also contemplated: How well do these maps compare to Gutenberg and Richter's 1954 seismicity map of the Earth?

6.1 Seismicity Maps

A map was generated from the USGS ANSS data that was comparable to Gutenberg and Richter's 1954 map. These data reflect the state of knowledge prior to the installation of the WWSSN (see Chapter 1) and the modern development of plate tectonic theory. Figure 46 portrays Gutenberg and Richter's (1954) seismicity map, which displays earthquakes with magnitudes ≥7 from 1904 to 1954 (Gutenberg and Richter, 1954). Figure 47 portrays the USGS ANSS seismicity map that mimics the Gutenberg and Richter (1954) map. This map also includes earthquakes with magnitudes ≥7 from 1904 to 1954. The green lines are the plate boundaries. The triangles are the stations.

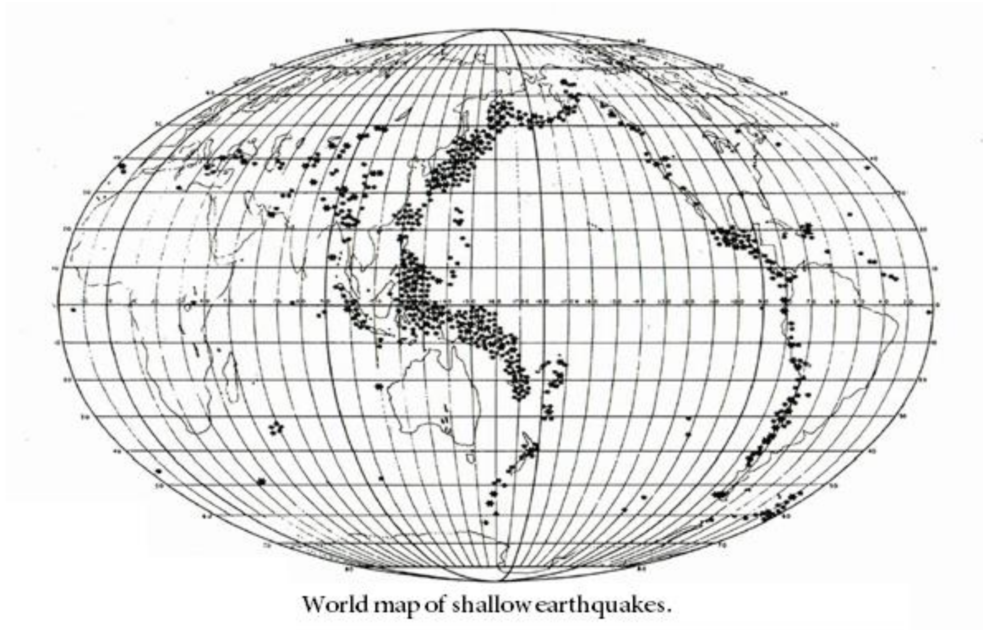

Figure 46. The Gutenberg and Richter (1954) seismicity map for the 1904-1954 period (Gutenberg and Richter, 1954).

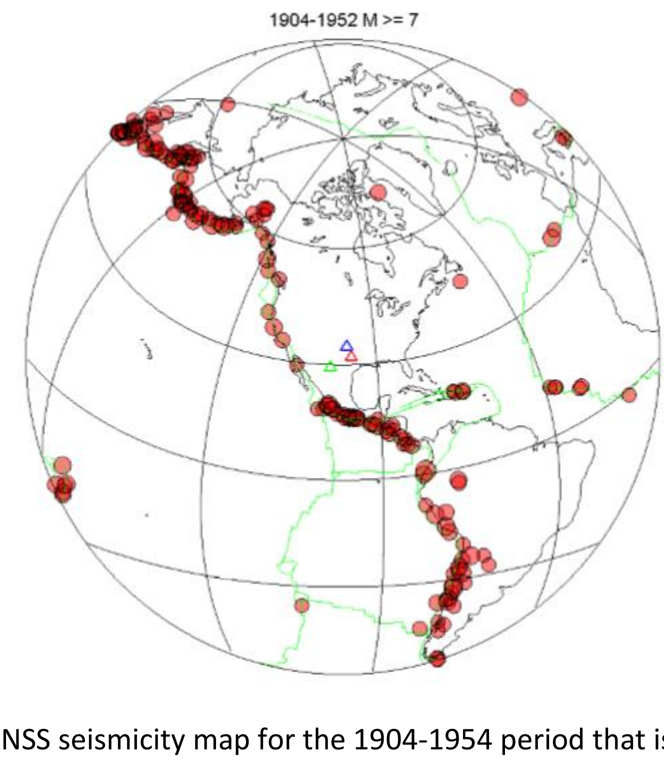

Figure 47. The USGS ANSS seismicity map for the 1904-1954 period that is centered on Texas/Oklahoma.

Two subsets of data were examined: one that included **All** of the 274 events, and another subset that included the 103 events **Common** to all three stations. Table 5 compares these two subsets.

Table 5. Statistics for All and Common events.

Station	Total # of events	Deep	Shallow	Incom-plete	No P	No S	No pP	Bad	P-wave bad arrival	S-wave bad arrival	Fair or bad polari-zations
All events with magnitudes ≥6 (count).											
TX32	213	39	172	59	2	24	179	1	6	23	14
WHTX	185	31	136	87	18	18	137	1	6	22	12
WMOK	198	31	138	74	29	35	147	1	9	17	10
Total #	**596**	**101**	**446**	**220**	**49**	**77**	**463**	**3**	**21**	**62**	**36**
All events with magnitudes ≥6 (percentages).											
TX32	78	18	81	22	1	11	84	1	3	11	7
WHTX	68	17	74	32	10	10	74	1	3	12	6
WMOK	73	16	70	27	15	18	74	1	5	9	5
Total #	**73**	**17**	**75**	**27**	**8**	**13**	**78**	**1**	**4**	**10**	**6**
Common events with magnitudes ≥6 (count).											
TX32	103	18	84	0	1	14	89	1	1	10	8
WHTX	103	18	76	0	9	9	77	1	3	12	7
WMOK	103	17	78	0	8	12	75	1	4	10	6
Total #	**309**	**53**	**238**	**0**	**18**	**35**	**241**	**3**	**8**	**32**	**21**
Common events with magnitudes ≥6 (percentages).											
TX32	100	17	82	0	1	14	86	1	1	10	8
WHTX	100	17	74	0	9	9	75	1	3	12	7
WMOK	100	17	76	0	8	12	73	1	4	10	6
Total #	**100**	**17**	**77**	**0**	**6**	**11**	**78**	**1**	**3**	**10**	**7**

It was found that the two subsets were very similar. Because of this, a choice was made to further analyze only the common events. For the rest of this discussion, only the 103 common events will be analyzed.

Seismicity maps for the three stations are shown in Figure 48. These were compared to the nominal USGS map, which was also reduced to only portray the 103 common events.

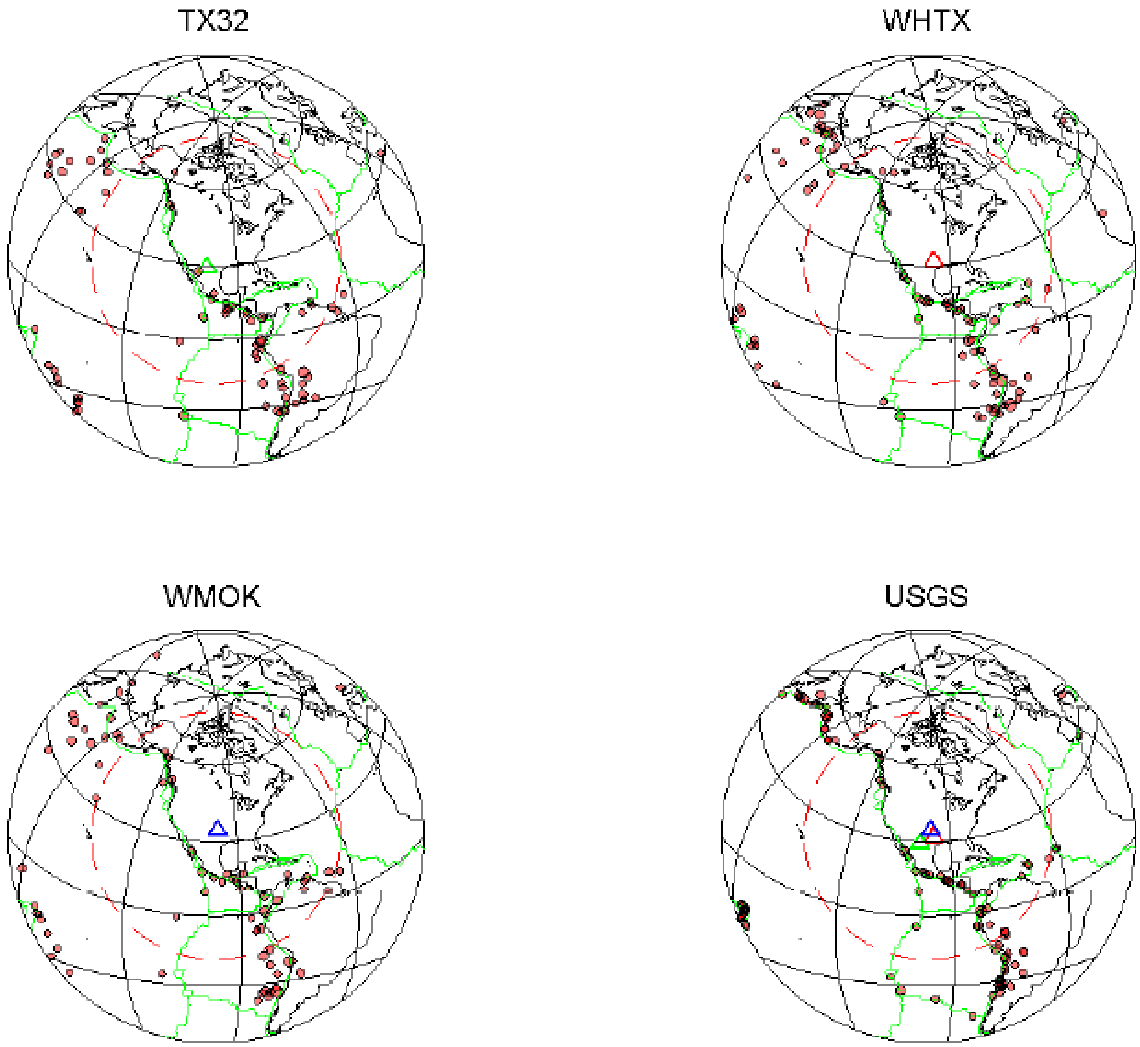

Figure 48. Seismicity maps for TX32, WHTX, and WMOK, along with the USGS locations. The dashed red circle reflects events with distances ≥50°. The green lines are the tectonic plate boundaries.

The nominal map clearly shows the tectonic plates and subduction zones. On the station maps, plate boundaries can be inferred but there is a substantial amount of scatter.

6.2 Mislocation Maps

Mislocation maps are shown for TX32, WHTX, and WMOK in Figure 49. The black dots are the nominal locations. The distance was obtained from the S-P time difference and the azimuth from the P-phase polarization.

TX32 has large counterclockwise and clockwise shifts, indicating azimuthal bias. WHTX has low bias. Similar to TX32, WMOK has counterclockwise and clockwise shifts, indicating azimuthal bias. All of the stations have large scatter and outliers. Robust statistical measures were utilized.

For the rest of the analysis, the two locations methods, **Azimuth and S-P time** and **Azimuth, S-P time, and pP-P time**, will be denoted by 'et' and 'ett', respectively.

Figure 50 shows the azimuth error distribution for the P-phase for TX32, WHTX, and WMOK. TX32 has the most asymmetrical distribution which indicates bias. Misalignment of the seismometer or errors in the transfer functions for the horizontal and vertical channels could contribute to the bias. TX32 has the most scattered energy. This unpolarized scattered energy compromises the polarization estimate, contributing to the variance. This scattered energy can also greatly affect the V_p estimates. Most of the bias is due to lithosphere structure (see Chapter 1). WHTX has the smallest bias. WMOK has less bias than TX32. 3D local structures at the station contribute to time shift errors, coda noise, and refraction which bends raypaths; these produce azimuth errors.

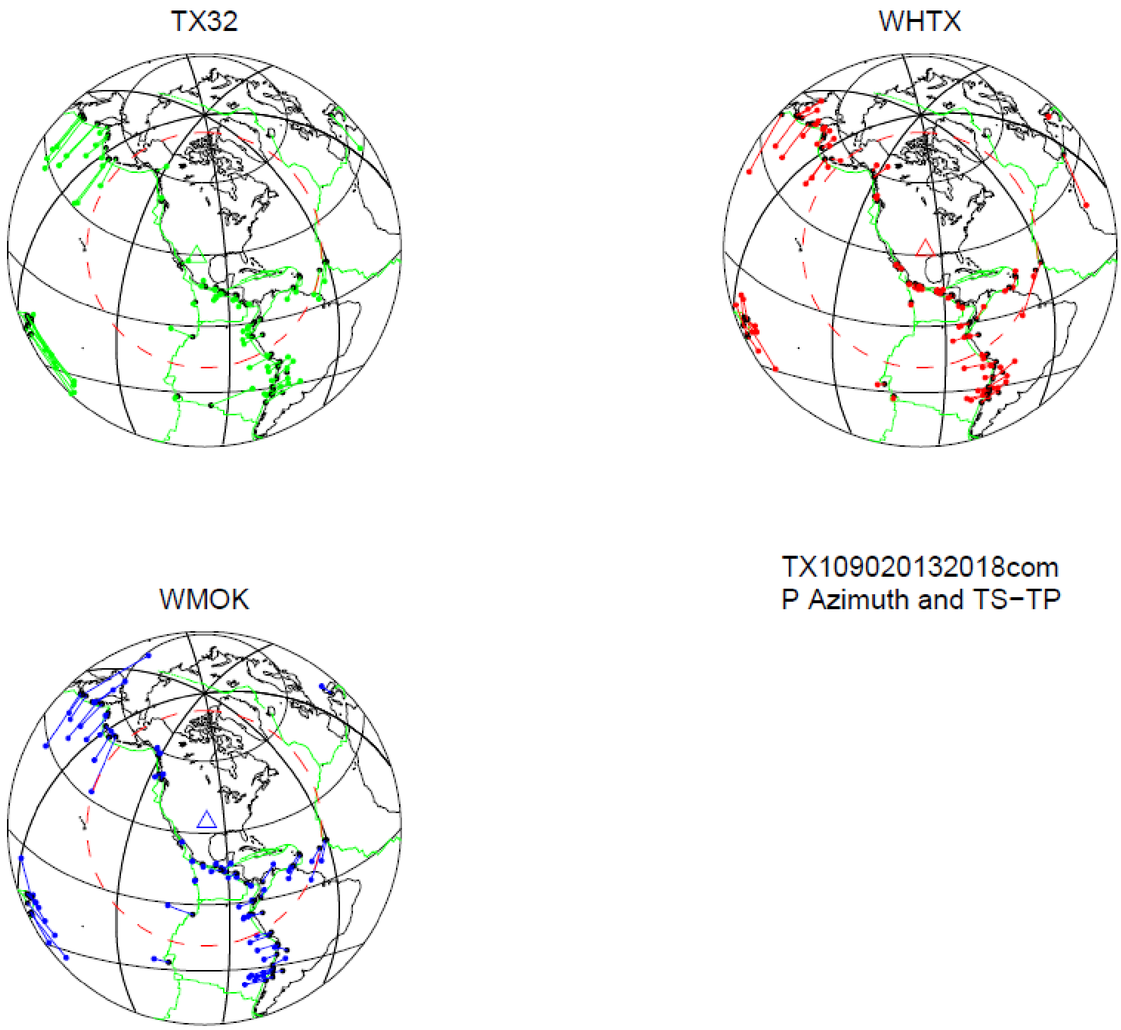

Figure 49. Location estimates using the P-wave azimuth and S-P time for TX32, WHTX, and WMOK. TX32 produces quite large location errors. WHTX produces smaller location errors. WMOK produces intermediate location errors.

Bias in the azimuth is caused by local refraction effects in a 3D velocity structure near the station. TX32 has the lowest noise but larger azimuthal refraction and coda, and detects more events but doesn't locate adequately. WHTX has the highest noise levels but locates events better.

Figure 50 also shows the distance error distribution for the P-phase. Azimuth error is independent of distance. Distance errors are caused by traveltime errors and reflect deficiencies in the global velocity model as well as local velocity effects near the station and source. For all stations, there is some bias which could be a global effect. TX32 has the least variance which is due to the higher SNRs at TX32.

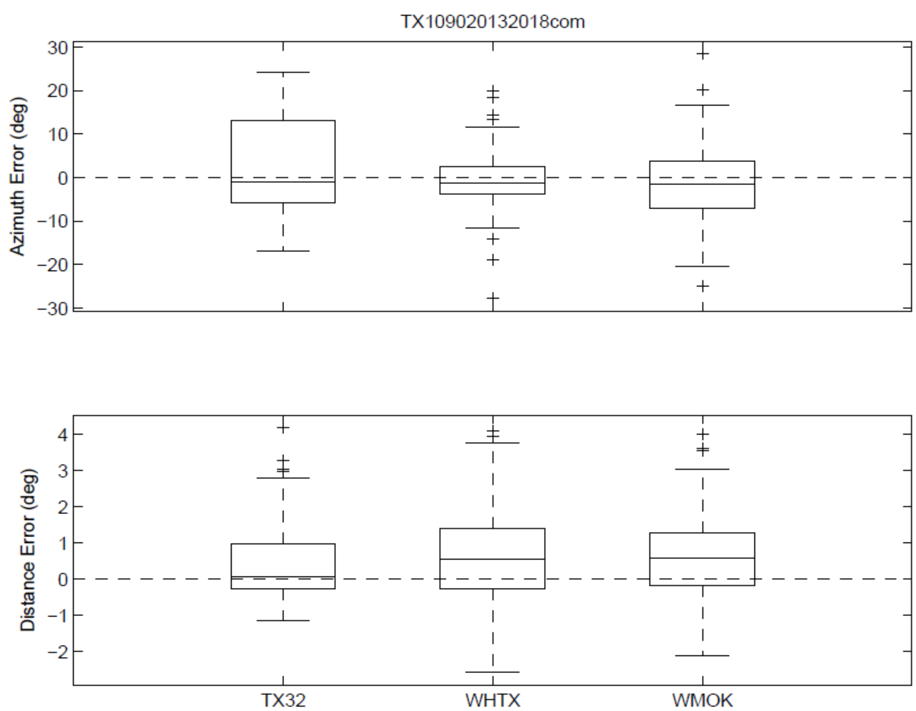

Figure 50. Boxplots for the azimuth and distance errors for TX32, WHTX, and WMOK.

Table 6 is an analysis of S-P time and azimuthal outliers for each station. Each station has different total number of events that were actually located out of the 103 common events. S-P times are associated with distance errors. TX32 and WMOK have similar percentages for S-P time outliers, but WHTX is much higher. As seen in Figure 51, the total angular location error $\delta\Lambda$ = $(\theta_e, \psi_e) - (\widehat{\theta_e}, \widehat{\psi_e})$ has two components, an azimuthal component δA = $A - \hat{A}$ and a distance component $\delta\Delta = \Delta - \hat{\Delta}$. The prefix '$\delta$' is the difference between the nominal and estimated values. The $\delta\Lambda$ variable is dominated by azimuth error. Distance errors tend to be smaller and are associated with traveltime errors.

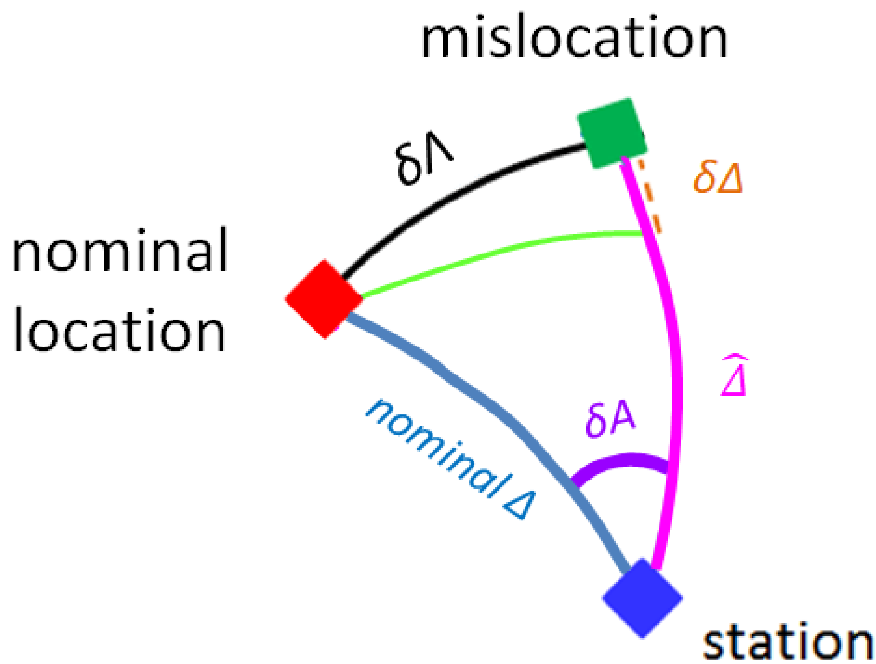

Figure 51. The components of the total angular location error, $\delta\Lambda$, variable. The spherical trigonometry in this figure defines $\delta\Lambda = (\theta_e, \psi_e) - (\widehat{\theta_e}, \widehat{\psi_e})$ (Herrmann, 2007).

Azimuth errors are most associated with refraction effects. Out of the located events, TX32 has a lower percentage of outliers. Azimuthal outliers stem from P-wave azimuth error, while S-P time outliers are dominated by S-arrival time error. WHTX and WMOK have higher background noise and a higher percentage of azimuthal outliers. The outliers are rejected in the mislocation maps.

Table 6. Percentages of outliers for the 'et' method.

Stations	S-P time outliers	Azimuthal outliers
TX32	$^{8}/_{89}$ → 7.77 %	$^{3}/_{89}$ → 2.91%
WHTX	$^{14}/_{94}$ → 13.59 %	$^{7}/_{94}$ → 6.80 %
WMOK	$^{9}/_{91}$ → 8.74 %	$^{9}/_{91}$ → 8.74%

Table 7 contains measures of the median (md) and robust standard deviation (rsd) for the P- and S- traveltimes (δTP, δTS), distance ($\delta\Delta$), and azimuth (δA). The 'et' method has no depth estimates, so depth is constrained to 11 km. 'Nloc' is the number of events that were actually located. TX32 has the lowest traveltime and distance scatter (standard deviation), while WHTX has the highest. Here it is evident that TX32 has the highest azimuthal scatter, while WHTX is the lowest.

Table 7. Statistics for Common events with magnitudes ≥6 for the 'et' method.

Station	**#**	**Nloc**	**md**	**rsd**	**md**	**rsd**	**md**	**rsd**	**md**	**rsd**
			δTP		***δTS***		***δΔ***		***δA***	
TX32	103	89	-2.15	4.05	-3.73	6.59	0.10	1.01	-0.03	13.7
WHTX	103	94	0.04	6.10	1.48	10.2	0.69	1.42	-1.34	5.25
WMOK	103	91	-0.04	4.85	1.38	9.20	0.72	1.25	-1.56	8.83
Total #	**309**	**274**	**-0.70**	**5.09**	**-0.25**	**8.84**	**0.51**	**1.24**	**-0.99**	**9.83**

Averages

Azimuth Error Models

Similar counterclockwise and clockwise shifts were observed in the azimuth error models for TX32 and WMOK as portrayed in Figure 52. TX32 shows a counterclockwise and clockwise pattern. WHTX has no pattern. WMOK also shows a counterclockwise and clockwise pattern; however, not as large as TX32.

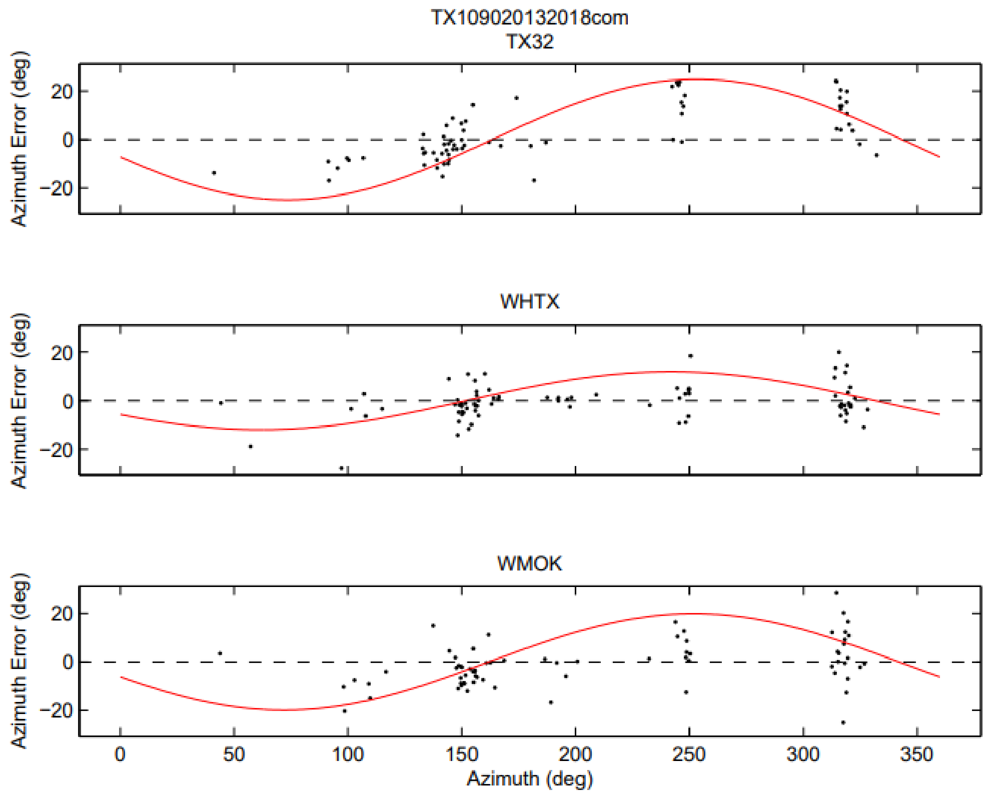

Figure 52. The nominal azimuths plotted against the estimated azimuth errors for TX32, WHTX, and WMOK. The data points are in clusters due to geographic areas where earthquakes do occur, such as subduction zones, and do not occur, such as cratonic areas. This plot excludes outliers. The red curves are a robust fit of a sinusoid to the azimuth error.

An F-test was used to investigate the significance of each model. The model was computed by fitting a sinusoidal curve to the azimuthal error using a robust method.

The F-test found the models at TX32 and WMOK to be significant. It was speculated that WMOK would need an azimuth correction because the site is located near a large thrust fault. The F-test found the model at WHTX to be insignificant. Due to the large azimuthal variance, corrections based on these models were not applied. Table 8 shows the F-test values computed to test the significance of the azimuthal models. The significant models are red.

Table 8. F-test with a 5% tail.

Station	Data Subset	F-critical value	F-statistic	Amplitude	Phase
TX32	Common	1.39	1.49	24.87	-106.64°
WHTX	Common	1.41	0.77	19.87	-108.06°
WMOK	Common	1.41	0.33	11.97	-118.26°
TX32	All	1.26	1.35	25.53	-108.24°
WHTX	All	1.29	1.76	12.08	-84.36°
WMOK	All	1.29	0.28	21.60	-117.77°

6.3 P- and S-Phase SNR

TX32 has lower background noise; the SNR is never <10 dB. TX32 has the highest SNR for the P- and S-phase when compared to the other stations. WHTX has higher background noise and the lowest SNRs.This is portrayed in Figure 53.

For all of the stations, the P-phase SNR is lower on the horizontal channels than the vertical channel, while the S-phase SNR is lower on the vertical channel than the horizontal channels. The horizontal channels for the P-phase, PE and PN, have high SNRs which is important for computing the azimuth. The vertical component PZ has the highest SNR for all stations.

The SNR for the S-phase at TX32 is low compared to the other stations. For TX32, the P-phase is higher than the S-phase on all components due to more scattering/coda. For WHTX, the S-phase is higher than the P-phase on some components.

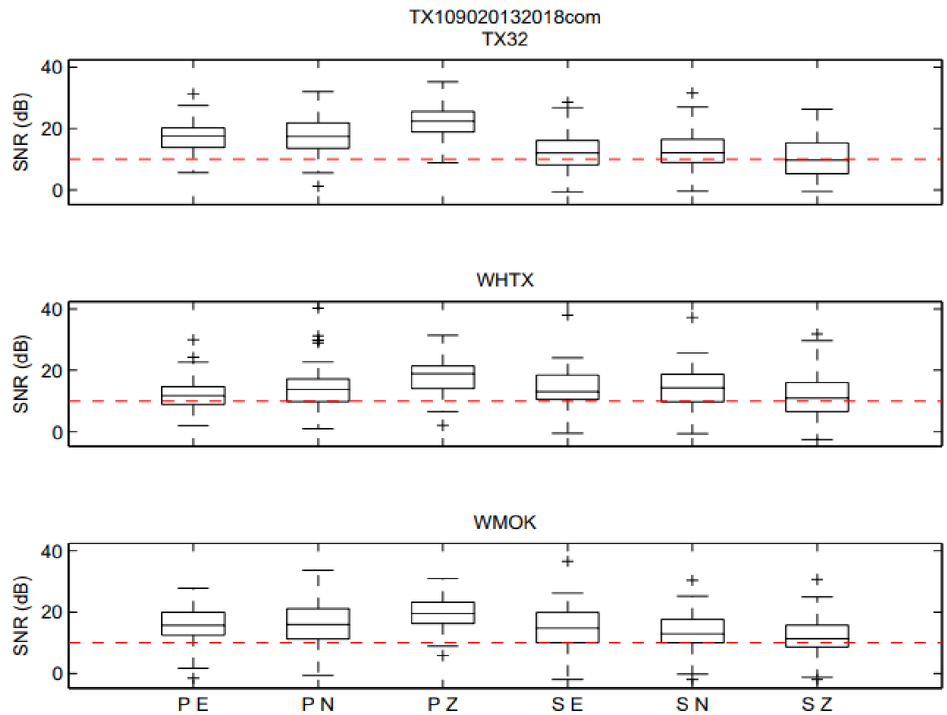

Figure 53. The mean SNR distribution for the E, N, and Z channels corresponding to the P, pP, and S-phases for TX32, WHTX, and WMOK.

6.4 Near Receiver Scattering/Multi-Pathing

TX32 has more coda generated near the station, while WHTX and WMOK have less coda. This is evident when comparing seismograms among the three stations. Eight events with magnitudes ≥7 were analyzed to assess the coda at the three stations. The (R, T, Z) components of the P-wave were examined for raw and pure state filtered (PSF) seismograms. Coda was obtained by subtracting the pure state filtered seismogram from the raw seismogram. Figure 54 shows the raw, pure state filtered, and coda seismograms for one of these events, as well as the coda at the three stations. This event is a magnitude 7.7 earthquake near Iquique, Chile from April

2014. For this event, the initial P-phase is small while the pP-phase is large. WHTX has the strongest arrival, and hence, the strongest coda for this particular event.

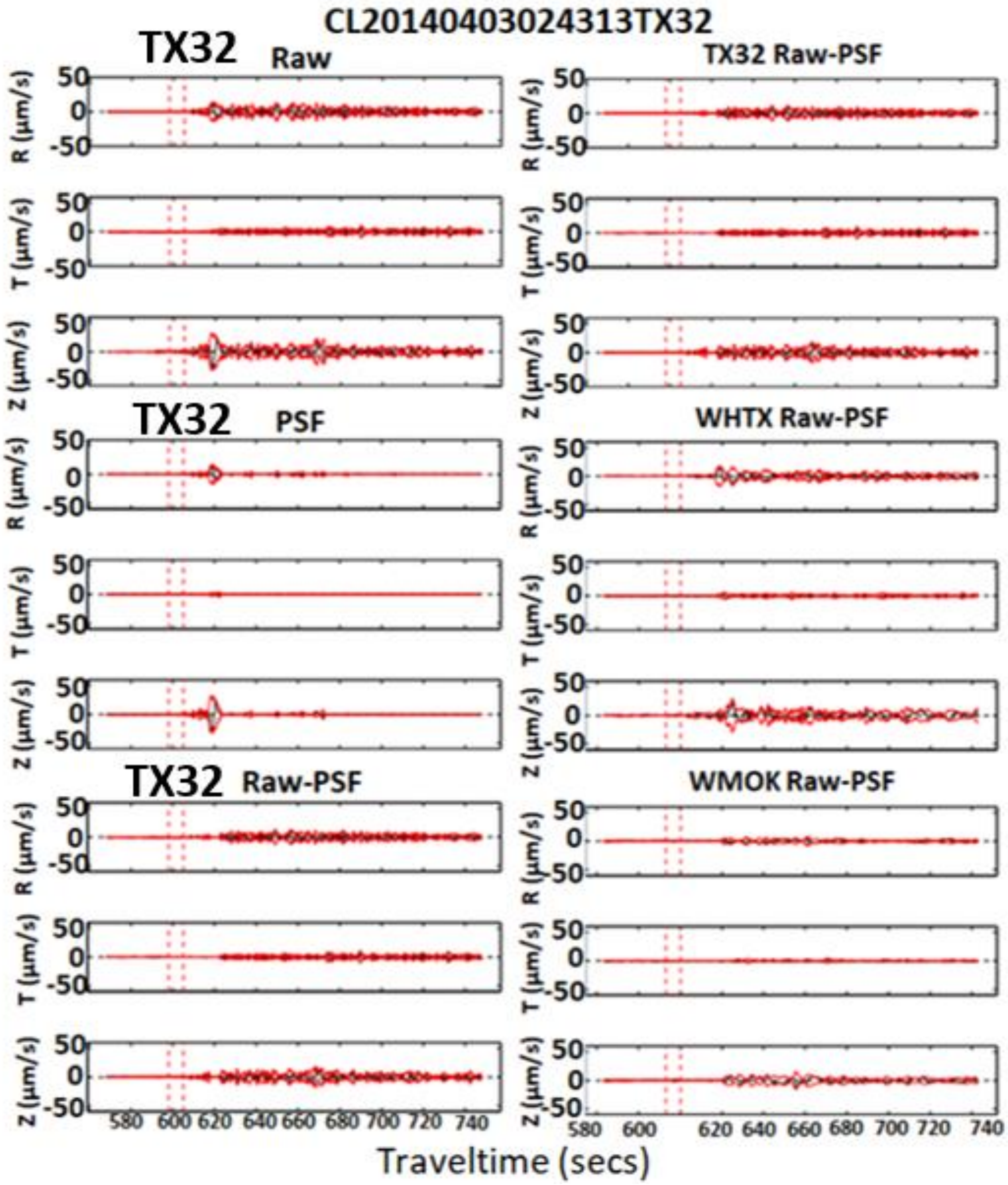

Figure 54. Seismograms of scattering noise. Subtracting the PSF from the raw seismogram isolates the coda.

Table 9 shows the eight events along with their total and transverse energy, which is a measure of coda. ‘Mw’ is the moment magnitude from the catalogue. ‘mb’ is the body-wave magnitude computed from the data. These are usually comparable.

Table 9. Scattering noise energy.

Event	Station	Mw	Δ (deg)	Depth (km)	mb	Total Energy $(\mu m/s)^2$	Transverse Energy $(\mu m/s)^2$
XX20141009021431	**TX32**	7.00	61.48	16.50	7.47	21.86	2.00
	WHTX	7.00	64.99		7.35	21.96	0.94
	WMOK	7.00	67.45		7.03	2.35	0.08
PE20130925164243	**TX32**	7.10	53.00	40.00	7.79	60.53	8.81
	WHTX	7.10	52.40		7.67	39.17	3.33
	WMOK	7.10	55.34		7.49	14.66	1.27
RU20130419030553	**TX32**	7.20	79.15	110.00	8.91	202.66	31.42
	WHTX	7.20	80.75		7.87	16.65	2.36
	WMOK	7.20	77.96		7.52	7.02	0.69
PE20151124224539	**TX32**	7.60	50.67	606.20	7.92	1008.98	181.62
	WHTX	7.60	49.31		7.71	183.78	23.63
	WMOK	7.60	52.19		7.41	50.78	7.03
CL20140403024313	**TX32**	7.70	59.03	22.40	7.74	60.98	8.83
	WHTX	7.70	58.30		7.89	76.42	3.65
	WMOK	7.70	61.22		7.77	26.72	1.23
RU20170717233414 (bad signal)	**TX32**	7.70	65.29	10.00	9.10	239.19	36.96
	WHTX	7.70	66.67		7.42	42.13	2.08
	WMOK	7.70	63.86		7.58	15.08	0.61
EC20160416235837	**TX32**	7.80	36.63	20.60	7.94	342.83	51.70
	WHTX	7.80	35.54		7.31	133.63	5.81
	WMOK	7.80	38.46		7.54	70.59	4.02
CL20150916225433	**TX32**	8.30	67.78	22.40	8.23	532.09	108.58
	WHTX	8.30	67.77		8.03	271.13	13.07
	WMOK	8.30	70.72		7.93	71.95	2.85

Later arrivals have two components of noise, the ambient background and scattering noise, whereas the P-phase is ahead of the scattering and just encounters the background noise. Background noise includes cities, humans, transportation, wind, etc. TX32 in west Texas does not experience much background noise, while it is high at WHTX which is in the most developed part of the state. WMOK is more isolated than WHTX, but not as much as TX32. TX32 experiences the most scattering while WMOK experiences the least. Table 9 suggests WMOK is the best station, but further analysis might conclude that WHTX is the best.

6.5 Ranking of Stations

Table 10 gives information about the level of background noise, scattering noise, and local velocity heterogeneity each station experiences.

Table 10. Ranking of the stations in terms of scatter and detection percentage for the 'et' method.

	P-traveltime scatter	**S-traveltime scatter**	**No P-phase detection %**	**No S-phase detection %**	**No pP-phase detection %**	**Azimuth scatter**
LOW ↓ HIGH	TX32	TX32	TX32	WHTX	WMOK	WHTX
	WMOK	WMOK	WMOK	WMOK	WHTX	WMOK
	WHTX	WHTX	WHTX	TX32	TX32	TX32

TX32 has the lowest background noise, and hence, ranks lowest in terms of traveltime scatter. The lower background noise is supported by the higher SNRs found at TX32 (see Figure 53). TX32 detects more P-phases, but the less S- and pP-phases than the other stations. This station has high scattering noise which affects detection of the later arrivals. This station's remoteness results in higher SNRs, so more events are detected; however, later arrivals are not detected sufficiently.

WHTX has higher background noise, and hence, ranks highest in terms of traveltime scatter. WHTX detects less P-phases, but more S- and pP-phases than TX32. Low azimuth scatter indicates low 3D velocity inhomogeneity. There is less velocity inhomogeneity at WHTX and more at TX32. Table 10 suggests that WHTX is the best station.

6.6 SNR

Because the SNR is determined from the seismograms, not comparison to the nominal location, it was speculated that rejecting low SNR events would improve the statistics and/or pattern recognition. A SNR cutoff of 10 dB was implemented and compared to the events with no cutoff. This cutoff rejected 10 events; however, some were well located. Tables 11 and 12 show the statistics for the events with a 10 dB cutoff. There are very small improvements in the standard deviations; therefore, the 10 dB cutoff was not implemented.

Table 11. Statistics for Common events with 10 dB cutoff with magnitudes ≥6.

Station	Total # of events	Deep	Shallow	Incom-plete	No P	No S	No pP	Bad	P-wave bad arrival	S-wave bad arrival	Fair or bad polari-zations
Count.											
TX32	103	18	81	0	0	12	84	1	1	11	8
WHTX	103	15	59	0	19	19	73	1	2	11	1
WMOK	103	16	70	0	12	16	73	1	0	8	4
Total #	**309**	**49**	**210**	**0**	**31**	**47**	**230**	**3**	**3**	**30**	**13**
Percentage.											
TX32	100	17	79	0	0	12	82	1	1	11	8
WHTX	100	15	57	0	18	18	71	1	2	11	1
WMOK	100	16	68	0	16	16	71	1	0	8	4
Total #	**100**	**16**	**68**	**0**	**15**	**15**	**74**	**1**	**1**	**10**	**4**

Table 12. Statistics for Common events with 10 dB cutoff with magnitudes ≥6 for the 'et' method.

Station	#	Nloc	md	rsd	md	rsd	md	rsd	md	rsd
			δTP		*δTS*		*δΔ*		*δA*	
TX32	103	91	-2.2	4.1	-3.7	6.6	0.1	1.0	-0.4	13.6
WHTX	103	84	-0.2	5.4	0.96	9.0	0.54	1.5	-1.4	4.7
WMOK	103	87	-0.5	3.9	0.78	7.9	0.57	1.2	-2.1	8.3
Total	**309**	**262**	**-1.0**	**4.5**	**-0.7**	**7.9**	**0.4**	**1.3**	**-1.3**	**9.71**

Averages

6.7 Azimuth, Distance, and Traveltime

TX32 has lower traveltime and distance scatter, while WHTX has lower azimuth scatter. TX32 has fewer no P-phase detections, while WHTX has fewer no S-phase detections.

Azimuth error should increase with distance as the raypath becomes more vertical at the station. Generally, lower SNRs are found at greater distances. The azimuth is plotted against the distance error in Figure 55. For TX32 and WMOK, the error increases with bias beyond approximately 50°. For WHTX, the error does not increase until approximately 80°. There is some bias in TX32 for distances <50°. Bias in the azimuth increases for TX32 and WMOK but not for WHTX; this is because these stations have deeper velocity heterogeneity.

The S-traveltime error dominates the distance error, not the P-traveltime error. The azimuth error dominates the location error, not the distance error. Arrival times for the S- and pP-phase are better determined than the P-phase azimuth. Figure 55 shows a tapering of azimuth error from right to left. There are more outliers at greater distances.

TX32 is shifted from zero-mean and has a sinusoidal pattern with more bias at greater distances. For WHTX, the scatter does increase but there is not as much bias.

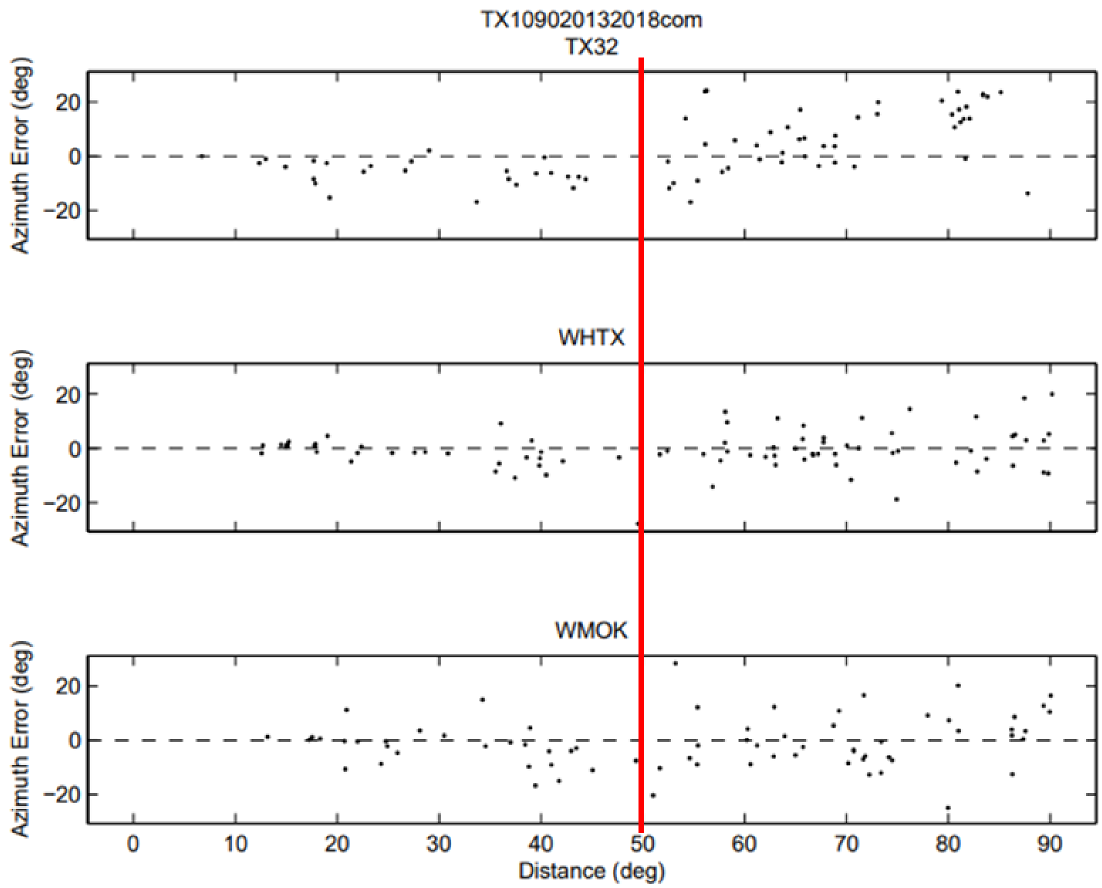

Figure 55. The azimuth errors against the estimated distances plotted for TX32, WHTX, and WMOK. The P-phase was selected to compute the azimuth. The red line marks 50°.

Traveltime errors are plotted for each phase at each station in Figure 56. The traveltime error and bias is large for the S-phase and, especially, the pP-phase. The P-phase is well defined and has a tighter distribution compared to other phases. TX32 has a systemic shift for the S-phase. There is clearly bias for the pP-phase among all three stations. WHTX and WMOK have a general increase in scatter. WHTX and WMOK show a similar pattern, however, TX32 is different. TX32 does not detect many pP-phases, so this station is not well-represented.

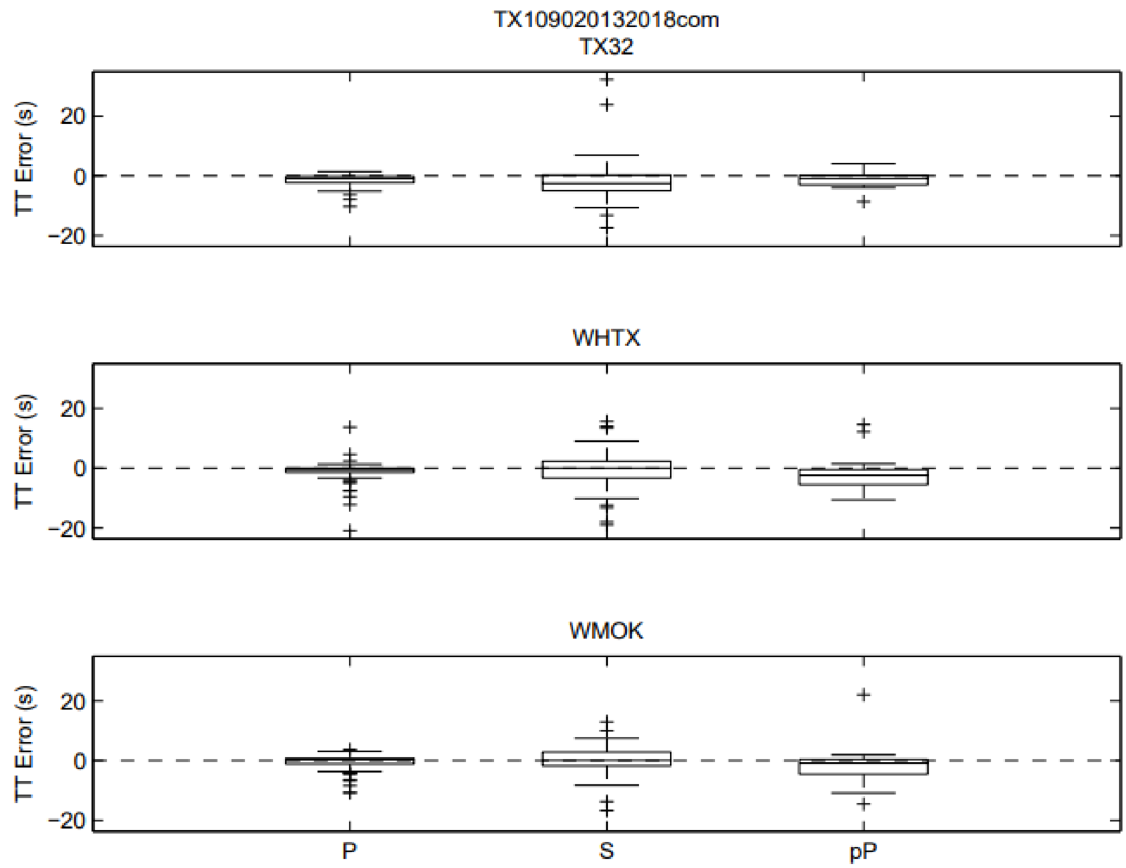

Figure 56. The traveltime error for the P-, S-, and pP-phase for TX32, WHTX, and WMOK. The number of undetected P-phases: TX32- 1, WHTX- 9, WMOK- 8. The number of undetected S-phases: TX32- 14, WHTX- 9, WMOK- 12. The number of undetected pP-phases: TX32- 89, WHTX- 77, WMOK- 75.

S-P and pP-P errors are plotted for each station in Figure 57. Again, there is clearly bias for the pP-phase among the three stations.

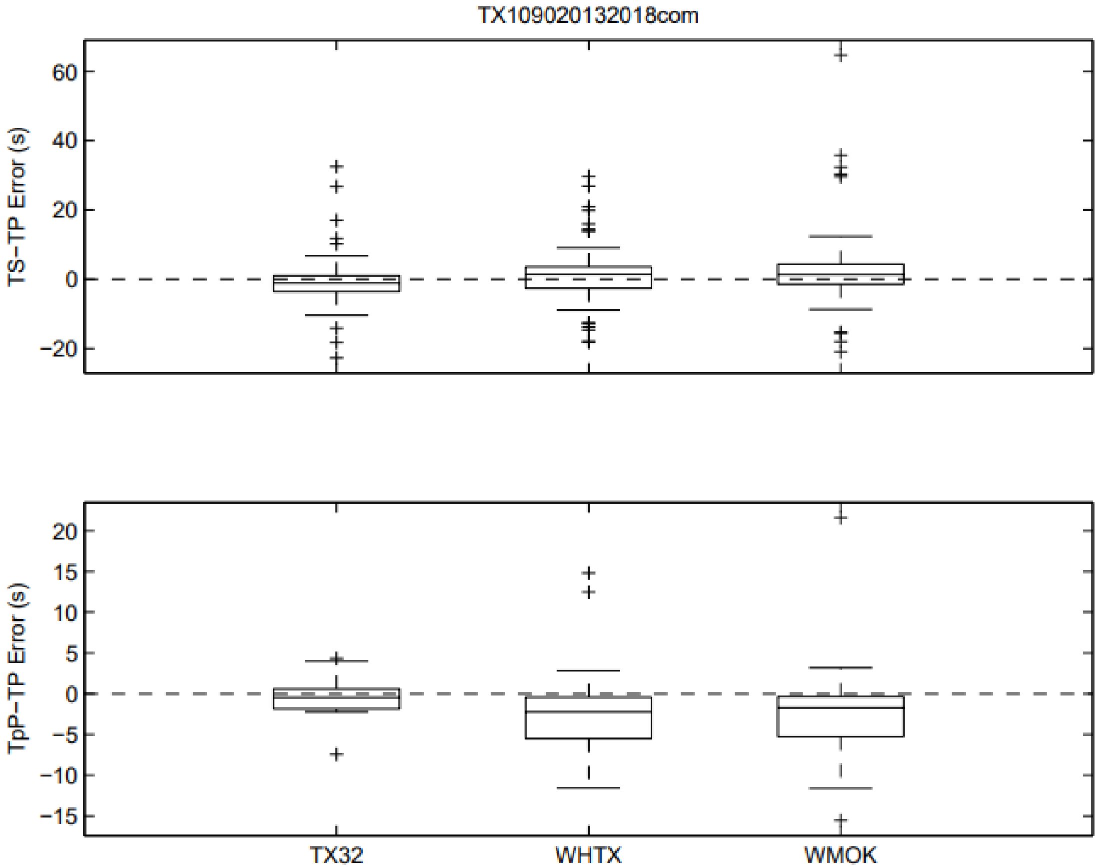

Figure 57. The S-P and pP-P time error for TX32, WHTX, and WMOK. The number of undetected S-phases: TX32- 14, WHTX- 9, WMOK- 12. The number of undetected pP-phases: TX32- 89, WHTX- 77, WMOK- 75. This boxplot includes outliers.

6.8 pP and Depth Estimation (pP-P Time)

Approximately 75% of events fail to detect the pP-phase. This could be due to scattering noise or a bad detection algorithm. When looking at traveltime errors for the P-, S- and pP-phases, the pP-phase is late (<0 seconds) at all the stations. The S-phase is early at WHTX and WMOK, but late at TX32, indicating upper mantle S-velocity differences. This pattern can also be seen in the S-P and pP-P times. The pP-traveltime errors are likely due to velocity differences in the lithosphere at the source, depending on oceanic versus continental lithosphere structure.

It was speculated that implementing a different velocity model would improve arrival determination. The IASP91 model was plotted along with three other velocity models: PREM, the AK135 continental model, and the AK135 oceanic model. It is evident that there are some differences between models as seen in Figure 58.

PREM is a globally averaged model that includes both continents and oceans (Dziewonski and Anderson, 1981). PREM has much larger time differences from the IASP91 model than the AK135 models. IASP91 is a continental model, and is not very different from the AK135 continental model; however, is very different from the AK135 oceanic model (Kennett et al., 1995; Montagner and Kennett, 1995).

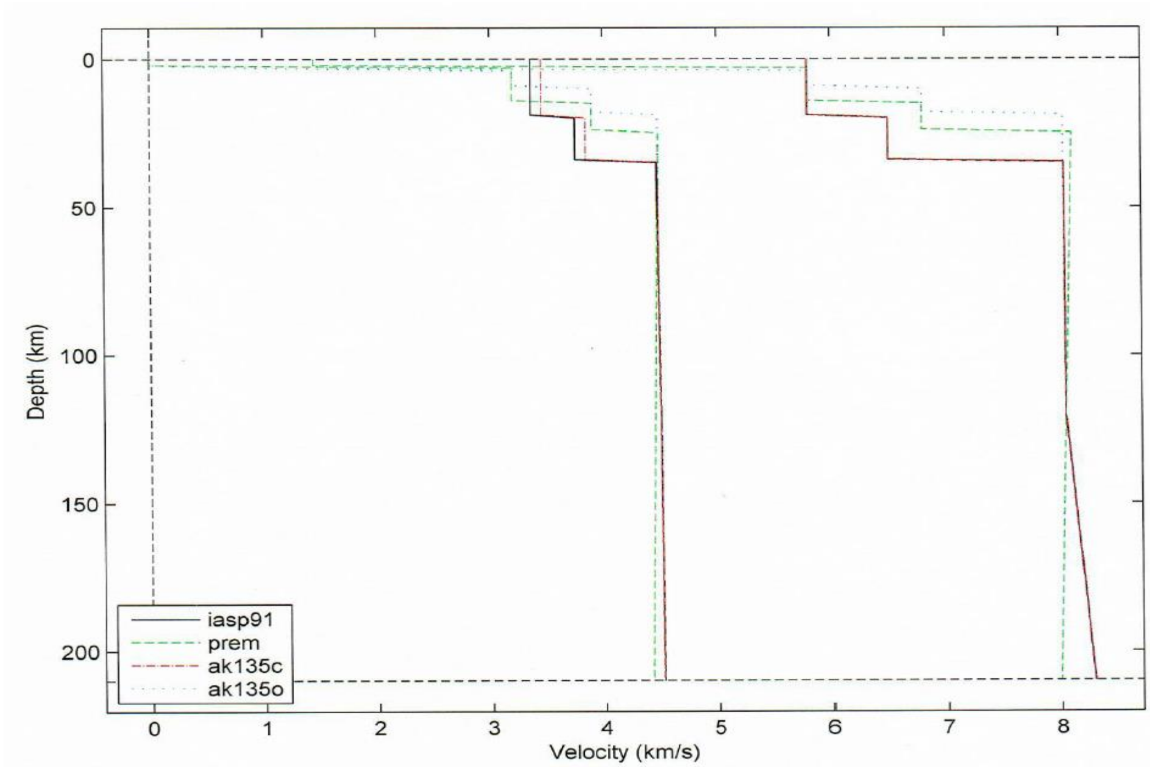

Figure 58. Velocity models for the P- and S-phase for depths <210 km. The IASP91, PREM, AK135C (continental), and AK135O (oceanic) models are portrayed. This plot only shows the upper mantle.

Table 13 represents the traveltime for a ray traveling vertically through 210 km.

Table 13. Table of P- and S-phase traveltimes <210 km for oceanic versus continental velocity models.

Velocity model	P traveltime	S traveltime
iasp91	27.3316 s	48.8646 s
prem	28.5673 s	47.8053 s
ak135c	28.3311 s	48.5670 s
ak135o	28.2757 s	47.1296 s
	Differences in P traveltime	**Differences in S traveltime**
iasp91-prem	-1.2357 s	1.0594 s
iasp91-ak135c	0.0005 s	0.2977 s
iasp91-ak135o	-0.9446 s	1.437 s

The P-traveltime difference is approximately -1 second, while the S-traveltime difference is approximately +1 second. Together, this means a 2 second error in S-P times, which will affect the distances, and hence, the locations. This could explain the error in the S-traveltimes and S-P times. Perhaps using a different velocity model could have minimized these traveltime differences. This is discussed more in *Chapter 7: Discussion of Results.*

After analysis of the statistics, it was concluded that locations that included depth, the 'ett' locations, were not very successful. There was not a significant difference in the location estimates between the 'et' and 'ett' methods. It was expected that the 'ett' method would obtain higher location accuracy; however, this was not the case. If an accurate depth was obtained, then these locations would have higher accuracy. Because picking of the pP-phase onset times were very problematic, the depth estimates were not accurate.

CHAPTER 7

DISCUSSION OF RESULTS

These results are applicable to Mars. The scenario was one station on a planet with limited knowledge. The 1950 knowledge of Earth would be a hopeful expectation for 2020 knowledge of Mars. In 1950, the Jeffreys-Bullen Earth model (circa 1940) and the Gutenberg and Richter seismicity map had been constructed. Plate tectonics was 10 years in the future. Currently, there is not much knowledge about the mantle structure and tectonics of Mars. In addition, there have only been predictions for Martian velocity models. This analysis shows that if the single seismic station is located in a region that is not geologically complex, and a region without heterogeneities that cause scattering, single-station event location may work well.

This research investigated the performance of single-station event location. The main objective was to analyze how effectively a single station could perform for event location relative to a global network of stations. This goal was satisfactorily accomplished meaning some single-station results compare favorably to Gutenberg and Richter. A single-station processor was developed that could locate the majority of events; although, in some geographic regions, this processor performed better, and in some areas worse. Near the TXOK region stations, events (>50°) were located successfully with relatively small error (i.e. the Meso-American subduction zone). At distances >50°, events were located with more error. The Aleutian/Kamchatka subduction zone had the greatest location error. At distances <90°, seismic waves are confined to the mantle and the location process is simplified.

The objective was to obtain homogeneous coverage of seismic events in both azimuth and distance for a hemisphere. This goal was more difficult to accomplish because most earthquakes occur in narrow arcuate zones on Earth. This research used a hemisphere centered on Texas and most events were located to the southeast and northwest, but not many in the northeast. This resulted in coverage that was not uniform in azimuth. In the southwestern direction, distance coverage was non-uniform although azimuthal coverage was more acceptable.

Arrival determination is a very important part of the location process. A major source of error for this program stems from inaccurate arrivals picks. The S-phase is often picked early, while the pP-phase is picked late relative to nominal. Arrivals were more or less accurate; however, the velocity model was the limitation. No 1D model can ever be correct on the Earth. Regional differences in the upper mantle and crust result from billions of years of tectonic activity. Some of these differences are accounted for in the global network locations, but these are based on decades of experience and thousands of events.

The type of velocity model selected affects the arrival picking process. The IASP91 Earth model is not the most recent velocity model; AK135 is an improved model. Perhaps implementing this model instead would have yielded better arrival picks, especially for the S-wave. If a different velocity model had been implemented, would the S-wave arrival error have been reduced?

Picking the pP- onset time was problematic. Bias for the pP-phase could be the result of a bad arrival pick or the selected velocity model. Perhaps implementing a velocity model that selects either continental or oceanic models as appropriate for each event would be a better choice for the pP-phase. The PREM 1D model utilizes different models for different lithosphere environments depending if you are in a continental or oceanic region. The pP-phase raypath goes upward from the surface, is reflected, and then downward through the mantle. This means that in most cases the pP-phase raypath could travel through continental lithosphere at the receiver end and oceanic lithosphere at the epicenter end. This error effects both the nominal arrival times computed from the nominal location and locations computed from measured arrival times.

Also, if the wrong velocity model is implemented in the processor, then the nominal arrival times could be incorrect. The nominal arrival times are based on the type of velocity model selected. The S- or pP- onset time pick could actually be a good pick, but because it's being compared to a bad nominal time, it may appear to be off.

The results convey the importance of having accurate seismic velocity models for the P-, S-, and pP-phases. Selecting the appropriate velocity model should be done carefully. Some velocity models are better suited for the certain environments than others. The choice of velocity model implemented into the program has many effects on the outcome.

Other algorithms for automatic arrival time detection could be investigated. Methods for arrival determination include Ross and Ben-Zion (2014), Ross and Ben-Zion (2014), and Ross et al. (2016). They present alternate and perhaps better ways to detect S-arrivals.

Bad later arrival picks could also be due to the coda present in the seismogram. Scattering obscures the signal, making it difficult to detect later arrivals. The first arrival precedes the coda, but later arrivals are hindered by the coda. While initial P-arrivals were statistically consistent, S- and later P-arrivals were not.

Another source of error stems from the time errors. These include the S-P and pP-P times. Distance errors are introduced by bad S-arrival times. Depth errors are introduced by bad pP-arrival times.

This analysis shows there is a combination of factors that impact single-station event location. Different geologic regions have different seismic velocity structures and densities that cause varying degrees of azimuthally dependent azimuth errors and scattering. TX32 has the worst azimuth estimates. The complex geology and sedimentary structures cause this station to encounter the large azimuthal bias and highest scattering. WHTX has the best azimuth estimates. Sedimentary structures cause this station to encounter scattering; however, the scattering is only moderate because the geology is not as complex as TX32. WMOK has intermediate azimuth estimates; however, has the least scattering. The Wichita Mountains are a complex structure like the Basin and Range Province, but the granite under WMOK produces less scattering, yielding better locations than TX32. The Wichita Mountains are more complex than the Great Plains Province, which explains why WHTX yields better azimuth estimates and locations than WMOK. From a global perspective, these stations are not very far apart. However, there are significant changes in the geologic structure present at each site.

Changes in lithospheric thickness and velocity variations in the upper mantle have significant effects on the quality of the computed azimuth estimates. The way in which lithospheric thickness is distributed over a continent can cause azimuthal dependence in some geographic regions (Liu and Gao, 2018). The magnitude of 3D velocity structures is relative to an assumed 1D velocity model.

CHAPTER 8

FUTURE WORK

Now that this processor has proven to be stable and acceptably accurate, in the future the processor could be used on Martian data which is being archived at IRIS. There are some modifications that could be made to the program to achieve better results. These are discussed below.

Because detecting accurate arrival times is of high importance, modifications related to this part of the processor would be of high priority. More accurate arrival times would certainly yield more accurate single-station event locations. Other algorithms for automatic arrival time detection could be investigated. A different velocity model could be implemented. Further work to obtain better picks for the problematic S- and pP-phases would be imperative.

Association of arrivals with ray types (P, S, pP, etc.) could be improved. After the P-signal is detected, there needs to be some process to establish what ray type it is. Kennett’s later work discussed phase association (Bai and Kennett, 2000; Bai and Kennett, 2001). Phase identification was executed through the analysis of the energy and frequency content of the seismograms along with polarization analysis and waveform correlation characteristics (Bai and Kennett, 2000). They also proposed that instantaneous frequency methods could be implemented in conjunction with other detection methods in order to achieve more accurate detections (Bai and Kennett, 2001; Kennett 2002). The methods of Bai and Kennett (2000) and Bai and Kennett (2001) could be investigated more.

The magnitude threshold could be lowered to include events in the sparse geographic regions. Lowering the magnitude threshold to 5 could yield some events in the northeastern region. However, lowering this threshold would make the database become significantly larger. Processing of all these events would take an extensive amount of time. This large database would then contain many more events with varying levels of SNRs. This is problematic because lower magnitude events will generally have lower SNRs which are typically associated with worse location estimates. If the magnitude is lowered, it needs to be ensured that only events with higher SNRs are selected, while events with the lower SNRs are discarded.

To get better results, a more restrictive analysis could be done with a distance range of 10°-50°. As seen in the mislocation maps from the analysis, events are much better located within the 50° window. The IASP91 model is not adequate for distances ≤10°; therefore, a different velocity model would need to be implemented.

REFERENCES

Akaike, H., 1974, A new look at the statistical model identification: IEEE Transactions on Automatic Control, **AC-19**, no. 6, 716-723.

Allen, R.V., 1978, Automatic earthquake recognition and timing from single traces: Bulletin of the Seismological Society of America, **68**, no. 5, 1521-1532.

Ammon, C.J., T. Lay, and D.W. Simpson, 2010, Great earthquakes and global seismic networks: Seismological Research Letters, **81**, no. 6, 965-971.

Aster, R., 2011, Fundamentals of ray tracing, http://www.ees.nmt.edu/outside/courses/GEOP523/Docs/rays.pdf, accessed 12 February 2019.

Astiz, L., P. Earle, and P. Shearer, 1996, IASP91 traveltimes: Surface focus, https://earthquake.usgs.gov/learn/topics/ttgraph.php, accessed 24 January 2019.

Bai, C., and B.L.N. Kennett, 2000, Automatic phase-detection and identification by full use of a single three-component broadband seismogram: Bulletin of the Seismological Society of America, **90**, no. 1, 187-198.

Bai, C., and B.L.N. Kennett, 2001, Phase identification and attribute analysis of broadband seismograms at far-regional distances: Journal of Seismology, **5**, issue 2, 217-231.

Bashir, L., S.S. Gao, and K.H. Liu, 2011, Crustal structure and evolution beneath the Colorado Plateau and the southern Basin and Range Province: Results from receiver function and gravity studies: Geochemistry, Geophysics, Geosystems, **12**, no. 6, 1-18.

Bent, A., 2013, Global Seismograph Network (GSN), *in* P.T. Bobrowsky, ed., Encyclopedia of Natural Hazards, 417-418.

Bowles, N. E., W. T. Pike, N. Teanby, G. Roberts, S. B. Calcutt, J. Hurley, P. Coe, J. Wookey, P. Dunton, I. Standley, J. Temple, R. Irshad, J. Taylor, T. Warren, and C. Charalambous, 2015, Performance and noise modelling of the short period seismometer SEIS-SP, part of the SEIS instrument for NASA's 2016 InSight mission: 46th Lunar and Planetary Science Conference, Abstract 2146.

Bracewell, R., 1965, The Fourier transform and its applications: McGraw-Hill Book Co.

Braile, Larry, 2007, Interpreting seismograms- A tutorial for the AS-1 seismograph, http://web.ics.purdue.edu/~braile/edumod/as1lessons/InterpSeis/InterpSeis.htm, accessed 22 January 2019.

Brown, T.E., 1971, Stratigraphy of the Washita group in central Texas: Baylor Geological Studies Bulletin, no. 21, 1-46.

Buland, R., and C.H. Chapman, 1983, The computation of seismic travel times: Bulletin of the Seismological Society of America, **73**, no. 5, 1271-1302.

Bullen K.E., and B.A Bolt, 1985, An Introduction to the Theory of Seismology: Cambridge University Press.

Burdick, S., F.L. Vernon, and R.D. van der Hilst, 2014, Model update May 2016: Upper-mantle heterogeneity beneath North America from travel-time tomography with global and USArray data: Seismological Research Letters, **85**, no. 1, 77-81, doi:10.1785/0220130098.

Bureau of Land Management, 2009, Final Programmatic Environmental Impact Statement for Geothermal Leasing in the Western United States: BML.

Butler, R., T. Lay, K. Creager, P. Earl, K. Fischer, J. Gaherty, G. Laske, B. Leith, J. Park, M. Ritzwolle, J. Tromp, and L. Wen, 2004, The global seismo-graphic network surpasses its design goal: EOS Trans. AGU, **85**, 225-229.

Byars, B., 2009, Development of a Lake Whitney learning laboratory manual: Lake Whitney Comprehensive Water Quality Assessment, 268-278.

Cather, S.M., R.M. Chamberlin, C.E. Chapin, and W.C. McIntosh, 1994, Stratigraphic consequences of episodic extension in the Lemitar Mountains, central Rio Grande Rift, *in* G.R. Keller and S.M. Cather, eds., Basins of the Rio Grande Rift: Structure, stratigraphy, and tectonic Setting: Geological Society of America Special Paper, **291**, 157-169.

Claerbout, J.F., 1976, Fundamentals of Geophysical Data Processing: McGraw-Hill Book Co.

Clinton, J.F., D. Giardini, P. Lognonné, B. Banerdt, M. Driel, M. Drilleau, N. Murdoch, M. Panning, R. Garcia, D. Mimoun, M. Golobek, J. Tromp, R. Weber, M. Böse, S. Ceylan, I. Daubar, B. Kenda, A. Khan, L. Perrin, and A. Spiga, 2017, Preparing for InSight: An invitation to participate in a blind test for Martian seismicity: Seismological Research Letters, **88**, no. 5, 1290-1302.

Dandonneau, P.A., P. Lognonné, W.B. Banerdt, S. Deraucourt, T. Gabsi, J. Gagnepain-Beyneix, T. Nébut, O. Robert, S. Tillier, K. Hurst, D. Mimoun, U. Christenssen, M. Bierwirth, R. Roll, T. Pike, S. Calcutt, D. Giardini, D. Mance, P. Zweifel, P. Laudet, L. Kerjean, and the SEIS team, 2013, The SEIS InSight VBB experiment: 44th Lunar and Planetary Science Conference, no. 1719.

Dziewonski, A.M., and D.L. Anderson, 1981, Preliminary reference Earth model: Physics of the Earth and Planetary Interiors, **25**, 297-356.

Earle, P.S., and P.M. Shearer, 1994, Characterization of global seismograms using an automatic-picking algorithm: Bulletin of the Seismological Society of America, **84**, no. 2, 366-376.

Fallin, J.A., 1990, Hydrogeology of the Terlingua Area, Texas: Texas Water Development Board Report, **323**, 1-50.

Frohlich, C., and J. Pulliam, 1999, Single-station location of seismic events: a review and a plea for more research: Physics of the Earth and Planetary Interiors, **113**, 277-291.

Gao, S.S., and K.H. Liu, 2014, Imaging mantle discontinuities using multiply-reflected P-to-S conversions: Earth and Planetary Science Letters, **402**, 99-106, doi:10.1016/j.epsl.2013.08.025.

Gao, S.S., and K.H. Liu, 2014, Mantle transition zone discontinuities beneath the contiguous United States: J. Geophysical Res. Solid Earth, **119**, 6452-6468.

Gao, S.S., K.H. Liu, R.J. Stern, G.R. Keller, J.P. Hogan, J. Pulliam, E.Y. Anthony, 2008, Characteristics of mantle fabrics beneath the south-central United States: Constraints from shear-wave splitting measurements: Geosphere, **4**, no. 2, 411-417.

Geiger, L., 1912, Probability method for the determination of earthquake epicenters from the arrival time only: Bull. St. Louis Univ., **8**, 60-71.

Gutenberg, B., and C.F. Richter, 1954, Seismicity of the Earth and associated phenomena, 2nd edition: Princeton University Press.

Herrmann, R., 2007, Introduction to earthquake seismology, http://www.eas.slu.edu/eqc/eqc_course/IntroSeis/Ass07/Ass07.pdf, accessed 5 February 2019.

Hill, R.T., 1901, Geography and geology of the Black and Grand Prairies, Texas: United States Geological Survey Annual Report, **21**, part 7.

Hull, A.M., 1951, Geology of the Whitney Reservoir area, Brazos River, Bosque-Hill Counties, Texas, *in* F.E. Lozo and B.F. Perkins, eds., The Woodbine and adjacent strata of the Waco area of central Texas: Fondren Science Series, no. 4, 45-63.

IRIS, 2011, IASP91 velocity model (inactive), http://ds.iris.edu/spud/earthmodel/9785632, accessed on 8 March 2019.

Jepsen, D. C., and B. L. N. Kennett, 1990, Three-component analysis or regional seismograms: Bulletin of the Seismological Society of America, **80**, no. 6, 2032-2052.

Johnson, K.S., 1974, Islands in the sea: Geology of the Wichitas: Great Plains Journal, **14**, no. 1, 33-55.

Johnson, K.S., 2008, Geologic history of Oklahoma, http://www.ogs.ou.edu/pubsscanned/EP9_2-8geol.pdf, accessed 31 January 2019.

Jurkevics, A., 1988, Polarization analysis of three-component array data: Bulletin of the Seismological Society of America, **78**, no. 5, 1725-1743.

Kawabayashi, T., H. Mikada, T. Goto, J. Takekawa, and K. Onishi, 2012, Availability of the τ-p transform detection using seismic reflection incident angles and impacts on Fresnel volume migration, BUTSURI-TANSA, **65**, no. 4, 213-222.

Keller, R.G., 1988, Geophysical maps of the Ouachita region: The Geological Society of America.

Kennett, B. L. N., 1991, The removal of free surface interactions from three-component seismograms: Geophys. J. Int., **104**, 153-163.

Kennett, B.L.N., 2001, The seismic wavefield volume I: Introduction and theoretical development: Cambridge University Press.

Kennett, B.L.N., 2002, The seismic wavefield volume II: Interpretation of seismograms on regional and global scales: Cambridge University Press.

Kennett, B.L.N., and E.R. Engdahl, 1991, Traveltimes for global earthquake location and phase association: Geophys. J. Int., **105**, 429-465, doi:10.1111/j.1365-246X.1991.tb06724.x.

Kennett, B.L.N., E.R. Engdahl, and R. Buland, 1995, Constraints on seismic velocities in the Earth from traveltimes: Geophys. J. Int., **122**, 108-124.

Khan A., M. van Driel, M. Bose, D. Giardini, S. Ceylan, J. Yan, J. Clinton, F. Euchner, P. Lognonné, N. Murdoch, D. Mimoun, M. Panning, M. Knapmeyer, and W.B. Banerdt,2016, Single-station and single-event marsquake location and inversion for structure using synthetic Martian wavefokawarms: Physics of the Earth and Planetary Interiors, **258**, 28-42.

Kim, S.G., and F. Gao, 1997, Study on some characteristics of earthquakes and explosions using the polarization method: J. Phys. Earth, **45**, 13-27.

Kim, S.G., and Z. Wu, 1997, Uncertainties of seismic source determination using a 3-component single station: J. Phys. Earth, **45**, 1-11.

Kocher, A.E., 1916, Reconnaissance soil survey of south-central Texas: Field Operations of the Bureau of Soils, **15**, 1073-1183.

Kushner, B., G.S. Soreghan, and M.J. Soreghan, 2017, Heterogeneity of clastic provenance to the Pennsylvanian Anadarko Basin and implications for paleogeomorphology: Geological Society of America Abstracts with Programs, **49**, no. 6.

Lawyer, L.C., C.C. Bates, and R.B. Rice, 2001, Geophysics in the affairs of Mankind: A Personalized History of Exploration Geophysics: Society of Exploration Geophysicists.

Leonard, M., 2000, Comparison of manual and automatic onset time picking: Bulletin of the Seismological Society of America, **90**, no. 6, 1384-1390.

Leonard, M., and B.L.N. Kennett, 1999, Multi-component autoregressive techniques for the analysis of seismograms: Physics of the Earth and Planetary Interiors, **113**, 247-263.

Li, T.M.C., J.F. Ferguson, E. Herrin, and H.B. Durham, 1984, High-frequency seismic noise at Lajitas, Texas: Bulletin of the Seismological Society of America, **74**, no. 5, 2015-2033.

Liu, L., and S.S. Gao, 2018, Lithospheric layering beneath the contiguous United States constrained by S-to-P receiver functions: Earth and Planetary Science Letters, **495**, 79-86.

Lognonné, P., W. B. Banerdt, D. Giardini, W. T. Pike, U. Christensen, B. Knapmeyer-Endrun, S. Raucourt, J. Umland, K. Hurst, P. Zweifel, S. Calcutt, M. Bierwirth, D. Mimoun, G. Pont, N. Verdier, P. Laudet, S. Smrekar, and T. Hoffman, 2017, SEIS/INSIGHT: One year prior to launch for seismic discovery on Mars: EGU General Assembly Conference Abstracts, **19.**

Loughran, L.B., 1990, Semiannual Technical Summary: NORSAR Scientific Report, no. 2, 1-105.

Lukasik, S.J., 2011, Why the ARPANET was built: IEEE Annals of the History of Computing, 40-20.

Madston, E.A, 1990, Seismic polarization analysis: MS Thesis, University of Texas at Dallas.

Magotra, N., D. Nalley, R. Weaver, 1991, Real time seismic event detection and discrimination using multi-channel data: Proceedings of the IEEE, **2**, 1204-1207.

Magotra, N., N. Ahmed, and E. Chael, 1986, A comparison of two parameter estimation schemes: Proceedings of the IEEE, **74**, no. 5, 760-761.

Magotra, N., N. Ahmed, and E. Chael, 1987, Seismic event detection and source location using single-station (three-component) data: Bulletin of the Seismological Society of America, **77**, no. 3, 958-971.

Marple, S.L., 1987, Digital spectral analysis with applications: Prentice-Hall Inc.

Mimoun, D., Naomi Murdoch, Philippe Lognonné, Kenneth Hurst, William T. Pike, Jane Hurley, Tanguy Nébut, William B. Banerdt, and SEIS Team, 2017, The noise model of the SEIS seismometer of the InSight mission to Mars: Space Sci Rev, **211**, 383-428.

Montagner, J.P., and B.L.N. Kennett, 1995, How to reconcile body-wave and normal-mode reference earth models: Geophys. J. Int., **125**, 229-248.

Murdoch, N., D. Mimoun, R.F. Garcia, W. Rapin, T. Kawamura, P. Lognonné, D. Banfield, and W.B. Banerdt, 2016, Evaluating the wind-induced mechanical noise on the InSight seismometers: Space Sci Rev, 1-27.

Nuemaier, A., and T. Schneider, 2001, Estimation of parameters and eigenmodes of multivariate autoregressive models: ACM Transactions and Mathematical Software, **27**, no. 1, 27-57.

Olson, J. V., 1982, Noise suppression using data-adaptive polarization filters: Applications to infrasonic array data: J. Acoust. Soc. Am., **72**, 1456-1460.

Panning, M. P., P. Lognonné, W. B. Banerdt, R. Garcia, M. Golombek, S. Kedar, B. Knapmeyer-Endrun, A. Mocquet, N. A. Teanby, J. Tromp, R. Weber, E. Beucler, J. F. Blanchette-Guertin, E. Bozdag, M. Drilleau, T. Gudkova, S. Hempel, A. Murdoch, A. C. Plesa, A. Rivoldini, N. Schmerr, Y. Ruan, O. Verhoeven, C. Gao, U. Christensen, J. Clinton, V. Dehant, D. Giardini, D. Mimoun, W. T. Pike, S. Smrekar, M. Wieczorek, M. Knapmeyer, J. Wookey, 2017, Planned products of the Mars structure service for the InSight mission to Mars: Space Sci Rev, 211, issue 1-4, 611-650.

Panning, M.P., É. Beucler, M. Drilleau, A. Mocquet, P. Lognonné, and W.B. Banerdt, 2015, Verifying single-station seismic approaches using Earth-based data: Preparation for data return from the InSight mission to Mars: Icarus, **248**, 230-242.

Panning, P., B.W. Banerdt, E. Beucler, L. Boschi , C. Johnson , P. Lognonné, A. Mocquet , R.C. Weber, 2012, InSight: Single station broadband seismology for probing Mars' interior: Lunar and Planetary Science Conference.

Park, J., K. Anderson, R. Aster, R. Butler, T. Lay, and D., Simpson, 2005, Global seismographic network records the Great Sumatra-Andaman earthquake: EOS Trans. AGU, **86**, 57-61.

Porritt, R.W., R.M Allen, and F.F. Pollitz, 2013, Seismic imaging east of the Rocky Mountains with USArray: Earth and Planetary Science Letters, **402**, 16-25, doi:10.1016/j.epsl.2013.10.034.

Prăvălie, R., 2014, Nuclear weapons tests and environmental consequences: A global perspective: Ambio: **43**, no. 6, 729-744.

Price, J.D., J.P. Hogan, M.C. Gilbert, and J.D. Payne, 1995, Surface and near-surface investigation of the alteration of the Mount Scott Granite and geometry of the Sandy Creek Gabbro pluton, Hale Spring area, Wichita Mountains, Oklahoma: Basement Tectonics, **12**, 79-122.

Priestly, M.B., 1981, Spectral analysis and time series: Academic Press Inc.

Prieto, G. A., R. L. Parker, D. J. Thomson, F. L. Vernon, and R.L. Graham, 2007, Reducing the bias of multitaper spectrum estimates: Geophys. J. Int., **171**, 1269-1281.

Raucourt, S.D., S. Tillier, N. Tanguy, J. Gagnepain-Beyneix, T. Gabsi, K. Hurst, P. Lognonné, M.D. Fossés, D. Mimoun, and W. Banerdt, 2012, The VBB SEIS experiment of InSight: 39th COSPAR Scientific Assembly, Abstract E1.15-29-12, 429.lognonn

Repasch, M., K. Karlstrom, M. Heizler, and M. Pecha, 2017, Birth and evolution of the Rio Grande fluvial system in the past 8 Ma: Progressive downward integration and the influence of tectonics, volcanism, and climate: Earth-Science Reviews, **168**, 113-164.

Research School of Earth Sciences, 2009, Model ak135-f, http://rses.anu.edu.au/seismology/ak135/ak135f.html, accessed 20 February 2019.

Rissanen, J., 1983, A universal prior for the integers and estimation by minimum description length: Ann. Stati., **11**, 417-431.

Robinson, E. A., and S. Treitel, 1980, Geophysical signal analysis: Prentice-Hall Inc.

Ross, Z.E., and Y. Ben-Zion, 2014, An earthquake detection algorithm with pseudo-probabilities of multiple indicators: Geophys. J. Int., **197**, 458-463.

Ross, Z.E., and Y. Ben-Zion, 2014, Automatic picking of direct P, S seismic phases and fault zone head waves: Geophys. J. Int., **199**, 368-381.

Ross, Z.E., M.C. White, F.L. Vernon, and Y. Ben-Zion, 2016, An improved algorithm for real-time s-wave picking with application to the (augmented) ANZA network in southern California: Bulletin of the Seismological Society of America, **106**, no. 5, 2013-2022.

Rost, S., and C. Thomas, 2002, Array seismology: Methods and applications: Reviews of Geophysics, **40**, no. 3, 1-27.

Ruedas, T., N. Schmerr, and N.G. Pérez, 2009, Seismological investigations of Mars' deep interior, https://mepag.jpl.nasa.gov/reports/decadal/seismars.pdf, accessed on 13 February 2019.

Ruesink, L.E., 1977, Taming the Brazos: Texas Water Resources Institute, **3**, no. 6, 1-6.

Samson, J. C., 1983, Pure states, polarized waves, and principal components in the spectra of multiple, geophysical time-series: Geophys. J. R. astr. Soc., **72**, 647-664.

Samson, J. C., 1983, The reduction of sample-bias in polarization estimators for multichannel geophysical data with anisotropic noise: Geophys. J. R. astr. Soc., **75**, 289-308.

Samson, J.C., 1980, Comments on polarization and coherence: J. Geophys., **48**, 195-198.

Samson, J.C., and J.V. Olson, 1980, Some comments on the descriptions of the polarization states of waves: Geophys. J. R. astr. Soc., **61**, 115-129.

Samson, J.C., and J.V. Olson, 1981, Data-adaptive polarization filters for multichannel geophysical data: Geophysics, **46**, no. 10, 1423-1431.

Sandidge-Bodoh, V., 1989, Investigating the effects fracture systems have on seismic wave velocities at the Lajitas, Texas seismic station: M.S. Thesis, Southern Methodist University.

Schaeffer, A.J., and S. Lebedev, 2014, Imaging the North American continent using waveform inversion of global and USArray data: Earth and Planetary Science Letters, **402**, 26-41.

Schweitzer, J., and M. Roth, 2015, The NORSAR Data Center (FDSN Network Code NO): Presented at the FDSN Meeting, IUGG.

Scrase, F.J., 1931, The reflected waves from deep focus earthquakes: Proceedings of the Royal Society of London Series A: Containing Papers of a Mathematical and Physical Character, **132**, no. 819, 213-235.

Shearer, P.M., 2009, Introduction to seismology, 2nd edition: Cambridge University Press.

Shieh, C.F., 1995, Study on the free surface coupling effect of seismic waves: TAO, **6**, no. 2, 197-207.

Sleeman, R., and T. van Eck, 2003, Single station real-time P and S phase pickers for seismic observatories, *in* T. Takanami, and G. Kitagawa, eds., Methods and applications of signal processing in seismic network operations: Lecture Notes in Earth Sciences, **98**, 173-194.

Smith, C.I., 1970, Lower Cretaceous stratigraphy, northern Coahuila, Mexico: The University of Texas at Austin, Bureau of Economic Geology, Report of Investigations, no. 65.

Soreghan, G.S., G.R. Keller, M.C. Gilbert, C.G. Chase, and D.E. Sweet, 2012, Load-induced subsidence of the Ancestral Rocky Mountains recorded by preservation of Permian landscapes: Geosphere, **8**, 654-668.

Spencer, J.M., 1966, Surface waters of Waco: Baylor Geological Studies Bulletin, no. 10, 1-56.

Takanami, T., and G. Kitawaga, 1988, A new efficient procedure for the estimation of onset times of seismic waves: J. Phys. Earth, **36**, 267-290.

Takanami, T., and G. Kitawaga, 1991, Estimation of the arrival times of seismic waves by multivariate time series model: Ann. Inst. Statist. Math., **43**, no. 3, 407-433.

Takanami, T., and G. Kitawaga, 1993, Multivariate time-series model to estimate the arrival times of S-waves: Computers & Geosciences, **19**, no. 2, 295-301.

Thomson, D.J., 1982, Spectrum estimation and harmonic analysis: Proceedings of the IEEE, **70**, no. 9, 1055-1096.

Tibuleac, I., and E. Herrin, 1997, Calibration studies at TXAR: Seismological Research Letters, **68**, no. 2, 353-365.

Tong, C., 1995, Characterization of seismic phases- an automatic analyzer for seismograms: Geophys. J. Int., **123**, 937-947.

Tong, C., and B. L. N. Kennett, 1995, Towards the identification of later seismic phases: Geophys. J. Int., **123**, 948-958.

Tong, C., and B.L.N. Kennett, 1996, Automatic seismic event recognition and later phase identification for broadband seismograms: Bulletin of the Seismological Society of America, **86**, no. 6, 1896-1909.

Trnkoczy, A., 2012, Understanding and parameter setting of STA/LTA trigger algorithm, in P. Bormann, ed., New manual of seismological observatory practice 2 (NMSOP-2): Duetsches GeoForschungsZentrum GFZ, 1-20.

U.S. Congress, 1988, Seismic verification of nuclear testing treaties: Office of technology assessment: U.S. Government Printing Office.

U.S. Geological Survey, 2018, How do seismologists locate an earthquake?, https://www.usgs.gov/faqs/how-do-seismologists-locate-earthquake, accessed 13 February 2019.

USArray, 2014, USArray: A continental-scale seismic observatory, www.usarray.org, accessed 16 April 2019.

Van Schmus, W.R., M.E. Bickford, and A. Turkek, 1996, Proterozoic geology of the east-central Midcontinent basement, *in* B.A. der Pluijm and P.A. Catacosinos, eds., Basements and basins of eastern North America: Geological Society of America Special Paper, **308**, 7-32.

Vidale, J.E., 1986, Complex polarization analysis of particle motion: Bulletin of the Seismological Society of America, **76**, no. 5, 1393-1405.

Wermund, E.G., 1996, Physiographic map of Texas, http://www.beg.utexas.edu/UTopia/ images/pagesizemaps/physiography.pdf, accessed 30 January 2019.

Wiggins, R.A., and E.A. Robinson, 1965, Recursive solution to the multichannel filtering problem: J. Geophys. Res., **70**, no. 8, 1885, 1891.

Withers, M., R. Aster, C. Young, J. Beiriger, M. Harris, S. Moore, and J. Trujillo, 1998, A comparison of select trigger algorithms for automated global seismic phase and event detection: Bulletin of the Seismological Society of America, **88**, no. 1, 95-106.

Yilmaz, Ö., 1987, Seismic data processing: Society of Exploration Geophysicists.

Zhu, H., D. Komatitsch, and J. Tromp, 2017, Radial anisotropy of the North American upper mantle based on adjoint tomography with USArray Geophys. J. Int., **211**, 349-377.

BIOGRAPHICAL SKETCH

Lauren Phillips was born in Singapore, Asia. After graduating from Plano East Senior High School, she went on to to get her first Bachelor of Science degree at Baylor University, graduating in 2013. In August 2014, she entered The University of Texas at Dallas. She received her second Bachelor of Science with a major in Geoscience, and a focus in Geophysics, in May 2017. She remained at The University of Texas at Dallas where she received a Master of Science in Geoscience (more specifically, Geophysics) in May 2020. She started working as a geophysical intern at PetroTel in 2015.

CURRICULUM VITAE

Lauren Phillips

Education

Master of Science (MS) in Geosciences
The University of Texas at Dallas
Fall 2017 - May 2020
GPA 3.963/4.0

Bachelor of Science (BS) in Geosciences,
The University of Texas at Dallas
Fall 2014 - May 2017
GPA: 3.731/4.0

Bachelor of Science (BS) in Nursing
Baylor University
Fall 2008 - Spring 2013
GPA 3.6/4.0

Professional Experience

Geophysical Intern, PetroTel, Plano TX
Sept 2015 – Present

Field Work Experience

Summer of Applied Geophysical Experience (SAGE)
Summer 2016

Skills

Petrel, ArcGIS, MATLAB, Hampson-Russell

Professional Memberships

Society of Exploration Geophysicists, Student Member
American Geophysical Union, Student Member
American Association of Petroleum Geologists, Student Member
Seismological Society of America, Student Member